UNIVERSITY OF CALIFORNIA

Santa Barbara

Redox reactions of Silica-Supported Catalysts and their Molecular Analogs

A dissertation submitted in partial satisfaction of the requirements for the degree Doctor of Philosophy in Chemistry

by

Bethany N. Wigington

Committee in charge:

Professor Susannah L. Scott, Chair

Professor Peter Ford

Professor Dan Little

Professor Ram Seshadri

March 2015

The dissertation of Bethany N. Wigington is approved.

_____

Dr. Peter Ford

_____

Dr. Dan Little

_____

Dr. Ram Seshadri

_____

Dr. Susannah L. Scott, Chair

January 2015

Redox reactions of Silica-supported Catalysts and their Molecular Analogs

by

Bethany N. Wigington

AKNOWLEDGMENTS

The work in this dissertation would not have been possible without the help and support of so many people. I first would like to thank my advisor, Professor Susannah Scott, for her support and guidance throughout my study and research. Without her, the work and writing in this thesis would not have been possible. I am grateful for the many experiences and opportunities I have been provided by working in her group. Although at times it was overwhelming, the diverse projects I worked on, people I've met, and places I've been have molded me as a researcher and person. I am also thankful for the past and present members of the Scott group, especially my friend and graduate student mentor, Dr. Anthony Crisci, who was patient with me and always willing to help especially after much persistence on my part.

My thesis research involved many collaborations and I greatly appreciate for the valuable contributions from Raúl Adler-Yañez (U. of Münster), Professor Gerhard Erker (U. of Münster), Dr. Gerald Kehr (U. of Münster), Dr. Tim Brewster (U. of Wash.), Dr. Jaime Flores (Rutgers), Dr. Jerry Hu (MRL), Dr. Tsu-Chien Weng (SSRL), Dr. Dimosthenis Sokaras (SSRL), and Professor Jin-ping Zhang (SINANO). Without their assistance a large portion of this work would not have been possible. I would also like to extend my appreciation to my committee members, Professors Peter Ford, Dan Little, and Ram Seshadri.

Some of the most rewarding learning experiences during my graduate tenure stemmed from opportunities to collaborate with Dr. Susan Hanson at Los Alamos National Laboratory. Her guidance molded me in the beginning of my graduate career and I am forever grateful for the opportunity to work with her.

I am greatly appreciative of Professor Jason Locklin for giving me my first research experience and for suggesting I attend graduate school at UCSB. I couldn't have imagined a better university and location to conduct my graduate research.

I've had the privilege to be a supported by NSF under the auspices of CENTC all 5+ years of graduate school. I am also thankful for fellowships through ConvEne IGERT and PIRE-ECCI that I've had during my graduate career, which enabled me to travel to Germany and China for research.

To all my friends, especially my Dailey method family, Randi Gbur, Agustin Pierri, Chelsea Dean, Gesine Veits, and Lauren Misch, thank you for providing a relief from the struggles of graduate school and making life outside of the lab so enjoyable. Jay thank you for being a part of my life and I look forward to what the future may bring.

Most importantly, I am thankful for the love and support of my amazing family, my parents, Will and Debra, brother, Nathanial and sisters, Abby and Hannah.

Chapter 2 is adapted with permission from John Wiley and Sons, Inc. Publisher (*Chem. Eur. J.* **2012,** *18*, 14981-14988). In Chapter 2, Dr. Michael Drummond at the University of North Texas performed DFT calculations. In Chapter 4, the silylalkylboranes were synthesized and characterized in collaboration with Raúl Adler-Yañez at the University of Münster. In Chapter 5, $[Cp^*Ir(OH_2)_3]OTf_2$ was prepared by Dr. Tim P. Brewster at the University of Washington, as well as the levulinic acid oxidation reactions. Dr. Jaime Flores prepared the phenylpyridyl (ppy) and bipyridyl (bpy) silanes also used in this chapter. Portions of this work made use of facilities of the Materials Research Laboratory, supported by the MRSEC Program of the National Science Foundation (No. DMR05-20415). This work was supported by the NSF under the auspices of the Center for Enabling New Technologies through Catalysis (CENTC) and the ConvEne IGERT

VITA OF BETHANY N. WIGINGTON

Education

2009-present Doctor of Philosophy in Chemistry, University of California, Santa Barbara, January 2015 (expected)

2004- 2008 Bachelor of Science in Chemistry (Honors), University of Georgia, Athens

Employment

2009-present Graduate Research Assistant, Dept. of Chemistry & Biochemistry, UC Santa Barbara

2008-2009 Scientific Research Assistant at the EPA in the Ecosystems Research & Development (ERD) division, Athens, GA

Awards and fellowships

- Best poster award at 25th Annual ORCS Conference, March 2014
- Associate of the NSF ConvEne IGERT program, 2009-2010
- Fellow of the NSF ConvEne IGERT program, 2010- 2012
- Fellow of the NSF Center for Enabling Technologies through Catalysis (CENTC), 2009-present
- MRL Travel Fellowship, spring 2012
- University of Georgia, Athens undergraduate research achievement award, 2008

Internships and collaborations

Summer 2012 University of Münster, Münster, Germany; Advisors: Prof. Gerhard Erker and Dr. Gerald Kehr: Frustrated-Lewis pair chemistry

January 2011 Suzhou Institute for Nanotechnology and Nanobionics (SINANO), Suzhou, China; Advisor: Prof. Jinping Zhang: TEM imaging

Summer 2010, 2011 Los Alamos National Laboratory (LANL), Los Alamos, NM; Advisors: Dr. David L. Thorn and Dr. Susan K. Hanson: Homogeneous Vanadium oxidations

Society Affiliations

Member of the American Chemical Society (ACS), 2008-present

Member of Graduate Students for Diversity in Science (UCSB), 2009-present

Presentations

- ACS Fall National Meeting, San Francisco, CA, *poster presentation*, August 2014
- 25th Annual Organic Reactions Catalysis Society (ORCS) Meeting, Tuscon, AZ, *poster presentation* March 2014
- Center for Enabling New Technologies through Catalysis (CENTC) Annual Meeting, Seattle, WA, *oral presentation* Sept. 2009, 2010, 2011; *poster presentation* Sept. 2014
- ACS Spring National Meeting, San Diego, CA, *poster presentation*, March 2012
- UCSB ConvEne IGERT winter symposium, UCSB, *oral presentation*, February 2012

- UCSB/UCLA ConvEne IGERT summer symposium, UCSB, *poster presentation*, August 2010
- Partnership in International Research and Education in Electron Chemistry and Catalysis at Interfaces, Suzhou, China, *oral presentation*, January 2011

Publications

3. B. N. Wigington, M. L. Drummond, T. R. Cundari, D. L. Thorn, S. K. Hanson, and S. L. Scott, A biomimetic pathway for Vanadium-catalyzed aerobic oxidation of alcohols: Evidence for a base-assisted dehydrogenation mechanism, *Chem. Eur. J.,* **18** (2012) 14981-14988. [doi]

2. M. H. Tucker, A. J.Crisci, B. Wigington, N. Phadke, R. Alamillo, J. Zhang, S. L Scott, and J. A. Dumesic, Acid-functionalized SBA-15-type periodic mesoporous organosilicas and their use in the continuous production of 5-Hydroxymethylfurfural, *ACS Catal.,* **2** (2012) 1865-1876.[doi]

1. Ma, X.; Wigington, B.; Bouchard, D**.**, Fullerene C60: surface energy and interfacial interactions in aqueous systems. *Langmuir* **26** (2010) 11886-11893. [doi]

ABSTRACT

Redox Reactions of Silica-Supported Complexes

and their Molecular Analogs

By

Bethany N. Wigington

Redox-active silica-supported catalysts can be used to create alternatives to stoichiometric (i.e., non-catalytic) processes that are widely used in oxidation reactions and often require toxic and/or environmentally-unfriendly reagants. Catalytically active metal sites can be introduced to a solid support either as part of the framework of porous materials during their synthesis (co-condensation), or through post-synthetic attachment. The strategy of catalyst immobilization emphasized in this work involves linking a metal complex to a silica material via a grafted spacer or tether. This approach requires modifying one of the ligands of the catalyst precursor with a functional group or linker capable of creating the anchor, via a covalent bond, to the silica support. Much of the synthetic effort is devoted to preserving structure and reactivity of the molecular complex upon anchoring.

In this work, three silica-supported complexes were prepared. Each was characterized in detail at each step of the attachment procedure, to verify the reaction and its completeness. The corresponding homogeneous catalysts were also prepared in order to make structural and reactivity comparisons.

First, we report a *bis*(8-hydroxyquinolinato)(2-propanato)oxovanadium(V) catalyst, $V(O)(HQ)_2(O^iPr)$, that selectively oxidizes alcohols under mild reaction conditions (60 °C, air) and operates via an unusual base-assisted mechanism. A silica-supported analog, $V(O)(HQ)_2(O^iPr)_x$-A380, was prepared via a multi-step grafting procedure and tested for catalytic aerobic oxidation under similar conditions as the homogeneous system. The activity of $V(O)(HQ)_2(O^iPr)_x$-A380 was much lower than that of $V(O)(HQ)_2(O^iPr)$, suggesting that the two are not precisely structurally equivalent. Further analysis reveals that during the grafting procedure, unexpected oxidation of the ligand tether occurred, giving rise to a V(IV) product.

In a separate study, we prepared two silylpropyl bis(pentafluorophenyl)boranes as molecular models for the Lewis acid component of supported frustrated Lewis pairs. The borane precursors were thoroughly characterized using NMR to confirm their structures, and to provide reference signals for silica-supported analogs. Three types of supported propyl bis(pentafluorophenyl)boranes, were prepared using a two-step methodology. First, allyl propylsilanes were installed, followed by hydroboration using Piers' borane to give tethered Lewis acid sites. As for molecular FLPs, combination with a Lewis base could lead to applications as heterogeneous metal-free catalysts for organic synthesis.

Lastly, two periodic mesoporous organosilicas (PMO) were synthesized by co-condensing either phenylpyridyl (ppy) silane or bipyridyl (bpy) silane, into the silica framework. The two materials were metalated using $Cp^*Ir(OH_2)_3(OTf)_2$ to give Cp*Ir-ppy-PMO and Cp*Ir-bpy-PMO, respectively, as supported analogs for the molecular catalysts $Cp^*Ir(ppy)(OTf)$ and $Cp^*Ir(bpy)(OTf)_2$. When tested in the catalytic oxidation of propionaldehye using water as the oxygen source (aldehyde-water shift catalysis, AWS), the

activities of the supported catalysts were comparable to those of the molecular systems, although all had the activities that are rather low. In spite of the low activity seen for AWS catalysis, Cp*Ir-ppy-PMO proved competent in the hydrogenation of levulinc acid.

We describe approaches for the design and synthesis of silica-supported molecular catalysts, using ligand anchoring techniques to create site-isolated, discrete catalyst.

TABLE OF CONTENTS

LIST OF FIGURES

LIST OF TABLES AND SCHEMES

Chapter 1. Introduction

1.1 Catalysis in Industry

Catalysis plays a pivotal role in chemical manufacturing, reducing energy use and increasing selectivity to maximize economic value and minimize environmental impact. More than 90 % of all chemical manufacturing processes employ catalysts, in areas as diverse as polymers, pharmaceuticals, agrochemicals and petrochemicals.[1] Among the catalysts used commercially, heterogeneous catalysts account for the largest fraction (80 %), followed by homogeneous catalysts (17 %) and enzymes (3 %).[2] The dominance of heterogeneous catalysts is attributed to their facile separation, compatibility with continuous processing, lower catalyst cost, and smaller reactor volume, which often lead to higher efficiency and lower operating costs. Homogeneous catalysts can suffer from difficult and costly separation and recovery, although in some cases they can offer increased activity and fewer mass transfer limitations compared to heterogeneous systems. An exception is homogeneous catalysis involving poorly soluble gases, such as O_2 or H_2, where mass transfer limitations can be considerable. In homogeneous catalysis, it is assumed that every single catalytic entity can show in principle the same reactivity. Although not always the case, this makes such catalysts intrinsically more selective than traditional heterogeneous catalysts with non-uniform sites, such as oxides or supported metal particles. While homogeneous catalysts have proven to be of high utility in small scale organic synthesis, the large-scale use of expensive molecular catalysts is often prohibitively expensive.

Recognizing the inherent limitations of homogeneous catalysts has led to efforts to support them. Immobilized molecular catalysts can, in principal, be created as well-defined complexes with custom ligand architectures attached to a support, thereby allowing the catalyst to reside in a different phase than the reaction substrate(s) and product(s). The goal is to combine the selectivity of the homogeneous catalyst with the easy separability of a heterogeneous system. Inorganic oxides are interesting supports for the immobilization of metal complexes, due to their high thermal and mechanical strength and large surface area. Immobilization can be achieved through a variety of methods, including those involving weak support–complex interactions, such as van der Waals forces or hydrogen bonds, and those involving strong electrostatic or covalent interactions, in which either the metal or one of the ligands participates directly in the interaction.[3] The robustness of the immobilization under reaction conditions is crucial, since a major drawback of supported catalysts is leaching during use and recycle, leading to deactivation.

Supported molecular catalysts can often be custom-designed with the precise ligand environment, oxidation state and nuclearity desired for a given reaction. Any organometallic complex can be used (transition metal, main group, rare earths) with a wide variety of supports (inorganic oxides, zeolites, metals). The activity of these catalysts is controlled by the catalyst loading. Site isolation and limited mobility of catalytically active molecules impede bimolecular decomposition reactions, and catalyst recovery becomes a simple matter of phase separation. Nevertheless, obtaining site-isolated catalytic centers with demonstrably precise compositions and structures remains an important challenge.[4] Since these are often multi-step syntheses, side-reactions and unstable intermediates can occur at any step, and are often difficult to detect.

Of the various methods used to support homogeneous catalysts, covalent attachment offers the greatest control of immobilization and, usually, the most resistance to leaching. Silica is a popular solid support due to its low cost, availability of different morphologies, mechanical robustness and accessible synthesis.[5] It has weak Brønsted acidity and no Lewis acidity. Silica consists of siloxane bridges (≡Si-O-Si≡) and silanol groups (≡Si-OH), the latter being located predominantly on the surface after high temperature calcination. Three types of silanol groups have been identified: isolated, vicinal and geminal, Fig. 1.1, each of which can serve as points of attachment for metal centers.

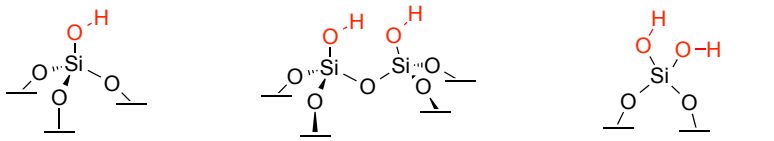

Figure 1.1 Schematic representation of types of silanol groups present on the silica surface.[6]

Thermally treating silica induces condensation of adjacent silanol groups to form siloxane bridges. This process is partially reversible upon hydration. Consequently, by varying the pretreatment temperature, the concentration of grafting sites (or silanols, ≡Si-OH) can be controlled, thereby offering the possibility to control the surface density of active sites.

1.2 Immobilization Strategies for Single-Site Heterogeneous Catalysts

Strategies to anchor metal complexes to silica through a covalent bond involve: linking the metal complex to the solid (*grafting*), synthesis of the ligand onto the support

followed by the metal center (*tethering*), or incorporation of the ligand or the complex during synthesis (*co-condensation*).

1.2.1 Post-synthesis Grafting and Tethering Methods

Grafting refers to attaching a metal center to a support through covalent-bonds to surface oxygen atom, while *tethering* requires that the hydroxyl groups react with a ligand-based functional group such as an alkoxy- or chlorosilane, Scheme 1.1.[7]

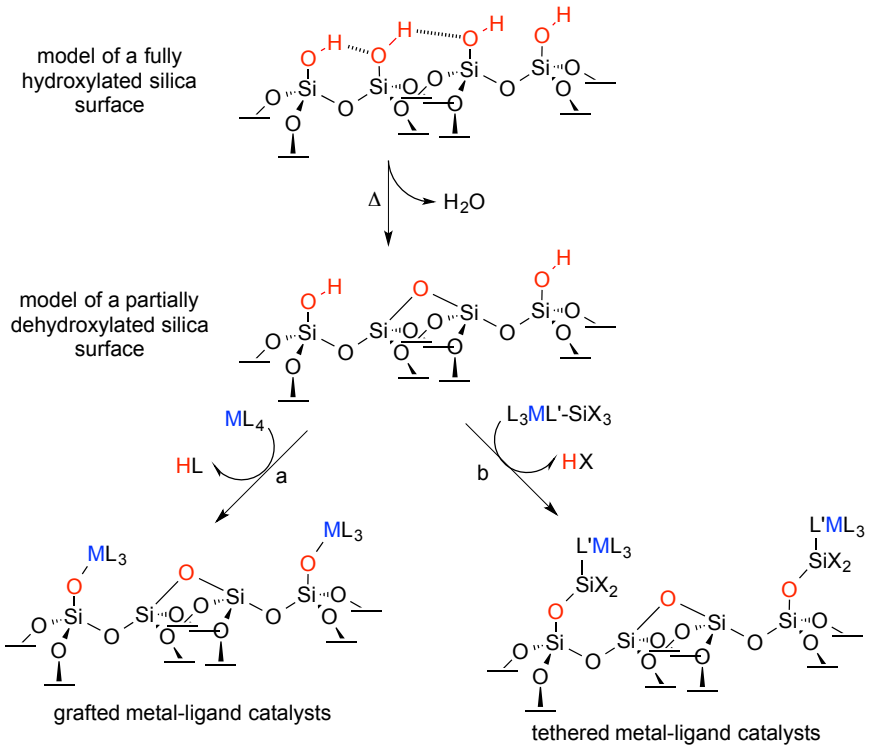

Scheme 1.1 Immobilization strategies on partially dehydroxylated silica surface: (a) *grafting*, via protonolysis of a metal-ligand bond; and (b) *tethering*, via protonolysis of an alkylsilane (X= Cl, OR). (L = ligand).[8]

During grafting, ligand protonolysis by surface hydroxyl groups leads to simultaneous formation of a metal-silanolate bond. These groups become part of the catalyst's inner coordination sphere and thus act as ligands. The grafted metal complex is generally bound through one or two bonds with the support, Fig. 1.2. The grafting reaction may change the symmetry, coordination number, and/or oxidation state of the metal center. This strategy has been frequently used to immobilize single-site olefin polymerization catalysts, such as organochromium, and/or alkylaluminum cocatalysts.[3] However, it is limited to complexes that tolerate oxygen atoms in the first coordination sphere of the metal.

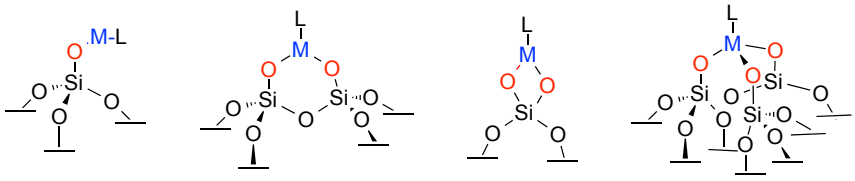

Figure 1.2 Modes of bonding for grafted metal complexes through surface oxygen atoms on a silica support. (L = ligand). Adapted from ref. 6.

An alternative approach involves grafting an organosilane bearing various functional groups through one or more oxygen atoms in the support. Initially, chlorosilanes were used for surface immobilization.[5] Trialkoxymonoalkylsilanes were developed for covalent attachment of homogeneous catalysts under milder conditions. The result is also mono- or dipodal anchoring. This is a consequence of the low probability that three silanols will occur in close enough proximity to interact with the same organosilane. However, this method does

facilitate the tethering of molecularly-diverse catalysts by further functionalization of the grafted silanes (e.g., to give phosphines, *N*-heterocycles, Schiff bases). Since the metal center is not covalently bonded to the support surface, but rather through a ligand tether, Scheme. 1.1, the coordination sphere of the anchored metal species is often assumed to be very similar to that of the precursor complex. However, unless the tether is very rigid, the possibility of metal-surface interactions can not be neglected, since they can have important consequences for reactivity. Furthermore, the tethering reactions are often multi-step processes involving additional catalysts and are usually not quantitative, which may lead to complications in later steps.

1.2.2 Sol-gel or Co-condensation Processes

Another immobilization approach, commonly used for preparing catalysts on ordered mesoporous silicas, is co-condensation. In this direct synthesis method, a trialkoxyorganosilane is typically added to an aqueous solution of a surfactant/templating agent and a tetraalkoxysilane. Condensation can occur under acid- or base-catalyzed conditions. Functional silanes are limited to those with organic groups that are soluble in water, and that tolerate the extreme pH conditions required for the silica synthesis and, where necessary, subsequent surfactant removal. The organosilicate ions must compete effectively with silicate ions for the interaction with surfactant micelles in order to be incorporated into the silica matrix. Consequently, functional groups introduced by co-condensation are often limited to less than 20 % organosilane incorporation to avoid compromising the ordered porous structure.[54] Incorporation of bulky organosilanes in particular interferes with silica condensation, lowering the stability of the silica mesopore structure. One strategy to increase

hydrophobicity and therefore structural stability under hydrothermal conditions is to use organodisilane precursors containing an organic bridging group R, Scheme 1.2. A benefit of co-condensation is a more homogeneous spatial distribution of organic groups in the silica material relative to post-synthesis grafting.[9-11]

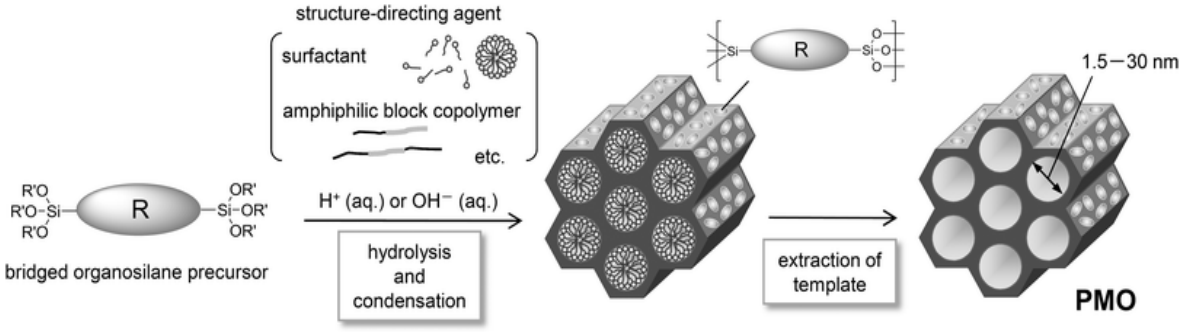

Scheme 1.2 Synthesis of a periodic mesoporous organosilica (PMO) from an organodisilane precursor.[12]

1.3 Characterizing Silica-supported Catalysts

One shortcoming of classical heterogeneous catalysis is the difficulty in developing a clear understanding of the structure of the "active sites" which, despite extensive studies, often remain unknown.[13] It is fundamentally important to characterize silica-supported metal complexes, both anchored and tethered, in order to establish structure-activity relationships. Much like their molecular counterparts, modified silica materials can be characterized using a variety of spectroscopic techniques, including IR, magic angle spinning NMR (MAS NMR), and EPR. The combination of these techniques with other readily available analytical tools can ultimately lead to a clearer understanding of the structure and reactivity of a given

material.

The work presented in this thesis focuses on the synthesis and reactivity of three different homogeneous and heterogeneous catalytic systems. Increasing demands for precious metal resources and the desire for first-row transition metal catalysts or metal-free systems for industrially-relevant redox reactions motivate this work. We describe approaches for the design and synthesis of silica-supported molecular catalysts, using ligand anchoring techniques to create site-isolated, discrete catalyst. We also describe another approach for preparing robust mesoporous silica materials containing anchored Ir or Rh catalysts. Throughout this work, we describe the use of incisive spectroscopic techniques, including solid-state NMR, Infrared spectroscopy, to characterize supported catalysts.

A silica-supported vanadium complex, $V(O)(HQ)_2(O^iPr)_x$-A380, was prepared In order to prevent the formation of bimolecular V-O-V species, which we believe leads to an inactive oxidation catalysts. We designed a multi-step reaction to achieve a ligand architecture on silica analogous to that of the homogeneous catalyst, $V(O)(HQ)_2(O^iPr)$, thereby preserving the coordination sphere. We characterized the tethered catalyst after each step and compared the structure to the molecular analog.

Preserving the structure of a catalyst throughout multi-step reactions can often be difficult especially if side reactions occur, which are often overlooked when the material is not thoroughly characterized. Silica-supported propyl bis(pentafluorophenyl)boranes were prepared using a two-step methodology. These materials are extremely sensitive to hydrolysis and undergo changes during storage probably due to adventitious water.

Catalysts with high hydrothermal stability can also be obtained using periodic mesoporous silicas (PMOs) possessing organosilanes co-condensed within the silica

framework. Two PMOs were prepared using either phenylpyridyl (ppy) or bipyridyl (bpy) silane, which were then were metalated with $Cp^*Ir(OH_2)_3(OTf)_2$. These materials were tested for aldehyde oxidation in water and compared to their homogeneous analogs.

1.4 References

1. Hegedus, L. L., . In *Catalyst Design: Progress and Perspectives*, Hegedus, L. L.; Rutherford, A., Eds. Wiley: New York, NY, 1987.

2. de Jong, K. P., Ed., *Synthesis of Solid Catalysts*. Wiley-VCH: Weinheim, Germany, 2009.

3. Fraile, J. M.; García, J. I.; Mayoral, J. A.; Pires, E., Heterogenization on Inorganic Supports: Methods and Applications. In *Heterogenized Homogeneous Catalysts for Fine Chemicals Production: Materials and Processes*, Barbaro, P.; Liguori, F., Eds. Springer: London, UK, 2010; pp 65-121.

4. Schwartz, J. A.; Contescu, C.; Contescu, A., *Chem. Rev*. **1995,** *95*, 477-510.

5. Trewyn, B. G.; Chen, H.-T.; Lin, V. S.-Y., Surface-functionalized Nanoporous Catalysts for Renewable Chemistry. In *Recoverable and Recyclable Catalysts*, Benaglia, M., Ed. Wiley-VCH: 2009; pp 15-47.

6. Copéret, C.; Chabanas, M.; Saint-Arroman, R. P.; Basset, J.-M., *Angew. Chem., Int. Ed*. **2003,** *42*, 156-181.

7. Hartley, F. R., *Supported Metal Complexes*. D. Reidel: Holland, 1985.

8. Fleischman, S. D.; Scott, S. L., *J. Am. Chem. Soc*. **2011,** *133*, 4847-4855.

9. Melde, B. J.; Holland, B. T.; Blanford, C. F.; Stein, A., *Chem. Mater*. **1999,** *11*, 3302-3308.

10. Hoffmann, F.; Cornelius, M.; Morell, J.; Fröba, M., *Angew. Chem., Int. Ed.* **2006,** *45*, 3216-3251.

11. Asefa, T.; MacLachlan, M. J.; Coombs, N.; Ozin, G. A., *Nature* **1999,** *402*, 867-871.

12. Mizoshita, N.; Tani, T.; Inagaki, S., *Chem. Soc. Rev.* **2011,** *40*, 789-800.

13. Ivin, K. J.; Mol, J. C., *In Olefin Metathesis and Metathesis Polymerization*. Academic Press: San Diego, 1997.

Chapter 2. A Biomimetic Pathway for Vanadium-Catalyzed Aerobic Oxidation of Alcohols: Evidence for a Base-assisted Dehydrogenation Mechanism

2.1 Abstract

The first step in the catalytic oxidation of alcohols by molecular O_2, mediated by homogeneous vanadium(V) complexes $LV^V(O)(OR)$, is ligand exchange. The unusual mechanism of the subsequent intramolecular oxidation of benzyl alcoholate ligands in the 8-hydroxyquinolinato (HQ) complexes $(HQ)_2V^V(O)(OCH_2C_6H_4$-*p*-X) involves intermolecular deprotonation. In the presence of triethylamine, complex **3** (X = H) reacts within an hour at room temperature to generate quantitatively $(HQ)_2V^{IV}(O)$, benzaldehyde (0.5 equiv) and benzyl alcohol (0.5 equiv). The base plays a key role in the reaction: in its absence, less than 12 % conversion was observed after 72 h. The reaction is kJ/mol and $\Delta S^{\ddagger}$ = (-169 ± 4) J/K•mol. first-order in both **3** and NEt_3, with activation parameters $\Delta H^{\ddagger}$ = (28 ± 4) A large kinetic isotope effect, 10.2 ± 0.55, was observed when the benzylic protons were replaced by deuterons. The effect of the benzyl alcoholate ligand's *para* substituent on the reaction rate was investigated via a Hammett plot, constructed using σ_p. From its slope, ρ = +(1.34 ± 0.18), a significant buildup of negative charge on the benzylic carbon in the transition state is inferred. These experimental findings, in combination with computational studies, support an unusual bimolecular pathway for the intramolecular redox reaction, in which the rate-limiting step is deprotonation at the benzylic C-H position. This base-assisted dehydrogenation (BAD) mechanism represents a biomimetic mechanism for transition metal-mediated alcohol

oxidations, differing from the previously identified hydride transfer and radical pathways. It suggests a new way to enhance the activity and selectivity of vanadium catalysts in a wide range of redox reactions, via control of the outer coordination sphere.

2.2 Introduction

The development of selective aerobic oxidation catalysts is desirable for the production of a variety of important fine chemical products.[1] Dioxygen is an oxidant with significant advantages over stoichiometric metal-based oxidants and even organic oxidants, including low cost, ready availability, low toxicity, and an environmentally benign reaction co-product (H_2O). Complexes of several noble transition metals, including Pd,[2-6] Rh,[7, 8] and Ru,[9-11] have proven to be versatile catalysts in a wide range of aerobic oxidation reactions. There is also strong interest in the design of oxidation catalysts based on Earth-abundant metals, such as V[12-18] and Cu.[19-22] However, these catalysts typically operate by very different redox mechanisms than their noble metal counterparts, showing greater propensity to engage in one-electron (radical) chemistry.[23, 24] Hence, an important factor in "reverse engineering" noble metal catalysts using base metals as their replacements is the potential selectivity issues arising from radical chemistry. In this context, it is interesting that Nature uses 3*d* metals like Fe and Cu to oxidize even the most inert C—H bonds selectively.[25-30] Metalloenzymes are adept at using both inner and outer coordination sphere interactions for controlling activity and selectivity. Nevertheless, most biomimetic approaches (with some notable recent exceptions)[31, 32] have emphasized inner coordination sphere chemistry.[33] Methods of inducing two-electron reactivity, long a hallmark of the 4*d* and 5*d* metals, via the participation of non-coordinated sites may be the key to a greater exploitation of 3*d* metals in catalysis.[34]

In view of these criteria, the rational design of environmentally benign oxidation catalysts requires a detailed understanding of the mechanisms of transition metal-mediated oxidations. This is illustrated in the recent development of Pd-based systems for aerobic alcohol oxidation, for which mechanistic insight into the role of ligand modulation and base promoters led to the design of robust, active, and selective catalysts.[2, 5, 6]

Aerobic oxidation by V-based catalysts may have an even wider substrate scope and application. Mild and selective vanadium-catalyzed oxidation of benzylic, allylic, and propargylic alcohols has been demonstrated.[35] Vanadium Schiff-base complexes are highly enantioselective catalysts for the aerobic oxidative kinetic resolution of α-hydroxy-esters, -amides, and -phosphonates at ambient temperature.[36-38] Vanadium complexes induce oxidative decarboxylation in certain hydroxy-carboxylic acids[39, 40] and α-amino acids,[41] desilylation of benzylic silanes,[42] as well as oxidation of lignin model compounds.[43, 44] However, the mechanisms of V-mediated oxidation are comparatively less well understood.

Facile interconversion of oxidation states (e.g., V^{V}, V^{IV} and V^{III}) can make it difficult to identify redox pathways. In alcohol oxidations, both hydrogen atom abstraction[16, 45] and hydride abstraction[14, 15, 17, 37, 38, 43, 44] by the vanadyl oxo ligand have been postulated. Littler and Waters proposed the former, based on indirect evidence of radical intermediates and the appearance of C-C bond fission products.[46-48] Similarly, Rocek and Aylward reported that VO_2^+ reacts with 2-ethyl-cyclobutanol by a radical pathway to give the ring-opened product, 4-hydroxyhexanal.[45] In other cases, the absence of ring scission products has been used to support hydride transfer pathways. For example, Toste et al. found that oxidation of (±)-methyl 2-hydroxy-2-(2-phenyl-cyclopropyl)acetate gave the corresponding ketone, ruling out a mechanism involving a carbinol radical.[17]

A few previous reports have suggested that bases can promote V-mediated alcohol oxidations. Ragauskas and co-workers studied the aerobic oxidation of activated benzylic and allylic alcohols catalyzed by $V^{IV}(O)(acac)_2$ in the presence of 1,4-diazabicyclo[2.2.2]octane (DABCO).[12, 13] Recently, some of us presented kinetic evidence for pyridine promotion of stoichiometric aliphatic alcohol oxidation by (dipic)$V^{V}(O)O^{i}Pr$ (H_2dipic = dipicolinic acid).[12, 13, 49] However, the pyridine dependence of the rate was complex, since the base also coordinates to the catalyst. We also reported that the 8-hydroxyquinolinolato complex, $(HQ)_2V^{V}(O)O^{i}Pr$ (**1**), catalyzes the aerobic oxidation of lignin model compounds, including benzylic alcohols, as well as allylic and propargylic alcohols (Scheme 2.1).[35] Catalytic activity in the presence of triethylamine was higher than for several other V catalysts.[35] Although no rate dependence on the base concentration was reported, there is no evidence that triethylamine binds to **1**, and there is no open coordination site for it to do so. Therefore, we chose this system to elucidate the role of the base in vanadium-catalyzed aerobic oxidation of alcohols.

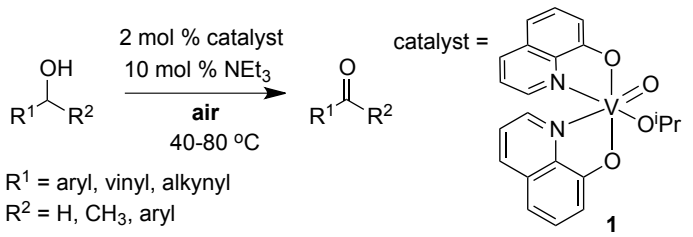

Scheme 2.1. Catalytic oxidation of benzylic, allylic, and propargylic alcohols by $(HQ)_2V^{V}(O)O^{i}Pr$ (**1**).

In this work, we present the combined results of our experimental (kinetics) and computational (density functional theory) studies on the key intramolecular redox step in catalytic

alcohol oxidation. For benzyl alcoholate complexes, we find that the base initiates the reaction by deprotonating the benzylic C—H bond. The result is an unusual base-assisted dehydrogenation, reminiscent of metalloenzyme pathways. It may have important ramifications for future catalyst development, by suggesting new ways to tune the activity and selectivity of vanadium catalysts for the oxidation of alcohols and other substrates.

2.3 Experimental Section

2.3.1 Reagents and Materials

General Considerations. Unless specified otherwise, all manipulations were carried out under a dry argon atmosphere using standard glove-box and Schlenk techniques. Deuterated solvents were purchased from Cambridge Isotope Laboratories and dried over CaH_2. Anhydrous acetonitrile, CH_2Cl_2, THF, and diethyl ether were obtained from Fisher Scientific and were used as received. 1,2-Dichloroethane and NEt_3 were dried over CaH_2. In addition, dichloroethane was stored over 4 Å molecular sieves. ^{1}H, ^{13}C, and ^{51}V NMR spectra were recorded at room temperature on Bruker AV400 and AV500 spectrometers as well as a Varian VNMRS 600 spectrometer. Chemical shifts (δ) were referenced internally to the residual solvent signal or externally to $VOCl_3$ (0 ppm). IR spectra were recorded on a Varian 1000 FT-IR Scimitar Series instrument. Complexes **1** and **2** were prepared as previously reported.[35] HR-MS spectra were recorded on a Micromass QTOF2 Quadrupole/Time-of-Flight Tandem mass spectrometer in the UCSB Mass Spectrometry Facility.

*2.3.2 Synthesis of $(HQ)_2V^V(O)(OCH_2C_6H_5)$ (**3**).*

Benzyl alcohol (466 mg, 4.31 mmol) and $(HQ)_2VO(O^iPr)$ (163 mg, 0.394 mmol) were dissolved in THF (2 mL). The reaction mixture was allowed to stand at room temperature for 20 min, then the solvent was removed under vacuum. The dark red residue was dissolved in THF (1 mL), and diethyl ether (10 mL) and pentane (3 mL) were added. Cooling the mixture to -20 °C overnight resulted in the formation of a dark red precipitate. After decanting the supernatant, the solid was washed with diethyl ether (2 x 2 mL) and dried under vacuum. Yield: 158 mg (87 %). ^{1}H NMR (400 MHz, CD_2Cl_2): δ 8.59 (d, 1H, *J* = 4.4 Hz, HQ), 8.43 (d, 1H, *J* = 3.6 Hz, HQ), 8.14 (d, 1H, *J* = 8.0 Hz, HQ), 8.04 (d, 1H, *J* = 8.0 Hz, HQ), 7.60-7.53 (m, 2H, HQ), 7.37-7.13 (m, 11H, HQ), 6.80 (d, 1H, *J* = 13.6 Hz, V-OC*H*H), 6.65 (d, 1H, *J* = 13.6 Hz, V-OCH*H*). ^{13}C{^{1}H} NMR (100 MHz, CD_2Cl_2): δ 164.8, 163.5, 146.7, 146.3, 144.5, 142.9, 141.8, 141.7, 139.9, 139.0, 137.9, 130.5, 130.4, 129.8, 129.3, 128.7, 127.9, 127.6, 122.7, 122.6, 118.4, 115.4, 111.9, 110.6, 90.1. ^{51}V NMR (105 MHz, CD_2Cl_2): δ -473 (s). IR: u(V=O) = 961 cm^{-1}. HRMS (ESI/TOF): *m/z* calcd for $C_{25}H_{19}N_2O_4V$ $[M+Na]^+$: 485.0682, found: 485.0661.

Complexes **4**-**7** were prepared following similar procedures to that described above for **3**.

*2.3.3 $(HQ)_2V^V(O)(OCH_2C_6H_4\text{-}p\text{-}CH_3)$ (**4**).*

Yield: 59.7 mg (92 %). ^{1}H NMR (400 MHz, CD_2Cl_2): δ 8.58 (br s, 1H, HQ), 8.42 (br s, 1H, HQ), 8.15 (d, 1H, *J* = 8.0 Hz, HQ), 8.05 (d, 1H, *J* = 8.4 Hz, HQ), 7.60-7.53 (m, 2H, HQ), 7.28-7.07 (m, 10H, HQ), 6.75 (d, 1H, *J* = 13.6 Hz, V-OC*H*H), 6.59 (d, 1H, *J* = 13.6 Hz, V-OCH*H*), 2.30 (s, 3H, CH_3). ^{13}C{^{1}H} NMR (100 MHz, CD_2Cl_2): δ 164.7, 163.4, 146.5, 146.1, 139.8, 138.8, 138.5, 137.7, 137.6, 130.4, 130.3, 129.6, 129.5, 129.3, 129.1, 127.7, 127.4, 122.5, 122.4, 118.1, 115.2, 111.7, 110.4, 105.4, 90.2, 21.3. ^{51}V NMR (105 MHz, CD_2Cl_2): δ -474 (s). IR (thin film): u(V=O) = 960 cm^{-1}. HRMS (ESI/TOF): *m/z* calcd for $C_{26}H_{21}N_2O_4V$ [M+Na]$^+$: 499.0839, found: 499.0812.

*2.3.4 $(HQ)_2V^V(O)(OCH_2C_6H_4\text{-}p\text{-}F)$ (**5**).*

Yield: 46 mg (82 %). ^{1}H NMR (400 MHz, CD_2Cl_2): δ 8.58 (d, 1H, *J* = 4.4 Hz, HQ), 8.42 (d, 1H, *J* = 4.0 Hz, HQ), 8.15 (d, 1H, *J* = 8.4 Hz, HQ), 8.05 (d, 1H, *J* = 8.4 Hz, HQ), 7.60-7.53 (m, 2H, HQ), 7.35-7.11 (m, 10H, HQ), 6.96 (t, 2H, aryl), 6.72 (d, 1H, *J* = 13.6 Hz, V-OC*H*H), 6.57 (d, 1H, *J* = 13.6 Hz, V-OCH*H*). ^{13}C{^{1}H} NMR (100 MHz, CD_2Cl_2): δ 164.6, 163.7, 163.3 (d, $^1J_{CF}$ = 200 Hz), 161.3 (d, $^1J_{CF}$ = 200 Hz), 146.5, 146.1, 141.6, 139.7, 138.9, 137.8, 137.5, 130.4, 130.3, 129.6, 129.4, 129.3, 129.1, 122.5, 122.4, 118.3, 115.4, 115.3, 115.2, 111.7, 110.3, 88.9. ^{51}V NMR (105 MHz, CD_2Cl_2): δ -474 (s). IR (thin film): u(V=O) = 960 cm^{-1}. HRMS (ESI/TOF): *m/z* calcd for $C_{25}H_{18}FN_2O_4V$ [M+Na]$^+$: 503.0588, found: 503.0562.

*2.3.5 $(HQ)_2V^VO(OCH_2C_6H_4\text{-}p\text{-}CF_3)$ (**6**).*

Yield: 45 mg (61 %). ^{1}H NMR (400 MHz, CD_2Cl_2): δ 8.58 (d, 1H, *J* = 4.4 Hz, HQ), 8.42 (d, 1H, *J* = 4.0 Hz, HQ), 8.15 (d, 1H, *J* = 8.4 Hz, HQ), 8.05 (d, 1H, *J* = 8.4 Hz, HQ), 7.60-7.53 (m, 2H, HQ), 7.35-7.11 (m, 10H, HQ), 6.96 (t, 2H, aryl), 6.72 (d, 1H, *J* = 13.6 Hz, V-OC*H*H), 6.57 (d, 1H, *J* = 13.6 Hz, V-OCH*H*). ^{13}C{^{1}H} NMR (150 MHz, CD_2Cl_2): δ 164.2, 162.6, 146.2, 145.6, 145.4, 141.2, 139.3, 138.5, 137.4, 130.6, 130.0, 129.9, 129.8 (q, $^1J_{CF}$ = 32 Hz), 128.7, 126.7, 126.0, 125. 22, 124.98 (q, $^1J_{CF}$ = 3.45 Hz), 124.4 (q, $^1J_{CF}$ = 272 Hz), 122.1, 122.0, 118.1, 114.9, 111.3, 109.9, 87.5. ^{51}V NMR (105 MHz, CD_2Cl_2): δ -477 (s). IR (thin film): u(V=O) = 960 cm^{-1}. HRMS (ESI/TOF): *m/z* calcd for $C_{26}H_{18}F_3N_2O_4V$ $[M+Na]^+$: 553.0556, found: 553.0530.

*2.3.6 $(HQ)_2V^V(O)(OCH_2C_6H_4\text{-}p\text{-}CN)$ (**7**).*

Yield: 64.8 mg (95 %). ^{1}H NMR (400 MHz, CD_2Cl_2): δ 8.58 (d, 1H, *J* = 4.5 Hz, HQ), 8.42 (d, 1H, *J* = 4.5 Hz, HQ), 8.15 (d, 1H, *J* = 8.0 Hz, HQ), 8.07 (d, 1H, *J* = 8.0 Hz, HQ), 7.60-7.53 (m, 2H, HQ), 7.41 (d, 2H, HQ), 7.34-7.11 (m, 2H, HQ), 6.73 (d, 1H, *J* = 14.5 Hz, V-OC*H*H), 6.61 (d, 1H, *J* = 14.5 Hz, V-OCH*H*). ^{13}C{^{1}H} NMR (125 MHz, CD_2Cl_2): δ 164.6, 163.3, 147.4, 146.7, 146.2, 141.7, 139.7, 139.0, 137.9, 132.7, 132.4, 130.5, 130.4, 129.6, 129.2, 127.5, 127.4, 122.6, 122.5, 119.4, 118.7, 115.5, 111.8, 111.2, 110.3, 87.6. ^{51}V NMR (105 MHz, CD_2Cl_2): δ -476 (s). IR (thin film): u(V=O) = 959 cm^{-1}. HRMS (ESI/TOF): *m/z* calcd for $C_{26}H_{18}N_3O_4V$ $[M+Na]^+$: 510.0635, found: 510.0610.

*2.3.7 Synthesis of α,α-d_2-benzyl alcohol (**9**).*

The synthesis of α,α-d_2 benzyl alcohol was carried out according to a reported literature procedure.[50] Yield: 88.6 mg (38 %). ^{1}H NMR (400 MHz, $CDCl_3$): δ 7.37 (m, 4H), 7.33-7.28 (m, 1H).

*2.3.8 Synthesis of $(HQ)_2V^V(O)(OCD_2C_6H_5)$ (**3-d_2**).*

The procedure was similar to that used for the synthesis of unlabeled **3**. Yield: 98 mg (97 %). ^{1}H NMR (500 MHz, CD_2Cl_2): δ 8.59 (d, 1H, *J* = 4.5 Hz, HQ), 8.43 (d, 1H, *J* = 4.5 Hz, HQ), 8.15 (d, 1H, *J* = 8.0 Hz, HQ), 8.05 (d, 1H, *J* = 8.5 Hz, HQ), 7.59-7.53 (m, 2H, HQ), 7.36-7.13 (m, 12H, HQ). ^{13}C{^{1}H} NMR (100 MHz, CD_2Cl_2): δ 164.7, 163.4, 146.5, 146.1, 141.6, 141.5, 139.8, 138.9, 137.8, 130.4, 130.3, 129.6, 129.1, 128.9, 128.6, 127.8, 127.6, 127.3, 122.5, 122.4, 118.2, 115.2, 111.7, 110.4, 89.2. ^{51}V NMR (105 MHz, CD_2Cl_2): δ -479.4 (s). IR (thin film): u(V=O) = 960 cm^{-1}. HRMS (ESI/TOF): *m/z* calcd for $C_{25}H_{17}D_2N_2O_4V$ $[M+Na]^+$: 488.0886, found: 487.0791.

2.3.9 Kinetics Experiments.

All experiments were carried out under Ar in 1,2-dichloroethane, using square quartz cuvettes (pathlength 1 cm) sealed with Teflon septum caps. In a typical experiment, NEt_3 was added via syringe to a thermally equilibrated cuvette containing 3 mL of a solution of the vanadium complex (0.3 – 0.4 mM). The concentration of NEt_3 was varied in the range 12 - 72

mM to evaluate its reaction order, then held constant at 24 mM for all other measurements. Reactions were initiated by the addition of NEt_3. The absorbance at 500 nm was recorded as a function of time, using an Agilent 8453 UV-visible spectrophotometer equipped with a Peltier thermostatted cell holder for complexes **2-5**. For complexes **6** and **7**, experiments were performed on a Shimadzu UV-2401PC spectrometer equipped with a TCC-240A thermoelectrically temperature-controlled cell holder. First-order rate constants were calculated by non-linear least-squares fitting (with uniform data weighting) of the integrated first-order rate equation, eq 4:

$$A_t = A_\infty + (A_0 - A_\infty) \exp(-k_{obs}t) \quad (4)$$

where A_∞ is the final absorbance at completion of the reaction, A_0 is the initial absorbance, A_t is the absorbance measured at time t, and k_{obs} is the pseudo-first-order rate constant.

2.3.10 Computational Methods.

The mechanism of the intramolecular redox reaction was investigated at the M06/6-311++(*d*,*p*) level of theory. Density functional theory (DFT) simulations employed the Gaussian 09 package.[51] The M06 functional[52] was used in conjunction with the extended Pople basis set, 6-311++G(*d*,*p*) and an ultrafine integration grid. [53-56]

All quoted energies are free energies calculated at 298.15 K and 1 atm, using unscaled vibrational frequencies. Stationary points were characterized as minima or transition states via calculation of the energy Hessian and observation of the correct number of imagi-

nary frequencies (zero or one, respectively). All geometry optimizations were performed without symmetry restraints. A restricted or unrestricted Kohn-Sham formalism was used for closed- and open-shell species, respectively. Both singlet and triplet energy surfaces were explored. The singlets were consistently lower in energy than the triplets by at least 84 kJ/mol; consequently, only singlet energies are reported here unless otherwise indicated.

2.4 Results

A rapid reaction takes place between $(HQ)_2V^V(O)O^iPr$ (**1**) and various *para*-substituted benzyl alcohols in either THF or CH_2Cl_2 at room temperature, eq 1. Ligand exchange generates $(HQ)_2V^V(O)(OCH_2C_6H_4$-*p*-X), where X is OCH_3 (**2**), H (**3**), CH_3 (**4**), F (**5**), CF_3 (**6**), or CN (**7**). Complexes **3** - **7** were characterized by ^{51}V, ^1H, and ^{13}C NMR, IR, and mass spectrometry; complex **2** has been reported previously.[35]

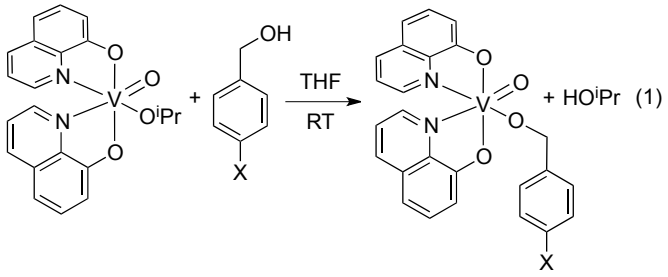

X = OCH_3 (**2**), H (**3**), CH_3 (**4**), F (**5**), CF_3 (**6**), CN (**7**)

Complexes **2-7** show characteristic signals in the ^1H NMR spectrum in the range 6.57 - 6.80 ppm, corresponding to the benzylic protons. These signals appear downfield from those of the free benzyl alcohols (4.57 - 4.77 ppm). Each complex gives one signal in the ^{51}V NMR spectrum. Differences in the ^{51}V chemical shifts are slight (ranging from -473 ppm for

2, to -477 ppm for **6**), but nevertheless correlate approximately with the electronic nature of the *para*-substituent. The IR spectrum of each complex contains a peak at 959 - 961 cm^{-1}, assigned to the □(V=O) mode.

2.4.1 Rate Law for the Intramolecular Redox Reaction.

In the absence of added base, complex **3** is relatively stable in CD_2Cl_2 at room temperature. For example, the ^1H NMR spectrum showed less than 12% reaction over the course of 72 h at 303 K. However, when NEt_3 (2 equiv) was added to a solution of **3** in 1,2-dichloroethane-d_4 in an NMR tube under Ar, the reaction proceeded readily (< 2 h) at room temperature to afford benzaldehyde (0.5 equiv, 100% yield), and benzyl alcohol (0.5 equiv, 100% yield), eq 2. The accompanying V^{IV} product, $(HQ)_2V^{IV}(O)$ (**8**), has been isolated and identified previously.[35]

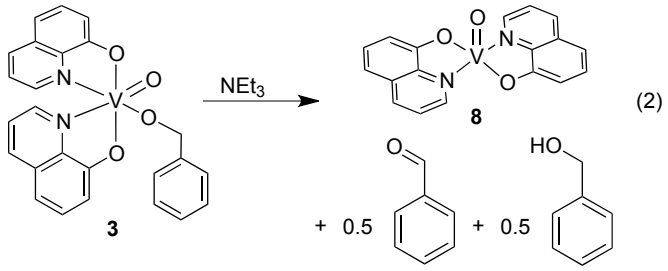

(2)

The kinetics of the intramolecular redox reaction of **3** in the presence of 24 mM NEt_3 in 1,2-dichloroethane at 303 K were monitored by UV-vis spectroscopy. A typical experiment is shown in Figure 2.1. There are two clean isosbestic points, at 382 and 426 nm, indicating quantitative conversion of **3** to **8** without accumulation of intermediates. The reaction is first-order in **3**, with $k_{obs} = (2.62 \pm 0.10) \times 10^{-3}$ s^{-1}, Figure 2.1 (inset). The linear dependence

of k_{obs} on the concentration of NEt_3 is shown in Table 2.1 and Figure 2.2. The rate law is therefore also first-order in NEt_3, eq 3:

$$-d[\mathbf{3}]/dt = k[NEt_3][\mathbf{3}] = k_{obs}\,[\mathbf{3}] \qquad (3)$$

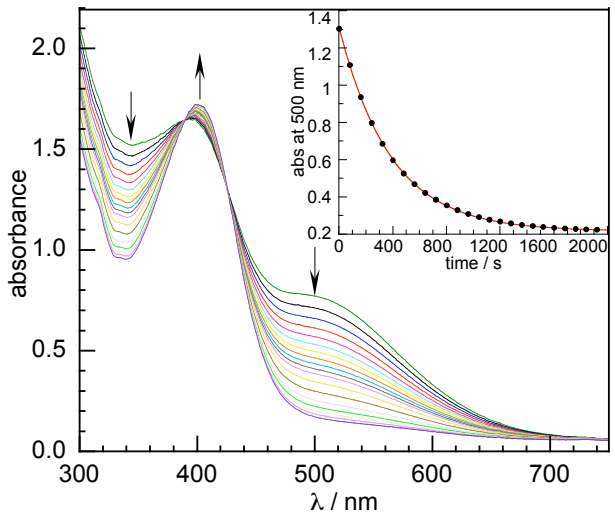

Figure 2.1. Time-resolved UV-vis spectra showing the redox reaction of 3 (0.34 mM) in the presence of NEt_3 (24 mM) in 1,2-dichloroethane at 303 K under Ar. Spectra were recorded at 20 s intervals over a period of 1 h. The inset shows the evolution of the absorbance at 500 nm as a function of time, as well as the curvefit obtained using the first-order rate equation.

Table 2.1. Dependence of k_{obs} for the redox reaction of **3** on the concentration of NEt_3 in 1,2-dichloroethane.

T (K)	[NEt_3] (mM)	10^3 k_{obs} (s^{-1}) [a]	10^2 k (M^{-1} s^{-1}) [b]
303	12	1.57 ± 0.13	
303	24	2.62 ± 0.10	10.9 ± 0.42
303	36	4.20 ± 0.60	
303	48	5.46 ± 1.05	
303	72	8.40 ± 0.80	
293	24	1.74 ± 0.31	7.2 ± 1.3
313	24	4.35 ± 0.68	18.1 ± 2.8
323	24	5.65 ± 0.77	23.6 ± 3.2
333	24	7.98 ± 0.81	33.2 ± 3.4

[a] Each value is the average of three independent experiments. The uncertainty is the standard deviation of the average. [b] Each value is the ratio of the averaged value of k_{obs} and the concentration of NEt_3. The uncertainty is the standard deviation of $k_{obs,}$ divided by 0.024 M.

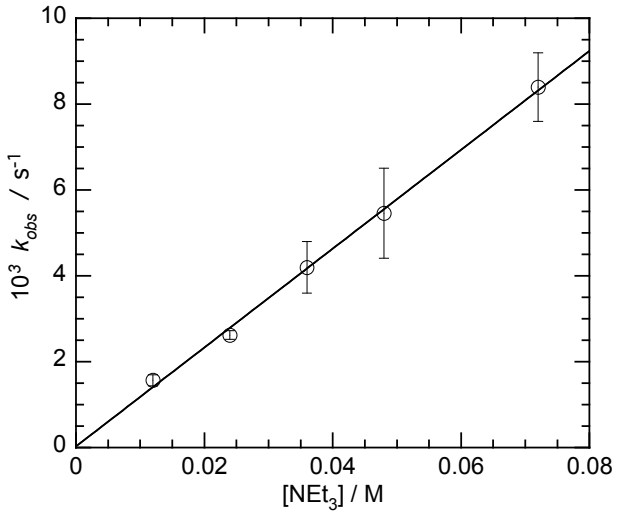

Figure 2.2. Dependence of the pseudo-first-order rate constants for the redox reaction of 3 on the concentration of NEt_3 in 1,2-dichloroethane at 303 K. Error bars are based on uncertainties reported in Table 2.1.

2.4.2 Activation Parameters.

The kinetics of the redox reaction of **3** were observed at several different temperatures, Table 2.1. The resulting Eyring plot, shown in Figure 2.3, yields $\Delta H^{\ddagger}$ = (28 ± 4) kJ/mol and $\Delta S^{\ddagger}$ = (-169 ± 4) J/K•mol.[57] The large, negative value for $\Delta S^{\ddagger}$ is consistent with a bimolecular reaction.

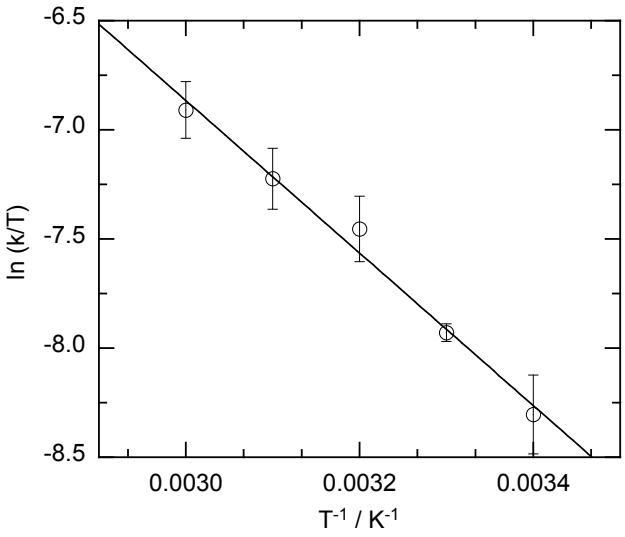

Figure 2.3. Eyring plot for the redox reaction of 3 in the presence of NEt_3 in 1,2-dichloroethane.

2.4.3 Kinetic Isotope Effect.

The selectively deuterated complex $(HQ)_2V^V(O)(CD_2C_5H_5)$ (**3**-d_2) was prepared by the reaction of **1** with α,α-d_2-benzyl alcohol in THF. At 303 K in 1,2-dichloroethane, the redox reaction of **3**-d_2 ($k = (1.07 \pm 0.04) \times 10^{-2}$ M^{-1} s^{-1}) is an order of magnitude slower than that of unlabeled **3** ($k = (10.9 \pm 0.42) \times 10^{-2}$ M^{-1} s^{-1}). The kinetic isotope effect, k_H/k_D, is therefore 10.2 ± 0.55. Its magnitude confirms that it is a primary kinetic isotope effect, suggesting that cleavage of a benzylic C-H bond occurs during the rate-determining step.

2.4.4 Para-Substituent Effects.

To probe electronic effects on the rate of the redox reaction, the kinetics were evaluated for each member of the series $(HQ)_2V^V(O)(OCH_2C_6H_4$-*p*-X), where X = OMe, CH_3, H,

F, CF_3, CN. The rate constants are given in Table 2.2, and the resulting Hammett plot, constructed using σ_p values,[58] is shown in Figure 2.4. The rate constants are very sensitive to the identity of the para substituent, with electron-withdrawing substituents enhancing the reaction rate. The large positive ρ value, +(1.34 ± 0.18), implies that negative charge develops on the benzylic carbon in the transition state.

Table 2.2. Dependence of the rate constant for the intramolecular redox reaction of $(HQ)_2V^V(O)OCH_2C_6H_4$-*p*-X, on the nature of the *para* substituent, X.[a]

Complex	X	σ_p [b]	10^2 *k* (M^{-1} s^{-1}) [c]
2	OCH_3	-0.27	5.46 ± 1.01
4	CH_3	-0.17	6.46 ± 0.16
3	H	0.00	10.9 ± 0.42
5	F	0.06	7.82 ± 0.46
6	CF_3	0.54	43.3 ± 1.67
7	CN	0.66	107 ± 1.68

[a] In 1,2-dichloroethane at 303 K. [b] Values from ref. 51. [c] Each value is the average of three independent experiments. The uncertainty is the standard deviation of the average.

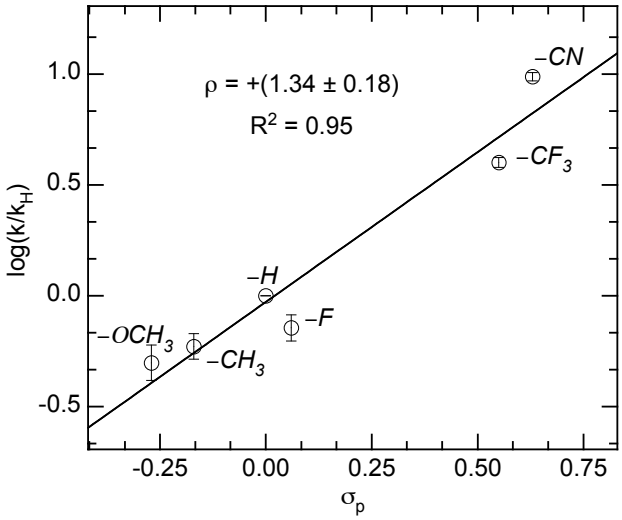

Figure 2.4. Hammett plot for the intramolecular redox reaction of $(HQ)_2V^V(O)OCH_2C_6H_4$-*p*-X, in 1,2-dichloroethane at 303 K.

2.4.5 Secondary Amines.

We also examined the redox reaction of **3** in the presence of HNR_2 (24 mM, 303 K). In all cases, the rate law is first-order in the secondary amine. The more basic $HNEt_2$ (pK_b = 3.07 in toluene) reacts faster than NEt_3 (pK_b = 3.33), with $k = (21.2 \pm 1.00) \times 10^{-2}$ M^{-1} s^{-1} vs. $k = (10.9 \pm 0.42) \times 10^{-2}$ M^{-1} s^{-1}, respectively. It is also more effective than the more basic, yet bulkier HN^iPr_2 (pK_b = 2.80 in toluene),[59] with $k = (10.5 \pm 2.46) \times 10^{-2}$ M^{-1} s^{-1}. When the even bulkier amine HN^iBu_2 (pK_b = 3.18) was used, the reaction was even slower ($k = (4.38 \pm 1.04) \times 10^{-2}$ M^{-1} s^{-1}) than with NEt_3. These differences in rate constants suggest that steric hindrance may play a role in the base-assisted mechanism, providing another means to tune this catalyst system.

2.4.6 Computational Modeling of the Reaction Mechanism.

DFT calculations on the singlet potential energy surface using the parent complex **3** gave a high free energy barrier, 132 kJ/mol, for direct intramolecular hydride transfer from the benzylic C-H bond of the alcoholate ligand to the oxo ligand at 298 K. In contrast, the calculated free energy barrier for a base-assisted pathway is more favorable, at only 94 kJ/mol. In this base-assisted dehydrogenation (BAD) mechanism, the benzylic C-H bond is deprotonated by NEt_3, yielding coordinated benzaldehyde and a formally V^{III} complex. A spin crossover from singlet to triplet also occurs at this stage, with the latter being more stable than the former by 71 kJ/mol. The protonated base, $HNEt_3^+$, subsequently approaches the oxo ligand and transfers a proton. This reaction is downhill, with no barrier. The resulting complex $(HQ)V^{III}(OH)(O{=}CHPh)$ presumably then comproportionates with **3** to generate the V^{IV} product **8** (eq 2), as previously proposed in a closely related system.[49] Calculated geometries for the transition states corresponding to intramolecular hydride transfer and the BAD mechanism are shown in Figure 2.4.

Computational modeling with $HNEt_2$ instead of NEt_3 revealed identical behavior, except that the free energy barrier for transfer of the benzylic proton to $HNEt_2$ was reduced to 79 kJ/mol. This is presumably because $HNEt_2$ also forms a hydrogen bond with the oxygen atom of a quinolinate ligand, resulting in a much closer approach to the active site than NEt_3 Figure 2.5c. Attempts to locate computationally a simultaneous mechanism, in which a proton is transferred to the oxo ligand while the benzylic site is being deprotonated, were unsuccessful, generally collapsing to stepwise transition states, although once indicating a highly unfavorable process with a barrier >188 kJ/mol.

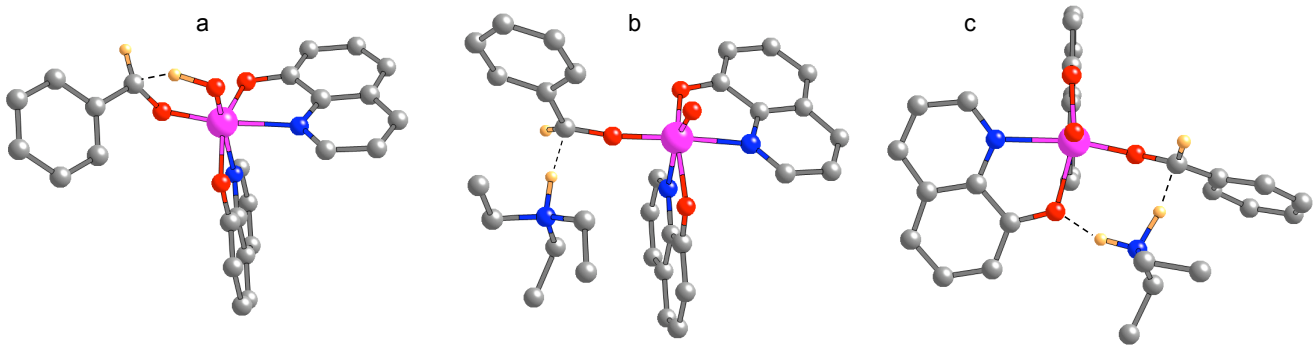

Figure 2.5. Calculated transition states in the redox reaction of **3**: (a) intramolecular hydride transfer to the vanadyl oxo ligand, and (b, c) base-assisted dehydrogenation by NEt_3 and $HNEt_2$. For (b), the distances Et_3N-H and $C_{benzyl}\cdots H$ are 1.17 and 1.59 Å, respectively. Most hydrogens have been omitted for clarity. Color scheme: V = magenta, N = blue, C = gray, O = red, H = orange.

A computational Hammett study was also performed to investigate para substituent effects for both potential reaction mechanisms. Complexes **2-6** were investigated, as was the complex with NO_2 as the para substituent. For the intramolecular hydride transfer mechanism, the correlation between σ_p and the calculated rate constants is weak ($R^2 = 0.22$), although consistent with slightly faster reactions for ligands with more electron-withdrawing para substiuents, $\rho = +(0.26 \pm 0.22)$ (see Supporting Information). For the intermolecular BAD mechanism, the correlation between σ_p and the calculated rate constant is significantly better ($R^2 = 0.98$) and the effect is much stronger: $\rho = +(2.86 \pm 0.19)$. Thus computations and experiment follow the same trend, with much greater rate acceleration occurring for electron-poor benzyl alcoholate ligands.

2.5 Discussion

Most metal-mediated alcohol oxidations that involve Brønsted bases as co-catalysts operate through a fundamentally different mechanism than that found in our study. Bases have proven to be important in both Cu-[20] and Pd-mediated[60] alcohol oxidations, where they serve to deprotonate alcohols coordinated to the metal at the –OH group, generating alkoxide complexes as intermediates prior to the redox step. Detailed mechanistic studies by Sigman and coworkers reported that bases play a dual role in Pd-catalyzed aerobic oxidation of secondary alcohols, both coordinating to the metal and deprotonating the coordinated alcohol.[61-64]

For our vanadium catalyst, the base instead plays a direct role in the redox step, abstracting a proton from the α-C-H bond of the alcoholate ligand, Scheme 2.2a. Calculations predict a free energy barrier for NEt_3-assisted deprotonation of **3** that is 38 kJ/mol lower than for direct hydride transfer to the oxo ligand. Extracting the enthalpic and entropic components of the free energy barriers reveals a higher enthalpic cost for intramolecular hydride transfer: $\Delta H^{\ddagger}$ is 49 kJ/mol lower for intermolecular base-assisted dehydrogenation (BAD). However, the bimolecular nature of the BAD mechanism also makes $\Delta S^{\ddagger}$ more negative, by 37 J/K•mol. Overall, the calculated activation free energy for the latter reaction is in reasonable agreement with the experimental value.

Based on these findings, we now propose an explanation for the complex rate-dependence of alcohol oxidation by (dipic)V^{V}(O)(OR) on pyridine concentration,[49] Scheme 2.2b. One pyridine equiv. occupies the open coordination site, while a second equiv. depro-

tonates the VOC-H bond. More basic substituted pyridines show significant rate enhancement for alcohol oxidation (ρ = -2.5), consistent with their role in this deprotonation step.

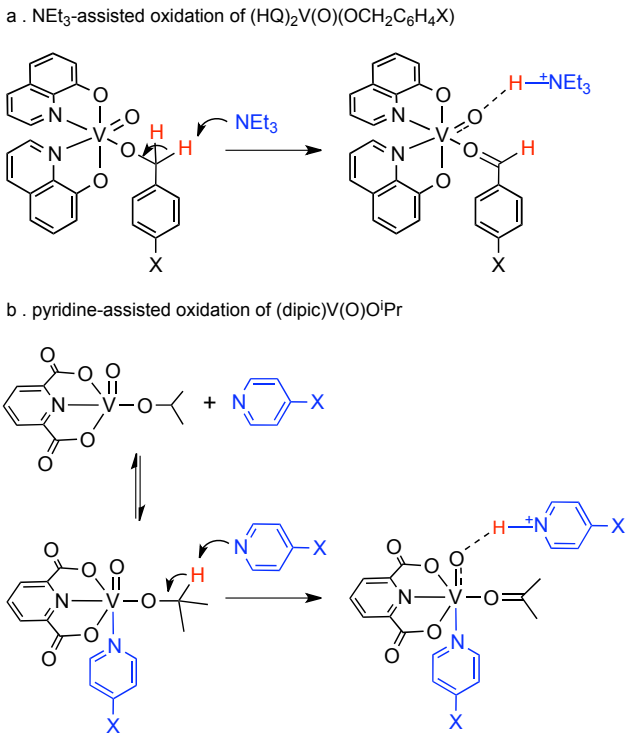

Scheme 2.2. Comparison of key steps in the intermolecular base-assisted dehydrogenation for two different LV(O)OR complexes, without and with an open coordination site.

The proposed reaction mechanism for $(HQ)_2V(O)(OR)$ is also supported by the large positive experimental and calculated Hammett parameters for *para*-substituted benzyl alcohols. In contrast, most prior Hammett studies of benzylic alcohol oxidations involving metal-based oxidants report negative ρ values.[65] For example, in the oxidation of benzylic alcohols by either $RuCl_2(PPh_3)_3$/TEMPO[66] or (neocuproine)$Pd(OAc)_2$,[67] the ρ value was determined to

be -0.58 in each case, signifying positive charge buildup on the benzylic carbon in the transition state due to rate-limiting β-hydride elimination. When a high-valent iron-oxo complex was used to oxidize *para*-substituted benzyl alcohols, the reaction rate was not greatly influenced by the nature of the para-substituent.[68, 69] Poor correlations with conventional Hammett σ and/or σ^+ values are usually attributed to radical character at the benzylic position in the transition state.[69] For the vanadium-mediated alcohol oxidation studied here, plotting the rate as a function of σ•-values revealed no correlation, inconsistent with the potential involvement of benzyl radicals.[70]

Few reported transition metal complex-mediated alcohol oxidations exhibit positive ρ values, and none are strongly positive. Sigman and Jensen reported a negligible ρ (+0.03) in the $Pd(OAc)_2$-catalyzed aerobic oxidation of benzyl alcohols.[71] Recently, Guzei and coworkers observed the oxidation of primary and secondary benzylic alcohols by a tetrametallic ruthenium-oxo-hydroxo-hydride complex.[65] While the Hammett correlation for the oxidation of secondary alcohols suggested negative charge development on the benzylic carbon (ρ = +0.22), primary alcohols displayed the opposite trend (ρ = -0.45).[65]

The base-assisted dehydrogenation pathway reported here resembles that of certain enzymatic oxidations, for which crystallographic and biochemical analyses suggest that the rate is highly dependent on the presence of specific catalytic residues near the active site, which act as proton acceptors.[72] For example, the mechanism proposed for benzylamine oxidation by bovine serum amine oxidase involves proton abstraction by an active-site base (aspartate),[73] affording a carbanion intermediate with partial delocalization of the negative charge into the aromatic ring of the substrate. A similar mechanism involving aspartate was

proposed for the oxidation of benzyl alcohols and amines by methylamine dehydrogenase, which showed an increase in rate with electron-withdrawing *para*-substituents.[73, 74] The reported ρ value, +1.47, is very similar to the value measured here.

Finally in recent work, DuBois and Bullock demonstrated the ability of pendant bases in the second coordination sphere of nickel complexes to facilitate proton movement,[75, 76] reminiscent of the proton conduction channels in the active sites of hydrogenase enzymes. Pendant amines promote H_2 activation by acting as proton relays, lowering the energy barrier to transfer protons to and from the catalytically active metal site.[75] DuBois and Kubiak have shown that these complexes are also electrocatalysts for formate oxidation.[77] Electrochemical and spectroscopic studies suggested rate-determining proton transfer within the Ni-formate complex to a pendant amine ligand, avoiding direct hydride transfer to the metal. This β-deprotonation is a multi-site proton-coupled electron transfer (MS-PCET). Similar to the base-assisted dehydrogenation pathway postulated here, it involves the initial movement of a proton and then two electrons to two separate sites.[78]

2.6 Conclusions

Experimental and computational studies agree that the mechanism of the redox reaction of **3** involves a bimolecular reaction between the vanadium complex and an external base. The two-electron redox process involves deprotonation of the benzylic position by NEt_3 in the rate-determining step, followed by the transfer of the proton from $HNEt_3^+$ to the vanadyl oxo ligand. Thus the overall intramolecular redox reaction is in fact intermolecular, mediated by a redox-inactive co-catalyst. Compared to most transition metal-catalyzed alcohol

oxidations, this mechanism is highly unusual. However, it does resemble those proposed for certain metalloenzyme-catalyzed oxidations.[73, 74] These mechanistic insights indicate that highly active and selective oxidation catalysts may be designed by using external bases as co-catalysts, or by designing supporting ligands with appropriately positioned pendant bases to serve as proton shuttles.

2.7 References

1. Hudlick, M., *Oxidations in Organic Chemistry*. American Chemical Society: Washington, D. C., 1990.

2. Aldea, R.; Alper, H., *J. Org. Chem.* **1995,** *60*, 8365-8366.

3. Blackburn, T. F.; Schwartz, J., *J. Chem. Soc., Chem. Commun.* **1977,** *5*, 157-158.

4. Ferreira, E. M.; Stoltz, B. M., *J. Am. Chem. Soc.* **2001,** *123*, 7725-7726.

5. Schultz, M. J.; Adler, R. S.; Zierkiewicz, W.; Privalov, T.; Sigman, M. S., *J. Am. Chem. Soc.* **2005,** *127*, 8499-8507.

6. Stahl, S. S., *Angew. Chem. Int. Ed.* **2004,** (43), 3400-3420.

7. Liu, L.; Yu, M.; Wayland, B. B.; Fu, X., *Chem. Commun.* **2010,** *46*, 6353-6355.

8. Mimoun, H.; Perez-Machirant, M. M.; Sérée de Roch, I., *J. Am. Chem. Soc.* **1978,** *100*, 5437-5444.

9. Bilgrien, C.; Davis, S.; Drago, R. S., *J. Am. Chem. Soc.* **1987,** *109*, 3786-3787.

10. Markó, I. E.; Giles, P. R.; Tsukazaki, M.; Chellé-Regnaut, I.; Urch, C. J.; Brown, S. M., *J. Am. Chem. Soc.* **1997,** *119*, 12661-12662.

11. Takezawa, E.; Sakaguchi, S.; Ishii, Y., *Org. Lett.* **1999,** *1* (713-715), 713.

12. Jiang, N.; Ragauskas, A. J., *Tetrahedron Lett*. **2006,** *48*, 273-278.

13. Jiang, N.; Ragauskas, A. J., *J. Org. Chem*. **2007,** *72*, 7030-7033.

14. Maeda, Y.; Kakiuchi, N.; Matsumura, S.; Nishimura, T.; Kawamura, T.; Uemura, S., *J. Org. Chem*. **2002,** *67*, 6718-6724.

15. Maeda, Y.; Kakiuchi, N.; Matsumura, S.; Nishimura, T.; Uemura, S., *Tetrahedron Lett*. **2001,** *42*, 8877-8879.

16. Ohde, C.; Limberg, C., *Chem. Eur. J*. **2010,** *16*, 6892-6899.

17. Radosevich, A.; Musich, C.; Toste, F. D., *J. Am. Chem. Soc*. **2005,** *127*, 1090-1091.

18. Velusamy, S.; Punniyamurthy, T., *Org. Lett*. **2004,** *6*, 217-219.

19. Chaudhuri, P.; Hess, M.; Florke, U.; Wieghardt, K., *Angew. Chem. Int. Ed*. **1998,** *37*, 2217-2220.

20. Gamez, P.; Arends, I. W. C. E.; Reedijk, J.; Sheldon, R. A., *Chem. Commun*. **2003,** *19*, 2414-2415.

21. Jiang, N.; Ragauskas, A. J., *J. Org. Chem*. **2003,** *71*, 7087-7090.

22. Michel, C.; Belanzoni, P.; Gamez, P.; Reedijk, J.; Baerends, E. J., *Inorg. Chem*. **2009,** *48*, 11909-11920.

23. Chirik, P. J.; Wieghardt, K., *Science* **2010,** *327*, 794.

24. Dzich, W. I.; van der Vlugt, J. I.; Reek, J. N. H.; de Bruin, B., *Angew. Chem. Int. Ed*. **2011,** *50*, 3356-3358.

25. Costas, M.; Mehn, M. P.; Jensen, M. P.; Que Jr., L., *Chemical Reviews* **2004,** *104*, 939-986.

26. Himes, R. A.; Karlin, K. D., *Curr. Opin. Chem. Biol*. **2009,** *13*, 119-131.

27. Kirillov, A. M.; Kopylovich, M. N.; Kirillova, M. V.; Haukka, M.; Guedes da Silva, M. F. C.; Pombeiro, A. J. L., *Angew. Chem. Int. Ed.* **2009,** *44*, 4345-4349.

28. Mas-Ballesté, R.; Costas, M.; van den Berg, T.; Que Jr., L., *Chem. Eur. J.* **2006,** *12*, 7489-7500.

29. Merkyx, M.; Kopp, D. A.; Sazinsky, M. H.; Blazyk, J. L.; Müller, J.; Lippard, S. J., *Angew. Chem. Int. Ed.* **2001,** *40* (15), 2782-2807.

30. Que Jr., L.; Tollman, W. B., *Nature* **2008,** *455*, 333-340.

31. Askevold, B.; Roesky, H. W.; Schneider, S., *ChemCatChem* **2012,** *4*, 307-320.

32. Grützmacher, H., *Angew. Chem. Int. Ed.* **2008,** *47*, 1814-1818.

33. Lippard, S. J.; Berg, J. M., *Principles of Bioinorganic Chemistry*. University Science Books: Mill Valley, CA, 1994.

34. Tondreau, A. M.; Hojilla Atienza, C. C.; Weller, K. J.; Nye, S. A.; Lewis, K. M.; Delis, J. G. P.; Chirik, P. J., *Science* **2012,** *335*, 567-570.

35. Hanson, S. K.; Wu, R.; Silks, L. A., *Org. Lett.* **2011,** *13*, 1908-1911.

36. Blanc, A.; Toste, F. D., *Angew. Chem. Int. Ed.* **2006,** *45*, 2096-2099.

37. Pawar, V. D.; Bettigeri, S.; Weng, S. S.; Kao, J. Q.; Chen, C. T., *J. Am. Chem. Soc.* **2006,** *128*, 6308-6309.

38. Weng, S.; Shen, M.; Kao, J.; Munot, Y. S.; Chen, C., *Proc. Nat. Acad. Sci.* **2006,** *103* (3522-3527), 3522.

39. Meier, I. K.; Schwartz, J., *J. Am. Chem. Soc.* **1989,** *111*, 3069-3070.

40. Meier, I. K.; Schwartz, J., *J. Org. Chem.* **1990,** *55*, 5619-5624.

41. Hirao, T.; Ohshiro, Y., *Tetrahedron Lett.* **1990,** *31*, 3917-3918.

42. Hirao, T.; Fujii, T.; Ohshiro, Y., *Tetrahedron Lett.* **1994,** *35*, 8005-8008.

43. Sedai, B.; Diaz-Urrutia, C.; Baker, R. T.; Wu, R.; Silks, L. A.; Hanson, S. K., *ACS Catal*. **2010,** *1*, 794-804.

44. Son, S.; Toste, F. D., *Angew. Chem. Int. Ed*. **2010,** *49*, 3791-3794.

45. Rocek, J.; Aylward, D. E., *J. Am. Chem. Soc*. **1975,** *97*, 5452.

46. Littler, J. S.; Waters, W. A., *J. Chem. Soc*. **1959**, 4046-4052.

47. Littler, J. S.; Waters, W. A., *J. Chem. Soc*. **1959**, 1299-1305.

48. Littler, J. S.; Waters, W. A., *J. Chem. Soc*. **1960**, 2767-2772.

49. Hanson, S. K.; Baker, T. R.; Gordon, J. C.; Scott, B. L.; Silks, L. A.; Thorn, D. L., *J. Am. Chem. Soc*. **2010,** *132*, 17804-17816.

50. Coon, M. J.; Vaz, A. D. N., *Biochemistry* **1994,** *33*, 6442-6449.

51. Gaussian 09; Revision A. 1; Frisch, M. J.; Trucks, G. W.; Schlegel, H. B.; Scuseria, G. E.; Robb, M. A.; Cheeseman, J. R.; Scalmani, G.; Barone, V.; Mennucci, B.; Petersson, G. A.; Nakatsuji, H.; Caricato, M.; Li, X.; Hratchian, H. P.; Izmaylov, A. F.; Bloino, J.; Zheng, G.; Sonnenberg, J. L.; Hada, M.; Ehara, M.; Toyota, K.; Fukuda, R.; Hasegawa, J.; Ishida, M.; Nakajima, T.; Honda, Y.; Kitao, O.; Nakai, H.; Vreven, T.; Montgomery, J., J. A.; Peralta, J. E.; Ogliaro, F.; Bearpark, M.; Heyd, J. J.; Brothers, E.; Kudin, K. N.; Staroverov, V. N.; Kobayashi, R.; Normand, J.; Raghavachari, K.; Rendell, A.; Burant, J. C.; Iyengar, S. S.; Tomasi, J.; Cossi, M.; Rega, N.; Millam, N. J.; Klene, M.; Knox, J. E.; Cross, J. B.; Bakken, V.; Adamo, C.; Jaramillo, J.; Gomperts, R.; Stratmann, R. E.; Yazyev, O.; Austin, A. J.; Cammi, R.; Pomelli, C.; Ochterski, J. W.; Martin, R. L.; Morokuma, K.; Zakrzewski, V. G.; Voth, G. A.; Salvador, P.; Dannenberg, J. J.; Dapprich, S.; Daniels, A. D.; Farkas, Ö.; Foresman, J. B.; Ortiz, J. V.; Cioslowski, J.; Fox, D. J. Gaussian, Inc.: Wallingford, CT, 2009.

52. Zhao, Y.; Truhlar, D. G., *Acc. Chem. Res.* **2008,** *41*, 157.

53. Hay, P. J., *J. Chem. Phys.* **1977,** *66*, 4377.

54. Krishnan, R.; Binkley, J. S.; Seeger, R.; Pople, J. A., *J. Chem. Phys.* **1980,** *72*, 650.

55. McLean, A. D.; Chandler, G. S., *J. Chem. Phys.* **1980,** *72*, 5639.

56. Wachters, A. J. H., *J. Chem. Phys.* **1970,** *52*, 1033.

57. Morse, P. M. S., M. D.; Wilson, S. R.; Girolami, G.S., *Organometallics* **1994,** *13*, 1646-1655.

58. McDaniel, D. H.; Brown, H. C., *J. Org. Chem.* **1958,** *23*, 420-427.

59. Christensen, J. J.; Izatt, R. M.; Wrathall, D. P.; Hansen, L. D., *J. Chem. Soc. A* **1969**, 1212-1223.

60. Bäckvall, J.-E., *In Modern Oxidation Methods*. Wiley-VCH: Weinheim, Germany, 2004.

61. Jensen, D. R.; Pugsley, J. S.; Sigman, M. S., *J. Am. Chem. Soc.* **2001,** *123*, 7475-7476.

62. Mandal, S. K.; Sigman, M. S., *J. Org. Chem.* **2003,** *68*, 7535-7537.

63. Mueller, J. A.; Jensen, D. R.; Sigman, M. S., *J. Am. Chem. Soc.* **2002,** *124*, 8202-8203.

64. Mueller, J. A.; Sigman, M. S., *J. Am. Chem. Soc.* **2003,** *125*, 7005-7013.

65. Yi, C. S.; Zeczycki, T. N.; Guzei, I. A., *Organometallics* **2006,** *25*, 1047-1051.

66. Dijksman, A.; Marino-Gonzalez, A.; Mairata i Payeras, A.; Arends, I. W. C. E.; Sheldon, R. A., *J. Am. Chem. Soc.* **2001,** *123*, 6826-6833.

67. ten Brink, G.-J.; Arends, I. W. C. E.; Hoogenraad, M.; Verspui, G.; Sheldon, R. A., *Adv. Synth. Catal.* **2003,** *345*, 497-505.

68. Newcomb, M.; Zhengzheng, P., *Inorg. Chem.* **2007,** *46*, 6767-6774.

69. Oh, N. Y.; Suh, Y.; Parks, M. J.; Seo, M. S.; Kim, J.; Nam, W., *Angew. Chem. Int. Ed.* **2005,** *117*, 4307-4311.

70. Creary, X.; E., M.-M. M.; S., M., *J. Org. Chem.* **1987,** *52*, 3254-3263.

71. Sigman, M. S.; Jensen, D. R., *Acc. Chem. Res.* **2006,** *39*, 221-229.

72. Bartlett, G. J.; Porter, C. T.; Borkakoti, N.; Thornton, J. M., *J. Mol. Biol.* **2002,** *324*, 105-121.

73. Hartmann, C.; Klinman, J. P., *Biochemistry* **1991,** *30*, 4605-4611.

74. Davidson, V. L.; Jones, L. H.; Graichen, M. E., *Biochemistry* **1992,** *31*, 3385-3390.

75. DuBois, D. L.; Bullock, M. R., *Eur. J. Inorg. Chem.* **2011,** *7*, 1017-1027.

76. O'Hagan, M.; Shaw, W. J.; Raugei, S.; Chen, S.; Yang, J. Y.; Kilgore, U. R.; DuBoise, D. L.; Bullock, M. R., *J. Am. Chem. Soc.* **2011,** *133*, 14301-14312.

77. Galan, B. R.; Schoffel, J.; Linehan, J. C.; Seu, C.; Appel, A. M.; Roberts, J. A. S.; Helm, M. L.; Kilgore, U. J.; Yang, J. Y.; DuBois, D. L.; Kubiak, C. P., *J. Am. Chem. Soc.* **2011,** *133*, 12767-12779.

78. Seu, C. S.; Appel, A. M.; Doud, M. D.; DuBois, D. L.; Kubiak, C. P., *Energy Environ. Sci.* **2012,** *5*, 6480-6490.

Chapter 3:

Silica-Supported Vanadium Catalysts for the Selective Aerobic Oxidation of Alcohols

3.1 Introduction

In Chapter 2, we reported a homogeneous *bis*(8-hydroxyquinolinato)(2-propanato) oxovanadium(V) catalyst that selectively oxidizes alcohols under mild reaction conditions (60 °C, air) and operates via an unusual base-assisted mechanism.[1] In practice, the productivity of such catalysts is limited by their tendency to form catalytically inactive oxo-bridged species. Immobilizing molecular complexes prevents such bimolecular reactions, thus potentially making them more robust. Anchoring metal complexes on solid supports offers additional advantages over their homogeneous counterparts such as easy separation of the catalyst from products and catalyst reuse, as well as the potential for application in flow reactors.

In this Chapter, we describe a molecular precursor approach involving multi-step grafting onto amorphous silica to produce a site-isolated vanadium complex. Careful ligand modification and tethering are desirable in order to maintain catalytic activity. We therefore attempted to prepare a supported catalyst for the oxidative dehydrogenation of alcohols by tethering an 8-hydroxyquinoline ligand to silica, Fig. 3.1. The nature of the surface-bound ligand and the resulting metal complex were investigated using IR and solid-state NMR (^{51}V MAS, ^{13}C CP/MAS and ^{29}Si CP/MAS) spectroscopies. Its catalytic activity in the aerobic oxidation of benzyl alcohol was evaluated, and compared to that of the homogeneous analog. The ability of the silica support to prevent deactivation was also explored.

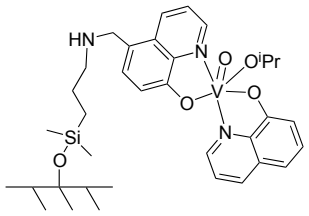

Figure 3.1. Desired silica-supported analog of the homogeneous $V(O)(HQ)_2(O^iPr)$ catalyst for aerobic alcohol oxidation.

3. 2 Experimental Section

3.2.1 Reagents and Materials

Unless specified otherwise, all manipulations were carried out under a dry Ar or N_2 atmosphere, using standard glove-box and Schlenk techniques. Deuterated solvents were purchased from Cambridge Isotope Laboratories and dried over CaH_2. (Aminopropyl)(dimethyl)ethoxysilane (APDES) was purchased from Gelest and used as received. 8-Hydroxyquinoline (HQ), diisopropylethylamine (DIPEA), formaldehyde (30 wt% in water), *tert*-butyl hydroperoxide (5.5 M in decane), and oxotris(propan-2-olato)vanadium ($V(O)(O^iPr)_3$) were purchased from Aldrich. 5-Chloromethyl-8-hydroxyquinoline hydrochloride (5-CHQ•HCl) was prepared according to a literature procedure.[2] N_2O (99%) was purchased from Praxair and used as received. Anhydrous 1,2-dichloroethane (1,2-DCE), acetonitrile (CH_3CN) and chloroform ($CHCl_3$) were obtained from Aldrich and used as received. Triethylamine (NEt_3) and diethylamine ($HNEt_2$) (both from Aldrich) were dried over CaH_2, degassed by several freeze-pump-thaw cycles and vapor-transferred to an air-free Schlenk tube, where they were stored over 3 Å molecular sieves prior to use. Toluene (Aldrich) was purified by passage through a drying column containing alumina and a

deoxygenating column packed with CuO/Al_2O_3 (Q5 catalyst, Vac-Atm). Dichloromethane (CH_2Cl_2) was purified by passage through two Q5 columns.

A non-porous, fumed Aerosil silica (A380), with a surface area of ca. 380 m^2/g and a primary particle size of 7 nm, was supplied by Evonik. It was thermally pretreated under vacuum (10^{-4} Torr) at 500 °C for 18 h. The resulting silica is denoted A380-500. It contains 0.89 mmol/g ≡SiOH, as measured by $VOCl_3$ chemisorption. The absence of physisorbed water was confirmed by the complete disappearance of the bending mode δ(HOH) at ca. 1635 cm^{-1} in the IR spectrum. All dry materials were stored in an Ar-filled glove box to prevent readsorption of atmospheric moisture.

3.2.2 Characterization

Solution-state NMR spectra were recorded on a Bruker DMX 500 MHz spectrometer, equipped with a 5 mm BBFO 1H-F/X probe, and referenced to $Si(CH_3)_4$ at 0 ppm. Solid-state NMR spectra were recorded on a Bruker DSX 300 MHz WB spectrometer operating at 7.00 T, with frequencies of 75.4 and 59.7 MHz for ^{13}C and ^{29}Si, respectively. Samples were packed under an Ar atmosphere into either 4.0 or 3.2 mm zirconia rotors (Bruker). ^{29}Si cross-polarization/magic angle spinning (CP/MAS) spectra were obtained using a 90 ° pulse length of 3.00 μs, a contact time of 5 ms, and high power proton decoupling during detection. Typically, 25,000 scans were acquired at a spinning rate of 10 kHz. Chemical shifts were referenced to *tetrakis*(trimethylsilyl)silane at -9.8 ppm. ^{13}C CP/MAS spectra were obtained using a 90 ° pulse length of 3.7 μs, a contact time of 2 ms, and high power proton decoupling during detection. Typically, 25,000 scans were acquired at a spinning rate of 10 kHz. Chemical shifts were also referenced to *tetrakis*(trimethylsilyl)silane at 3.2 ppm. ^{51}V solid-

state NMR spectra were recorded on a Bruker DSX 300 MHz WB spectrometer operating at 7.00 T with spinning rates of 12 and 14 kHz, and on a Bruker DSX 800 MHz WB spectrometer operating at 18.8 T with spinning rates of 22 and 24 kHz. Chemical shifts were referenced to $VOCl_3$ (0 ppm) and V_2O_5 (-610 ppm) on the 300 and 800 MHz spectrometers, respectively.

A continuous-wavelength electron paramagnetic resonance (EPR) measurement was performed on a Bruker EMXplus X-band spectrometer. The sample was placed in an air-free quartz tube. Experiments were performed using a microwave frequency of ca. 9.4 GHz and an attenuation of 35 dB.

IR spectra were recorded under Ar in transmission mode on a Bruker ALPHA spectrometer. For background and sample spectra, 32 scans were acquired at a resolution of 4 cm^{-1}. Self-supporting pellets of silica were made by pressing 3-5 mg sample into disks of 4 mm diameter using a hand press.

CHN analytical data were obtained from the CENTC Elemental Analysis Facility at the University of Rochester. Samples were weighed with a PerkinElmer Model AD-6 Autobalance and their compositions were determined with a PerkinElmer 2400 Series Analyzer. All samples were handled in the glovebox and transferred under argon for analysis. Vanadium content was determined using an inductively-coupled plasma atomic emission spectrometer (Thermo iCAP 6300). A vanadium standard solution (1,000 ppm V in 3 vol% HNO_3, Ricca Chemical) was diluted to the desired concentration with deionized water for use in elemental analysis. Vanadium/silica samples were first digested with HF, followed by heating to remove HF. The residue was redissolved in a solution of dilute HNO_3 prior to analysis.

Reaction products were analyzed using a Shimadzu GCMS-QP2010 fitted with an Agilent DB-1 column (100% dimethylpolysiloxane, 30 m × 0.25 mm i.d., 0.25 mm film thickness). A typical temperature program involved 2 min isothermal operation at 33 °C, followed by a 25 °C min^{-1} ramp to 220 °C. The inlet and ion source temperatures were 250 and 260 °C, respectively. Approximately 0.25 mL of the reaction mixture was sampled and centrifuged before analysis. The supernatant was injected in 1 μL aliquots into the GCMS, and conversion was determined by reference to an internal standard (1,3,5-tri-*tert*-butylbenzene).

3.2.3 Synthesis of (2-(Isopropylimino)methyl)quinolin-8-ol

2-Formyl-8-hydroxyquinoline (251 mg, 1.45 mmol) was dissolved in methanol (3 mL). Isopropyl amine (0.3 mL) was added, and the solution turned red. The reaction mixture was allowed to stand at room temperature for 5 h, then the solvent was removed under vacuum. The remaining oil was dissolved in CH_2Cl_2 (2 mL), and the solvent removed under vacuum, affording an orange oil (340 mg).

3.2.4 Synthesis of (2-(Isopropylamino)methyl)quinolin-8-ol

The saturated (amino) analog was prepared by dissolving (2-(isopropylimino)methyl)quinolin-8-ol (291 mg, 1.36 mmol) in 25 mL anhydrous ethanol to which $NaBH_4$ (1.1 equiv.) was slowly added. The orange reaction mixture was stirred at room temperature overnight. The reaction was diluted with water (100 mL) and extracted with CH_2Cl_2 (3 x 40 mL). The organic layers were combined and washed with 0.1 M

$NaHCO_3$ and dried over Na_2SO_4. The solution was filtered and the solvent was removed under vacuum to leave a yellow solid (258 mg).

3.2.5 Synthesis of Substituted Bis(8-hydroxyquinolinato)vanadium(V) Complexes

Following a modified literature procedure[3], $V(O)(O^iPr)_3$ (0.0971 g, 0.398 mmol) was added to a suspension of 2-CH_3-8-hydroxyquinoline (0.1267 g, 0.796 mmol) in CH_3CN (3 mL). The mixture was allowed to stand at room temperature for 4 d, during which time dark red crystals of $(2\text{-}CH_3\text{-}HQ)_2V(O)(O^iPr)$ **(2)** formed. The supernatant was decanted, then the crystals were washed with diethyl ether (2 x 4 mL) and dried under vacuum. ^{51}V NMR (CD_2Cl_2): -469.6 ppm.

The same general procedure was followed to prepare and isolate several substituted derivatives: $(2\text{-}NH_2\text{-}HQ)_2V(O)(O^iPr)$ (**3**), ^{51}V NMR (CD_2Cl_2): -454 ppm; $(5\text{-}NO_2\text{-}HQ)_2V(O)(O^iPr)$ (**4**), ^{51}V NMR (CD_2Cl_2): -509 ppm; $(5,7\text{-}(CH_3)_2\text{-}HQ)_2V(O)(O^iPr)$ (**5**), ^{51}V NMR (CD_2Cl_2): -480 ppm; $(2\text{-}(CH_3)_2CHN{=}CH\text{-}HQ)_2V(O)(O^iPr)$ (**6**), ^{51}V NMR (CD_2Cl_2): -480 ppm; $(2\text{-}(CH_3)_2CHN{=}CH\text{-}HQ)_2V(O)$ (**7**) IR (V=O): 983 cm^{-1}.

3.2.6 Grafting Aminopropyldimethylsilane onto Non-Porous Silica (APD-A380)

Aerosil 380 (A380, 450 mg) was partially dehydroxylated by heating to 500 °C under vacuum (0.1 mTorr) for 18 h. In a 150 mL Schlenk flask, the dried silica was suspended in 10 mL toluene, to which APDES (0.15 mL, 2 equiv.) was added. The mixture was heated to 80 °C for 2 d. The solid was isolated by filtration, washed with toluene (10 mL), followed by (2 mL methanol/10 mL CH_2Cl_2), toluene (30 mL) and lastly CH_2Cl_2 (10 mL), then dried at 100 °C under vacuum (0.1 mTorr) for 18 h. IR spectroscopy indicated near-complete reaction

with isolated hydroxyls. ^{13}C CP/MAS NMR: δ -3.20 ($Si(CH_3)_2$), 13.8 ($SiCH_2$), 15.4 (OCH_2CH_3), 27.0 ($CH_2CH_2CH_2NH_2$), 44.7 ($CH_2CH_2CH_2NH_2$), 58.5 (OCH_2CH_3). ^{29}Si CP/MAS NMR: δ 16.0 (M), -100. (Q^3), -107 (Q^4). Elemental analysis N: 0.8 wt%.

3.2.7 Tethering 8-Hydroxyquinoline to Silica (HQ-A380)

In a 100 mL Schlenk flask, 5-chloromethyl-8-hydroxyquinoline hydrochloride (5-CHQ•HCl) was dissolved in anhydrous DMSO (5 mL) followed by addition of DIPEA to give a bright yellow solution. This was added, along with CH_2Cl_2 (40 mL), to a 100 mL Schlenk flask containing APDM-A380 and the mixture was stirred at room temperature for 3 h, then at 85 °C overnight. The yellow solid was isolated by filtration, washed with CH_2Cl_2 (3 x 100 mL) and dried under vacuum. The yellow solid was then suspended in a mixture of CH_3CN and $CHCl_3$ (15 mL) and stirred overnight at room temperature, in a reactor equipped with a Teflon screw-cap, to dissolve any remaining salt. The solid was isolated by filtration, washed with CH_3CN (100 mL) and $CHCl_3$ (100 mL), and dried under vacuum at 115 °C for 18 h. ^{13}C CP/MAS NMR: δ -2.40 ($Si(CH_3)_2$), 15.4 (OCH_2CH_3), 15.5 ($SiCH_2$), 20.6 ($CH_2CH_2CH_2NHCH_2$(HQ)), 42.8, 51.0 ($CH_2CH_2CH_2NHCH_2$(HQ)), 58.5 (OCH_2CH_3), 120-152 ($CH_2CH_2CH_2NHCH_2$(*HQ*)). Elemental analysis N: 1.6 wt%.

3.2.8 Complexing Vanadium to HQ-A380 ($V(O)(HQ)_2(O^iPr)$-A380)

In a Teflon screw-cap reactor, HQ-A380 was suspended in CH_2Cl_2. A solution of $V(O)O^iPr_3$ (1:1 mol ratio relative to HQ) in CH_2Cl_2 was added to the suspension. Upon contact with $V(O)O^iPr_3$, the yellow solid turned a burgundy color. Magnetic stirring was

continued for 4 h to ensure thorough mixing. The burgundy solid was isolated by filtration, washed with CH_2Cl_2 (3 x 100 mL), and dried under vacuum at room temperature for 18 h.

A second aliquot of the ligand (8-HQ) was added to the vanadium-modified silica to ensure that all vanadium centers were coordinated by a second hydroxyquinolinato ligand. The silica (880 mg) was suspended in CH_3CN to which 8-HQ (78 mg) (1:1 mol ratio) dissolved in CH_3CN was added. The suspension was stirred at room temperature for 4 h. The dark burgundy solid was isolated by filtration, washed with CH_3CN (3 x 75 mL) and dried under vacuum (0.1 mTorr) at 90 °C. ^{51}V MAS NMR: δ -494 (78.9 MHz), -507 (210 MHz). Vanadium analysis: 0.78 wt%. Elemental analysis N: 1.7 wt%.

3.2.9 General Procedure for Catalytic Oxidation of Benzyl alcohols with (V(O)(HQ)$_2$(O^iPr)-A380)

In a 25 mL vial, the benzyl alcohol substrate (0.238 mmol) and 1,3,5-tri-*tert*-butylbenzene (internal standard) were dissolved in 1,2-dichloroethane (5 mL). The solution was added to a 100 mL round-bottom flask containing V(O)(HQ)$_2$(O^iPr)-A380 (25 mg, 0.00476 mmol) and equipped with a magnetic stir bar and septum. An amine base, either NEt_3 or $HNEt_2$ (0.0238 mmol), was added and the flask was attached to an air-cooled condenser. The flask was heated with stirring in an oil bath at 70 °C for 24 h under air. The conversion was determined by GC-MS using an internal standard. For the leaching test, the reaction mixture was centrifuged after 4 d, and the solution was separated from the catalyst. The supernatant was heated under reaction conditions for an additional 24 h before sampling the solution.

When *tert*-butyl hydroperoxide was used as the oxidant, reagents were added to the

flask under a flow of N_2. The flask was sealed with a septum under N_2. When the oxidant was N_2O, all reagents were added to the flask under a flow of N_2O. The flask was sealed with a septum under N_2O headspace for the duration of the experiment.

3.2.10 General Procedure for Catalytic Oxidation of Benzyl amine with (V(O)(HQ)$_2$(O^iPr)-A380)

In a 25 mL vial, the benzyl amine substrate (0.0726 mmol) and 1,3,5-tri-*tert*-butylbenzene (internal standard) were dissolved in CH_3CN (2 mL). The solution was added to a 15 mL Teflon screw cap reactor containing V(O)(HQ)$_2$(O^iPr)-A380 (24 mg, 0.00363 mmol) and equipped with a magnetic stir bar. The reactor was sealed and heated with stirring in an oil bath at 60 °C for 21 h under air. The conversion was determined by GC-MS using an internal standard.

3.3 Results and Discussion

3.3.1 Evaluation of ligand substituent effects

Ligand substituents are frequently used in catalyst tethering, but substituent effects can play a major role in catalytic activity.[3] We prepared 8-hydroxyquinolinato complexes of vanadium(V) with either 2-(isopropylimino)methyl or 2-(isopropylamino)methyl substituents, in order to ensure that the presence of a tethering group on the 8-HQ ring would not interfere with formation of the *bis*(chelate) complex. The modified ligands are easily accessible through the reaction of commercially available 2-carboxyaldehyde-8-hydroxyquinoline with isopropylamine. Upon addition of V(O)(O^iPr)$_3$ to 2 equiv.? (2-(isopropylimino)methylquinolin-8-ol, we formed the expected red-brown *bis*((2-

(isopropylimino)methyl)(8-hydroxyquinolinato)vanadium(V) complex, Scheme 3.1. Its crystal structure, shown in Fig. 3.2, retains a symmetry similar to that of unsubstituted $V(O)(HQ)_2(O^iPr)$.[4]

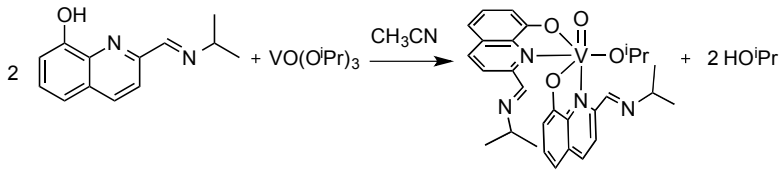

Scheme 3.1. Synthesis of *bis*((2-(isopropylimino)methyl)(8-hydroxyquinolinato))(2-propanato) oxovanadium(V) (**6**).

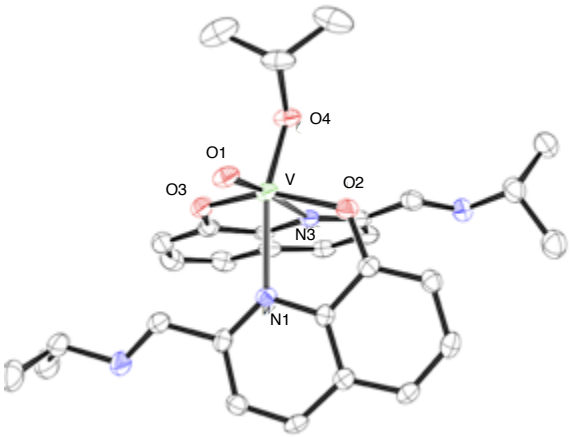

Figure 3.2. Crystal structure of **6** (H atoms omitted for clarity). Selected bond lengths (Å): V-O1 = 1.595(2); V-O3 = 1.871(2), V-O4 = 1.772(2), V-N1 = 2.301(2), V-N3 = 2.439(2), N2-C10 1.266(3), N2-C11 = 1.462(4), N4-C10 1.265(3), N4-C11 = 1.471(4). Selected bond angles (°): O1-V-O4 = 100.70(9), O1-V-O3 = 96.81(9), O4-V-O3 = 101.69(9).

To our surprise, addition of $V(O)(O^iPr)_3$ to 2 equiv. (2-(isopropylamino)methyl)quinolin-8-ol led to brown crystals of a V(IV) product, Scheme 3.2. Its short C-N bond distances (1.277 Å) are characteristic of imines, Fig. 3.3, compared to the longer bond distance (1.47 Å) for amines. No oxidation products, e.g., acetone from the 2-propanato ligand, were observed by ^1H NMR of the reaction mixture. We did observe a yellow side-product; however, efforts to isolate and identify it were unsuccessful. Vanadium catalyzed oxidation of imines is not uncommon.[5, 6] Wang et. al recently reported the direct synthesis of imines from amines catalyzed by $V(O)(HQ)_2(O^iPr)$ under mild conditions with air as the oxidant in the absence of additives or promoters.[6] Although our reaction occurred in the absence of air, which was presumably used to reoxidize vanadium, we believe a similar pathway is occurring in the oxidation of the amine tether.

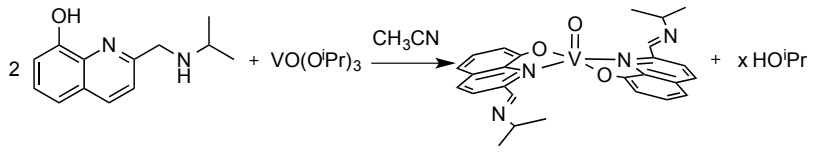

Scheme 3.2. Unexpected oxidation of (2-(isopropylamino)methyl)quinolin-8-ol, during the reaction to form *bis*((2-(isopropylimino)methyl)-8-hydroxquinolinato) oxovanadium(IV) (**7**).

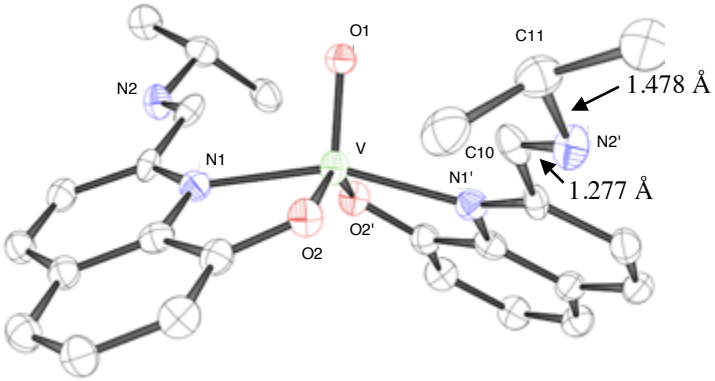

Figure 3.3. Crystal structure of **7** (H atoms omitted for clarity). Selected bond lengths (Å): V-O1 = 1.600(4); V-O2 = 1.949(3), V-O2´ = 1.949(3), V-N1 = 2.102(3), V-N1´ = 2.102(3), N2-C10 = 1.277(5), N2-C11 = 1.478(5). Selected bond angles (°): O1-V-O2 = 107.69(10), O1-V-O2´ = 107.69(9), O2-V-O2´ = 144.62(19).

The activities of **6** and **7** were investigated in the catalytic oxidation of 4-methoxy-benzyl alcohol. Both were much less active (14 and 7 % conversion after 24 h at 85 °C in toluene) compared to $V(O)(HQ)_2(O^iPr)$ (49 % conversion after just 4 h at 60 °C in 1,2-dichloroethane, and 100 % conversion after 24 h). The lower conversions may be due to increased steric hindrance at vanadium resulting from the increased chain length of the 2-substituent, which could interfere with substrate binding.

In order to identify the best location for the tether, a variety of substituted *bis*(8-hydroxyquinolinato)vanadium(V) complexes were prepared, and substituent effects on the rate of oxidation of 4-methoxy-benzyl alcohol were assessed. Positions on the 8-hydroxyquinoline ring are labeled in Fig. 3.4. The unsubstituted *bis*(8-quinolinato)vanadium complex gave 49 % conversion to 4-methoxy-benzaldehyde in 4 h, and 100 % conversion in

24 h, Fig. 3.5.[3] In contrast, ligands with substituents located at the 2-position of the ring systems, such as in **2** and **3**, resulted in almost no conversion after 24 h in 1,2-DCE at 60 °C (2 and 4 %, respectively). Catalysts with 5- or 7-substituted 8-hydroxyquinolinato ligands exhibited considerably higher catalytic activity, and electron-withdrawing substituents (e.g., NO_2) give more activity than electron-donating substituents (e.g., CH_3). For example, **4** showed 62 % conversion after 24 h, while complex **5** gave 100 % conversion under the same reaction conditions.

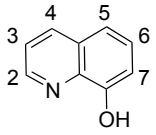

Figure 3.4. Numbering of atoms on the 8-hydroxyquinoline ring.

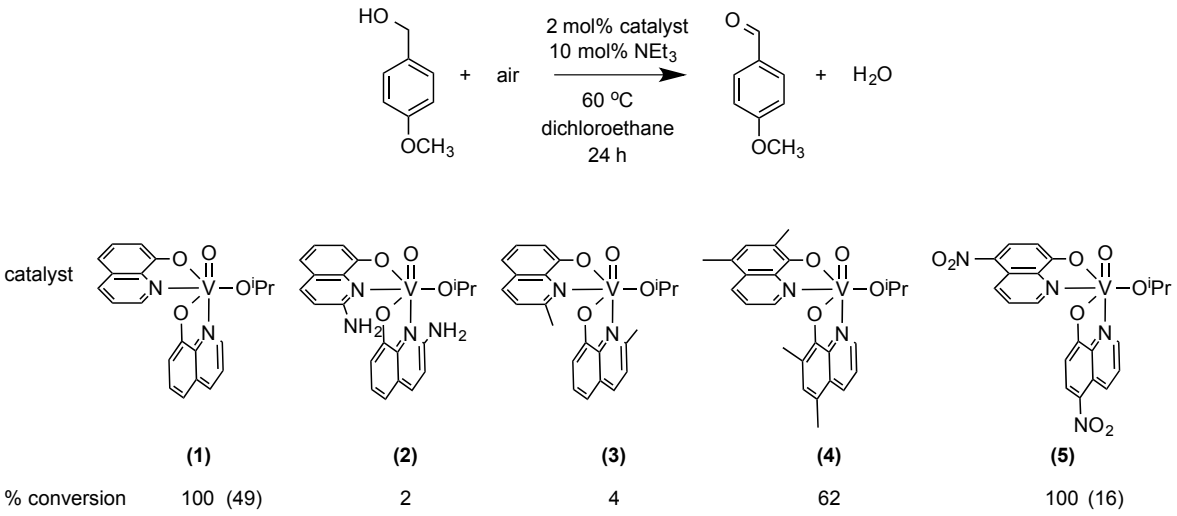

Figure 3.5. Catalytic oxidation of 4-methoxybenzyl alcohol using a variety of substituted *bis*(8-hydroxyquinolinato)vanadium(V) complexes. All reactions are 100 % selective for the aldehyde. Values in parentheses are % conversion after 4 h.

We previously reported DFT calculated the transition state in the redox ewXRION OD $V(O)(HQ)_2(OCH_2C_6H_5)$.[1] Visualizing the spatial orientation of the HQ ligands, we were able to better understand ligand substituent effects, focusing primarily on the substitution position and steric interactions between the ligand, the metal center and the coordinated alcohol substrate. The substituent positions on the quinoline ring which allow for the least steric congestion for substrate coordination to vanadium are the 4-, 5- or 7-positions. Substituents in the 2-position hinder binding of alcohol to vanadium. This is consistent with the low catalytic activity observed for **2** and **3**, Fig. 3.5.

3.3.2 Tethering of an (8-hydroxyquinolinato)vanadium complex to silica

Previous reports on the immobilization of 8-hydroxyquinoline on silica involved metal complexation aimed at trace-metal extraction.[7-9] In most cases, the methods involved lengthy syntheses and provided minimal characterization of the material. In this work, we chose a simple two-step grafting approach involving initial covalent attachment of aminopropylsilane to silica, and subsequent tethering of a 5-chloromethyl-8-hydroxyquinoline derivative (5-CHQ•HCl). This straightforward approach provides an immobilized ligand to which V(V) can coordinate. Since the hydroxyl group of 8-HQ is strongly *ortho*/*para*-directing, substituents are most readily introduced at either the 5- or 7-positions.[10] Guided by results from the homogeneous catalysts (Fig. 3.5), DFT calculations of the transition state and synthetic considerations, we chose to install a tether at the 5-position, in order to avoid steric hindrance that could suppress catalytic activity.

Aminopropyldimethylsilyl groups were covalently attached to a partially

dehydroxylated silica surface through a condensation reaction between the ethoxy group of aminopropyldimethylethoxysilane (APDES) and the silica silanols, to give APD-A380, Scheme 3.3. IR spectroscopy confirmed the disappearance of the majority of the isolated silanol peak at 3747 cm^{-1} upon grafting, Fig. 3.6. A weak, broad peak centered at 3600 cm^{-1} remains in the υ(O–H) region, representing hydroxyl groups which are perturbed by hydrogen bonding and/or inaccessible to the organosilane. The υ(N–H) region shows the two expected bands at 3418 and 3377 cm^{-1} for the newly installed primary amine, Fig. 3.6. Additional weak bands for N-H and C-H bending modes appear between 1700 - 1275 cm^{-1}.[11-13] Elemental analysis also confirms amine tethering, with 0.8 % N-content, corresponding to 0.6 mmol grafted silane per g silica.

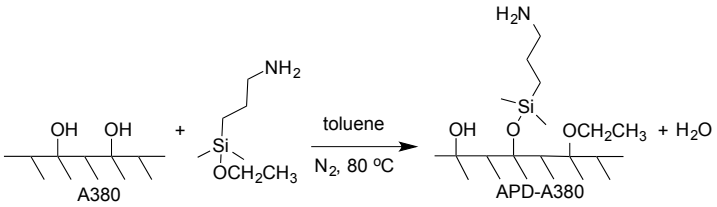

Scheme 3.3. Grafting aminopropyldimethylethoxysilane on A380 silica pretreated at 500 °C, to give APD-380.

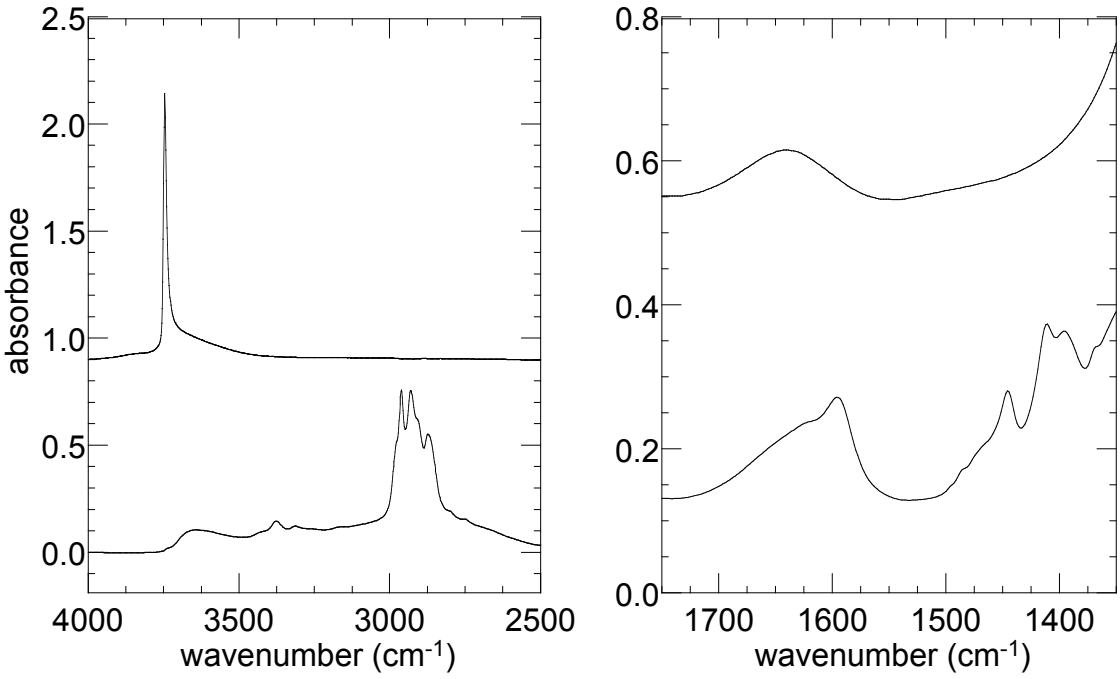

Figure 3.6. Transmission IR spectra of A380 silica pretreated at 500 °C, before (top), and after aminopropyldimethylsilyl modification (bottom) to give APD-A380.

^{13}C CP/MAS NMR spectroscopy of APD-A380 revealed the presence of the anchored aminopropyldimethylsilyl group as well as ethoxy groups derived from the ethanol generated during the grafting reaction, Fig. 3.7a. A signal at -3 ppm is attributed to the methyl groups $=SiOSi(CH_3)_2$ of the grafted silane, while peaks corresponding to the propyl chain are located at 14, 27, and 44 ppm. The ^{29}Si CP/MAS spectrum shows a monofunctional Si signal (M, R_3SiO) at 13 ppm for the grafted silane, Fig. 3.7b. The peaks at -100 and -107 ppm represent silicon atoms corresponding to Q^3 (monohydroxy- or alkoxy-substituted Si) and Q^4 (tetrasiloxy-substituted Si) sites, respectively. Both ^{13}C and ^{29}Si NMR spectra are in good agreement with other reports of post-synthesis functionalization of silica involving APDES.[11, 13, 14]

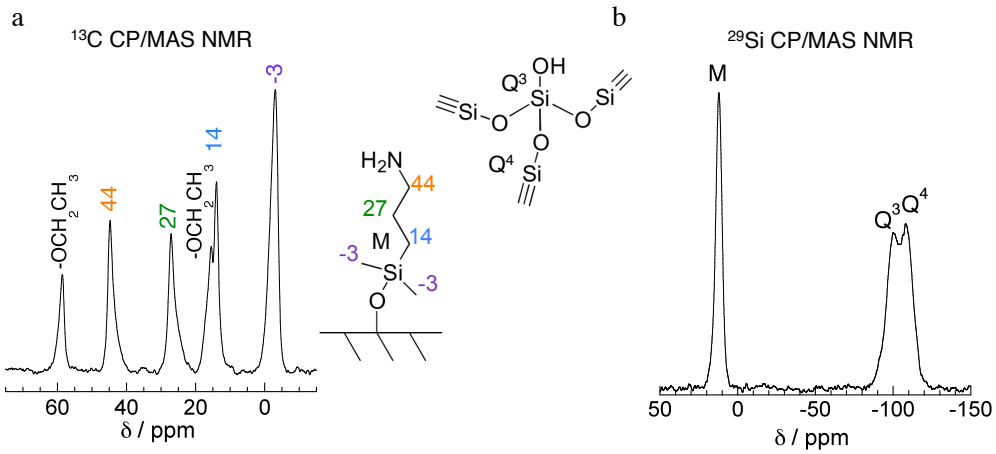

Figure 3.7. Solid-state NMR spectra of APD-A380: (a) ^{13}C CP/MAS, and (b) ^{29}Si CP/MAS NMR. Spinning rate ? kHz.

The next step was reaction of APD-A380 with 5-chloromethyl-8-hydroxyquinoline hydrochloride (5-CHQ•HCl). N-alkylation generates the silica-supported ligand HQ-A380, Scheme 3.4. As expected, elemental analysis confirmed that the N-content of the materials doubled, from 0.8 to 1.6 %, following incorporation of the hydroxyquinoline moiety.

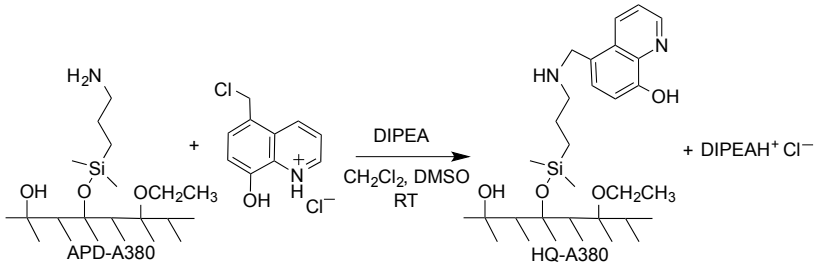

Scheme 3.4. Tethering 8-hydroxyquinoline to APD-A380 to give HQ-A380.

Upon HQ incorporation, a broad peak centered at 3400 cm^{-1} appears, ascribed to the υ(O–H) stretching vibration of HQ.[15-17] This region may also contain an υ(N–H) contribution from the secondary amine on the tether, but it is difficult to discern due to the broadness of the peak. Several new, poorly resolved bands appear in the υ(C–H) region between 2700 and 3100 cm^{-1}, Fig. 3.8. Strong bands at 1613, 1582, 1506, and 1477 cm^{-1} are associated with the hydroxyquinolinate aromatic ring system.[15-17] The bands at 1409 and 1377 cm^{-1} are probably C-H bends.[15]

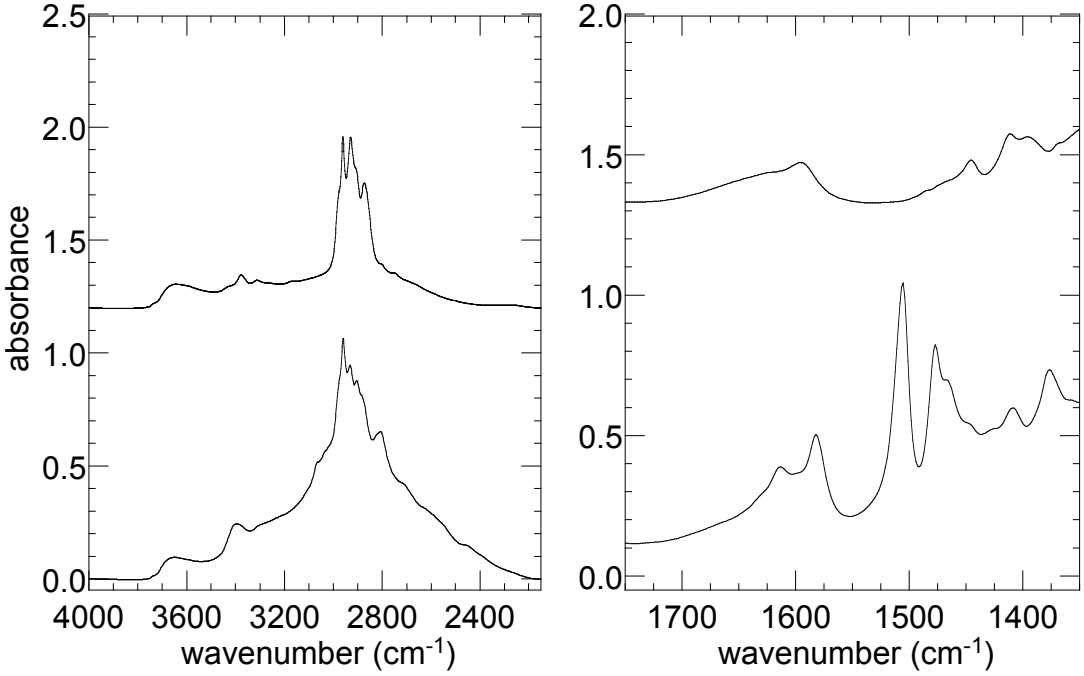

Figure 3.8. Transmission IR spectra of APD-A380 (top), and after N-alkylation with 5-CHQ•HCl to give HQ-A380 (bottom).

The ^{13}C CP/MAS NMR spectrum of HQ-A380 clearly shows the presence of aromatic carbons associated with the quinoline ring in the range 100-160 ppm (Fig. 3.9a).

The overall pattern of the aromatic region is in good agreement with the corresponding solution-state spectrum of the molecular complex.[3] Ethoxy groups persist after reaction and workup. In the ^{29}Si CP/MAS NMR, the M signal at 13 ppm is still present, verifying that the grafted silane remains intact (Fig. 3.9b).

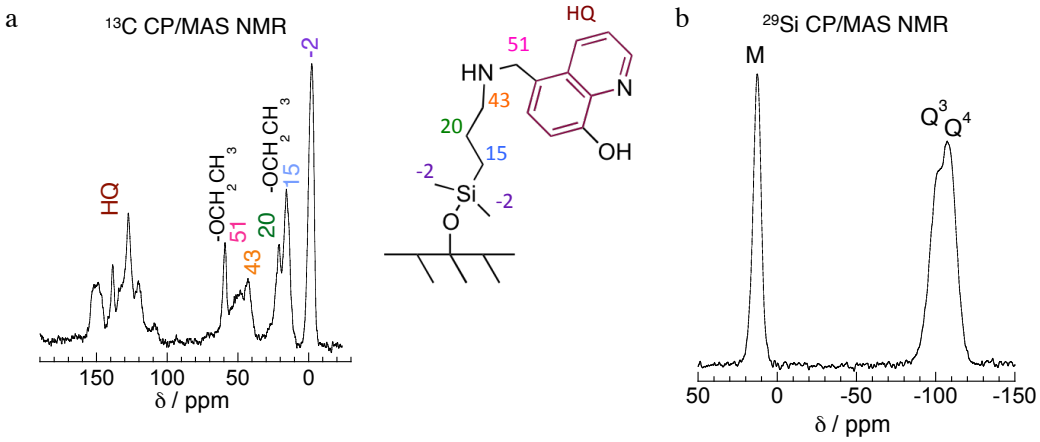

Figure 3.9. Solid-state NMR spectra of HQ-A380: (a) ^{13}C CP/MAS NMR, and (b) ^{29}Si CP/MAS NMR.

After confirming the covalent attachment of hydroxyquinoline, vanadium was incorporated using V(O)(O^{i}Pr)$_3$, Scheme 3.5. Elemental analysis gave a vanadium loading of 0.78 wt%. Subsequent addition of one equiv. free 8-hydroxyquinoline was intended to form the silica-supported *bis*(8-hydroxyquinolinato)vanadium V(O)(HQ)$_2$(O^{i}Pr)-A380, Scheme 3.5a. However, since the increase in the N-content following addition of free 8-HQ, from 1.6 to 1.7 wt%, is within the error of the instrument, we suspect that most sites were already *bis*(chelated) by two tethered ligands in close proximity to one another, Scheme 3.5b. Furthermore, the total uptake of V (0.17 mmol/g) is less than half the amount of tethered HQ

(0.68 mmol/g silica). Still, the small change in the N-content ensures that any initially mono-chelated species are complexed with the second equivalent of 8-hydroquinoline.

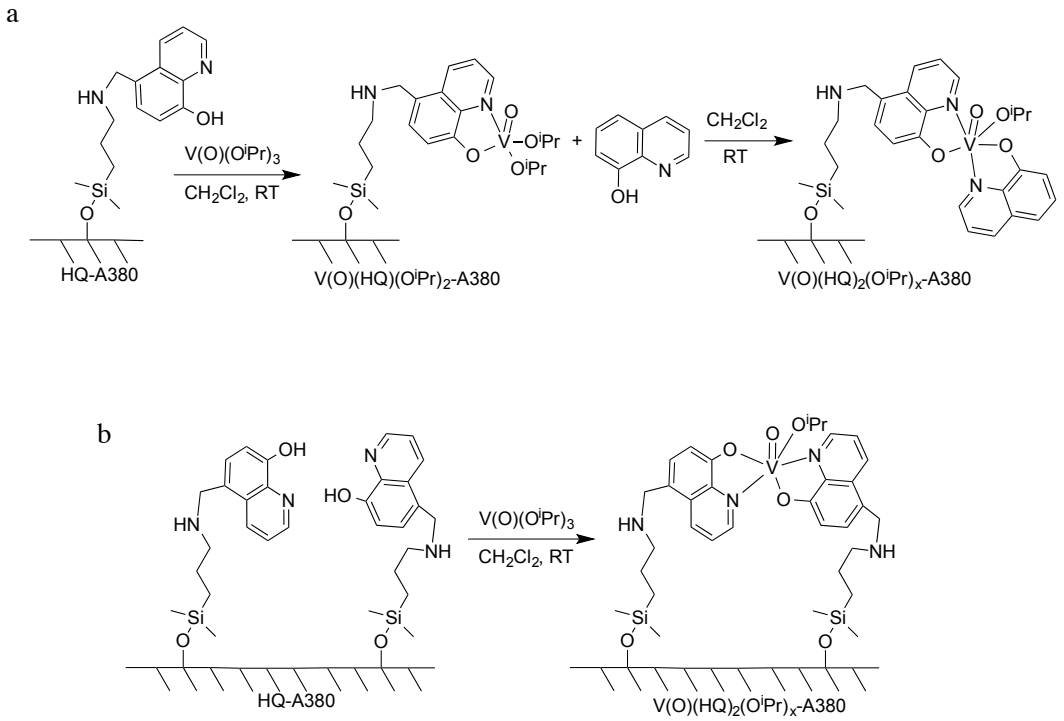

Scheme 3.5. (a) Mono-chelation of vanadium by HQ-A380, and reaction with a second equivalent of 8-hydroxyquinoline to form a bis(chelated) complex, $V(O)(HQ)_2(O^iPr)_x$-A380; (b) bis-chelation of vanadium by two 8-HQ tethers within close enough proximity to form $V(O)(HQ)_2(O^iPr)$-A380, without the need for additional 8-HQ.

The complexation and chelation reactions were followed by IR spectroscopy. Only subtle differences between HQ-A380 and $V(O)(HQ)_2(O^iPr)_x$-A380 are observed in the υ(C–H) region between 3100 and 2800 cm^{-1}, Fig. 3.10. Two new peaks at 2974 and 1322 cm^{-1} are assigned to the 2-propoxide ligand.[18] In addition, the intensity of the broad peak at 3400 cm^{-1}, assigned to the υ(O–H) mode of uncoordinated 8-HQ, decreases upon addition of vanadium.

The characteristic ring vibrations of 8-HQ-A380 at 1582 cm^{-1} shifts to a lower frequency (1577 cm^{-1}) upon chelation, consistent with previous chelation studies.[5] Interestingly, an unexpected peak at 1598 cm^{-1} appears upon addition of $V(O)(O^iPr)_3$, and persists following addition of the second equiv. of 8-HQ. Its assignment will be discussed further below. The persistence of the band at 1322 cm^{-1} implies that one 2-propoxide ligand remains coordinated.

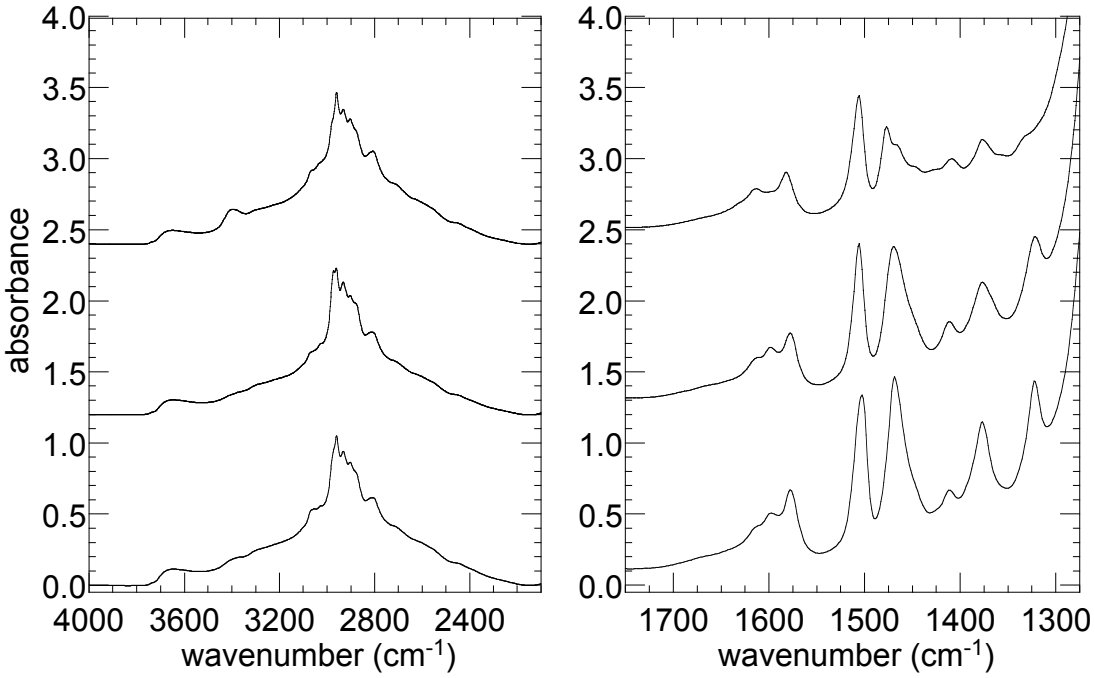

Figure 3.10. Transmission IR spectra of HQ-A380 (top), after reaction with $V(O)(O^iPr)_3$ (middle), and after adding one equiv. free 8-HQ (bottom) to give $V(O)(HQ)_2(O^iPr)_x$-A380.

The ^{13}C CP/MAS NMR spectrum of $V(O)(HQ)_2(O^iPr)_x$-A380 remains largely unchanged relative to HQ-A380, however, there is a slight increase in the relative intensity of

the peak centered at 20 ppm, due to the contribution from -CH_3 groups on the 2-propoxide ligand, Fig. 3.11a. The methine signal appears at 90 ppm, Fig. 3.11a, consistent with the molecular complex (91 ppm). However, there is a new and unexpected peak at 164 ppm, Fig. 3.12, which is not present in the spectrum of HQ-A380. This chemical shift is characteristic of an imine carbon. The ^{29}Si CP/MAS spectrum, Fig. 3.11b, confirms that vanadium addition did not disrupt the silica structure. We reported above that addition of $VO(O^iPr)_3$ to (2-(isopropylamino)methyl)quinolin-8-ol resulted in ligand oxidation to give *bis*(2-(isopropylimino)methylquinolinato)vanadium(IV). The new band in the IR spectrum (1598 cm^{-1}, consistent with a C=N stretching vibration) and the peak at 164 ppm in the ^{13}C NMR spectrum support the formation of an imine upon reaction of HQ-A380 with $VO(O^iPr)_3$.

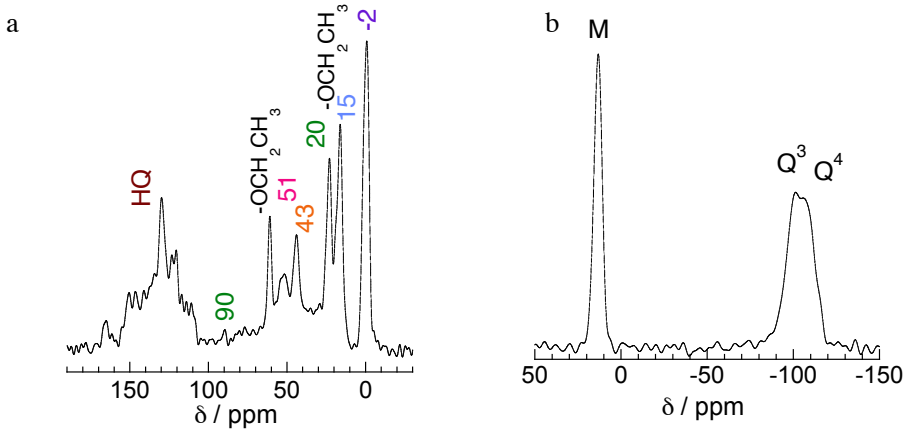

Figure 3.11. Solid-state NMR spectra for $V(O)(HQ)_2(O^iPr)_x$-A380: (a) ^{13}C CP/MAS NMR, and (b) ^{29}Si CP/MAS NMR.

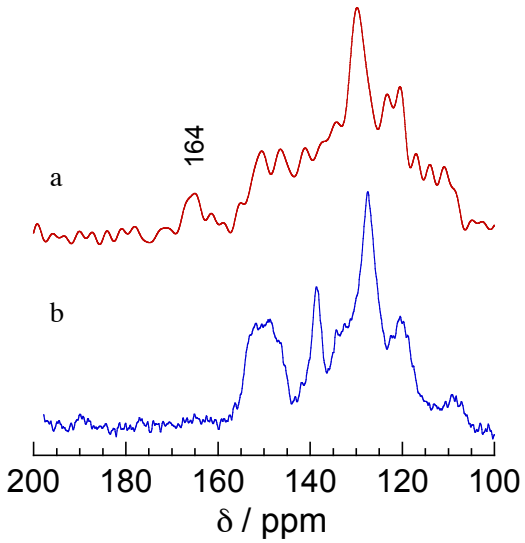

Figure 3.12. Stacked view of solid-state ^{13}C CP/MAS NMR spectra for (a) $V(O)(HQ)_2(O^iPr)_x$-A380, and (b) HQ-A380.

Formation of an imine suggests that V(V) oxidizes the secondary amine of the tether, resulting in reduction to V(IV). In order to determine whether a reduced vanadium species is also present, analogous to the homogeneous complex **7**, an X-band EPR spectrum of the material was collected. It shows the characteristic eight-line hyperfine structure for V(IV), Fig. 3.13. The presence of V(IV) is consistent with oxidation of the amine tether, although $V(O)(HQ)_2$-A380 cannot be a stoichiometric product. For simplicity, we will continue to describe it as $V(O)(HQ)_2(O^iPr)_x$-A380.

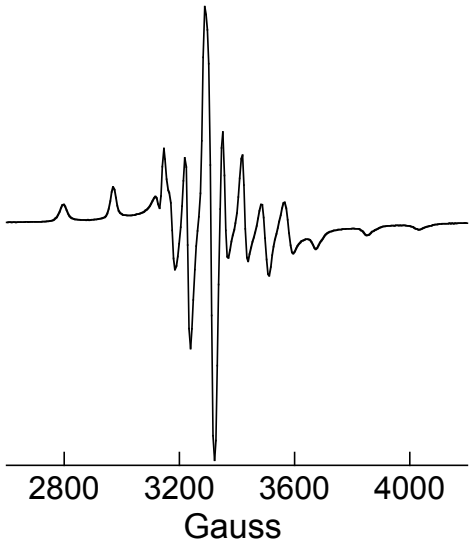

Figure 3.13. X-band EPR spectrum of $V(O)(HQ)_2(O^iPr)_x$-A380, recorded at 25 °C.

Nevertheless, the presence of some diamagnetic V(V) was verified by solid-state ^{51}V MAS NMR. Spectra were acquired on two different spectrometers with two different spin rates in order to identify the isotropic peak, Fig. 3.14. Using a higher magnetic field gives better sensitivity for quadrupolar nuclei such as vanadium ($I = 7/2$) by reducing the intensity of the spinning side-bands. The isotropic ^{51}V chemical shift for the silica-supported complex is -494 ppm (at 78.9 MHz, 10 kHz spinning rate) and -507 ppm (at 210 MHz, 24 kHz spinning rate). This agrees well with the value for the unsubstituted molecular V(V) complex (-492 ppm).[3]

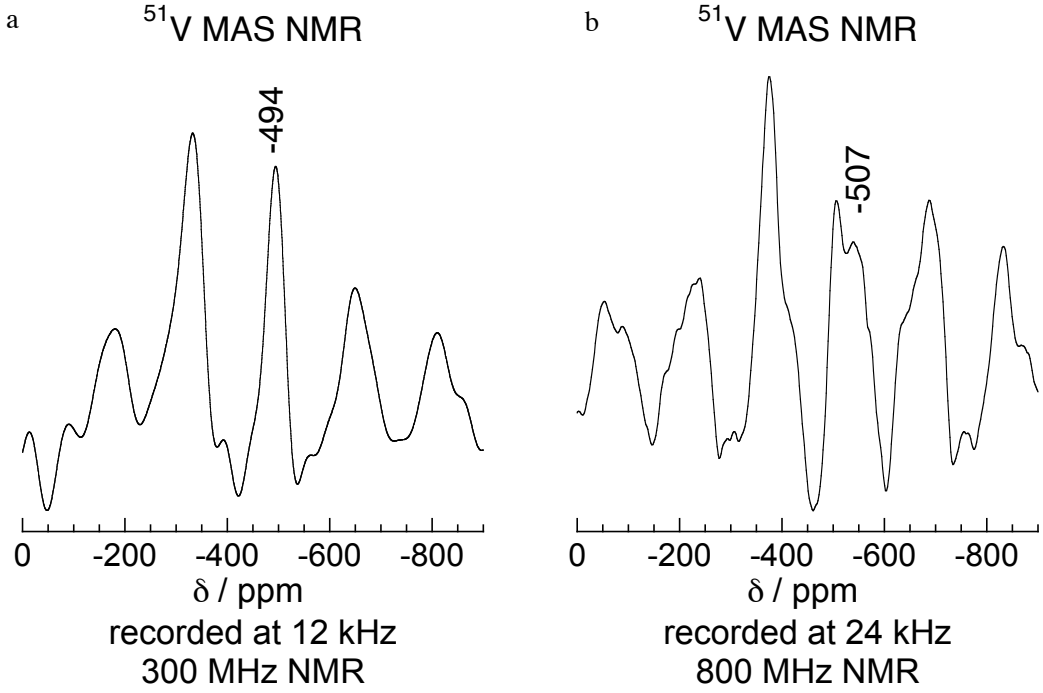

Figure 3.14. Solid-state ^{51}V CP/MAS NMR of V(O)(HQ)$_2$(O^{i}Pr)$_x$-A380, recorded at (a) 78.9 MHz (spinning rate 12 kHz), and (b) 210 MHz (spinning rate 24 kHz).

3.3.3 Catalytic activity for benzyl alcohol oxidation.

Although multiple vanadium oxidation states are present in V(O)(HQ)$_2$(O^{i}Pr)$_x$-A380, previous studies showed that molecular *bis*-quinolinato complexes of both V(V) and V(IV) are both effective catalysts for aerobic benzyl alcohol oxidation, affording complete conversion after 24 h at 60 °C in 1,2-dichloroethane (1,2-DCE).[3] V(O)(HQ)$_2$(O^{i}Pr)-A380 was tested in this reaction, Scheme 3.6, using conditions analogous to those reported for the homogeneous catalyst in Chapter 2.

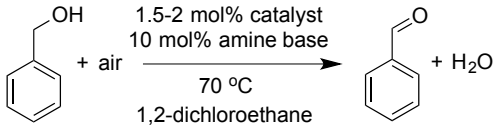

Scheme 3.6. Aerobic oxidation of benzyl alcohol catalyzed by $V(O)(HQ)_2(O^iPr)$-A380.

Oxidation of benzyl alcohol proceeds selectively to the aldehyde in the presence of $V(O)(HQ)_2(O^iPr)_x$-A380 (1.5-2.0 mol%) and NEt_3 (10 mol%). However, after 24 h at 70 °C in 1,2-DCE, only 3 % conversion was achieved, compared to 100 % for the homogeneous catalyst under the same conditions. When the reaction progress was monitored for 140 h, the conversion increased to 70 %, confirming that the catalyst remains active, although slow. The solid catalyst was removed by hot filtration and the supernatant was exposed to reaction conditions for a further 24 h, but no further oxidation of benzyl alcohol occurred, nor was benzaldehyde oxidized to benzoic acid. ICP-MS analysis of the supernatant showed some vanadium leaching from the silica support (~ 8-10 %) under reaction conditions (70 °C in DCE). Hydrolysis (H_2O is a by-product) of the imine tether in the polar solvent may be responsible for the presence of vanadium in the supernatant. The absence of over-oxidized products suggests that the soluble vanadium species do not catalyze further oxidation reactions as was observed with the homogeneous catalyst. Any expected conversion of benzyl alcohol by leached vanadium species may not be visible due to their low concentration in solution.

3.3.4. Effect of the amine promoter.

Replacing triethylamine by the more basic diethylamine[19, 20] enhances the rate of benzyl alcohol oxidation, Fig. 3.15 and Table 3.1. After 24 h, 23 % benzyl alcohol was

oxidized to the aldehyde in the presence of $HNEt_2$, compared to 3 % for NEt_3 (after 72 h, yields were 28 vs. 42 %, respectively). This result is similar to that for molecular $V(O)(HQ)_2(O^iPr)$, for which the rate increased by an order of magnitude upon replacing NEt_3 by $HNEt_2$.[1] According to the homogeneous mechanism, the base deprotonates the substrate by removing a benzylic proton. It is likely that a similar mechanism applies to the supported catalyst. Increasing the amount of $HNEt_2$ to 50 mol% resulted in no change in the overall conversion after 24 h, Fig. 3.16. However, after an additional 24 h, the yield of benzaldehyde was slightly higher (48 vs 35 %, for 50 and 10 mol % $HNEt_2$, respectively).

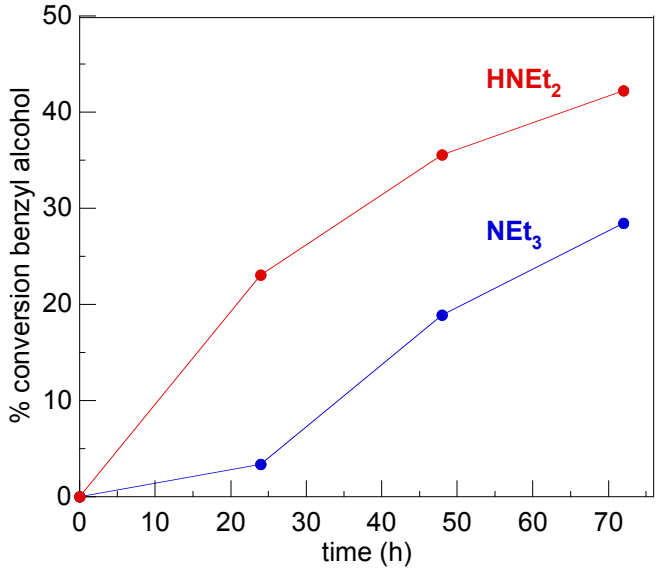

Figure 3.15. Effect of amine basicity (10 mol%) on aerobic oxidation of benzyl alcohol catalyzed by $V(O)(HQ)_2(O^iPr)$-A380 at 70 °C in 1,2-DCE.

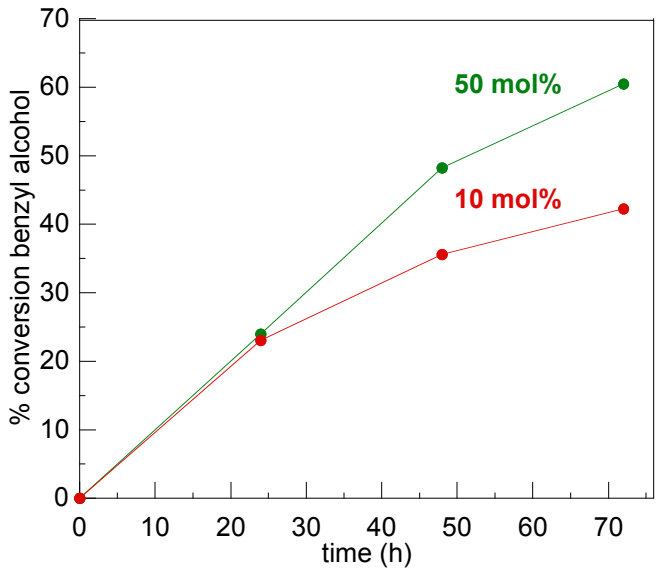

Figure 3.16. Effect of $HNEt_2$ concentration on the rate of aerobic oxidation of benzyl alcohol catalyzed by $V(O)(HQ)_2(O^iPr)$-A380 at 70 °C in 1,2-DCE.

Table 3.1. Aerobic oxidation of benzylic alcohols catalyzed by $V(O)(HQ)_2(O^iPr)$-A380[a]

Entry	Substrate	Base	Solvent[b]	Temperature (°C)	Conversion (%)[c]
1	benzyl alcohol	NEt_3	1,2-DCE	70	3
2	benzyl alcohol	$HNEt_2$	1,2-DCE	70	23
3	4-hydroxybenzonitrile	$HNEt_2$	1,2-DCE	70	42
4	4-methoxybenzyl alcohol	$HNEt_2$	1,2-DCE	70	3
5[d]	benzyl alcohol	$HNEt_2$	1,2-DCE	70	23
6	benzyl alcohol	$HNEt_2$	toluene	100	32
7	benzyl alcohol	$HNEt_2$	o-xylene	130	69[d]

[a] Reaction conditions: alcohol substrate (0.20 mmol), 1.5-2.0 mol% catalyst, 10 mol% NEt_3 or $HNEt_2$.

[b] Approximately 5 mL.

[c] Conversions are reported after 24 h reaction time.

[d] With 50 mol% $HNEt_2$.

3.3.5 Para-substituent effect.

To study the influence of substrate electronic effects on the rate, we performed a Hammett study using *para*-substituted benzyl alcohols. After 24 h, conversion of the electron-poor 4-(hydroxymethyl)benzonitrile to the aldehyde was nearly double (42 %) relative to benzyl alcohol, Fig. 3.17 and Table 3.1. In contrast, electron-rich 4-methoxy-

benzyl alcohol showed minimal conversion (3 %) after the same reaction time. These results follow the same trend as the homogeneous bis(8-hydroxyquinolinato)vanadium complex, in which a greater rate acceleration occurred for electron-poor benzyl alcohols. Since benzyl alcohols with electron-withdrawing substituents have more acidic benzylic protons, they are easier to deprotonate.

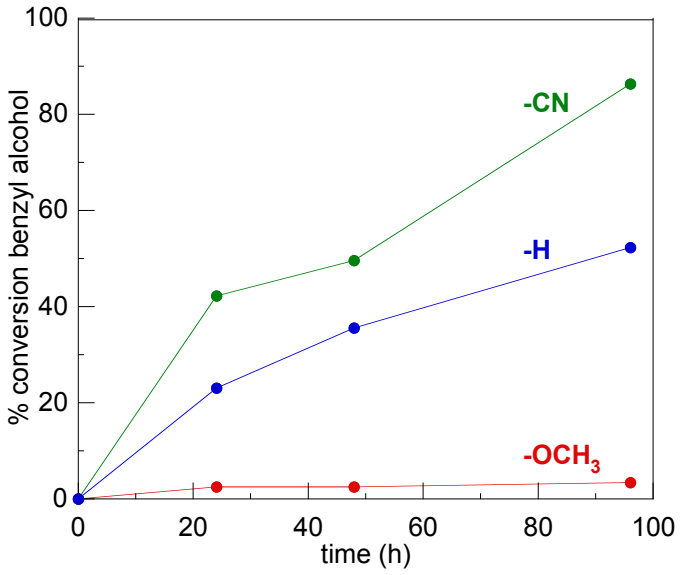

Figure 3.17. Substituent effects on aerobic oxidation of *para*-substituted benzyl alcohols, $HOCH_2C_6H_4$-*p*-X (X = OCH_3, H, and CN), catalyzed by $V(O)(HQ)_2(O^iPr)_x$-A380 using 10 mol% $HNEt_2$, at 70 °C in 1,2-DCE.

3.3.6 Effect of solvent/temperature.

The effect of the solvent and the reaction temperature on the reaction rate was also investigated, Fig. 3.18. It has been proposed that 1,2-DCE undergoes bimolecular substitution and elimination reactions with diethylamine.[21] It is possible that on the long time

scale of the heterogeneous reaction some side reaction between the solvent and secondary amine could occur. Changing the solvent from 1,2-DCE to toluene not only allowed us to increase the temperature from 70 to 100 °C but could circumvent side reactions with diethylamine. The conversion after 24 h improved slightly (from 23 to 32 %). After 96 h, the conversion reached 88 %, while maintaining selectivity for benzaldehyde. The catalyst also appeared to be more stable in toluene than in 1,2-DCE with only 1 % leaching compared to 8-10 %. Using a more hydrophobic solvent could suppress hydrolysis of the imine tether, which would result in free vanadium species. Changing the solvent to o-xylene and heating at 130 °C led to a more dramatic increase in conversion after 24 h, to 69 %. Nearly 100 % conversion was observed after 72 h reaction time. Therefore, using a high boiling point solvent, which allows heating at elevated temperatures, causes the rate of benzyl alcohol oxidation to increase.

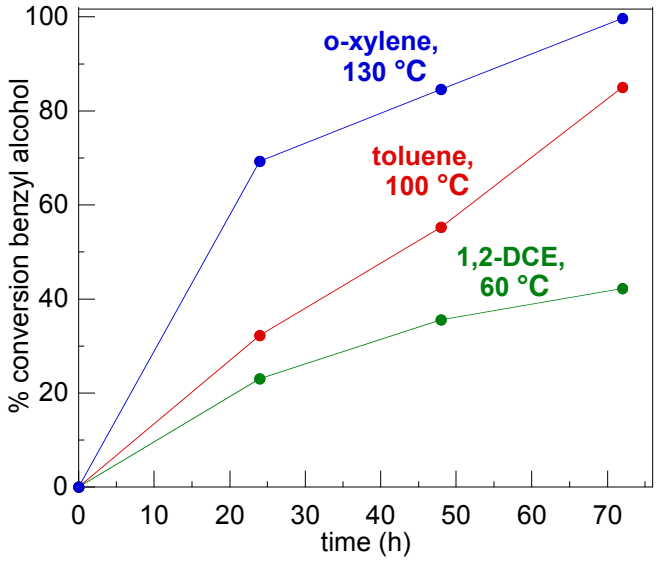

Figure 3.18. Effect of solvent and temperature on the aerobic oxidation of benzyl alcohol,

catalyzed by $V(O)(HQ)_2(O^iPr)$-A380 and $HNEt_2$.

3.3.7 Effect of oxidant.

When the oxidant was changed to *tert*-butyl hydroperoxide, and the reaction was conducted under N_2 the conversion of benzyl alcohol to benzaldehyde after 24 h was 22 %, similar to results obtained using air. However, following the reaction for an additional 24 h led to no increase in conversion, in contrast to the behavior in air. When N_2O (1 atm) was used as the oxidant in a sealed flask, only 3.8 % benzyl alcohol was converted to benzaldehyde after 24 h.

3.3.8 Catalyst recycling.

The catalyst was recovered from the reaction mixture (benzyl alcohol, $HNEt_2$ in 1,2-DCE) by filtration, washed with acetone and dried overnight at 120 °C. It was then reused in the oxidation of benzyl alcohol under the same reaction conditions as the initial oxidation reaction, using 10 mol% $HNEt_2$ at 70 °C in 1,2-DCE. After 24 h, the activity was much lower than the fresh catalyst providing only 2% conversion of benzyl alcohol. Following the reaction for 96 h led to no increase in conversion (3 %). Catalyst deactivation may be responsible for the loss in conversion with the recycled catalyst.

3.3.9 Catalytic activity for benzyl amine oxidation.

Recently, it was reported that $V(O)(HQ)_2(O^iPr)$ catalyzes the aerobic oxidation of primary aromatic amines to imines under mild conditions (60 °C in CH_3CN, 12-24 h).[6] Inspired by these results, we tested $V(O)(HQ)_2(O^iPr)_x$-A380 for the catalytic oxidation of

benzyl amine under analogous conditions as the homogenous. After 21 h, we found that our heterogeneous catalyst selectively converted 44 % of benzyl amine to the corresponding imine while 96 % conversion was seen with the homogeneous catalyst. These results open up the potential reactivity of $V(O)(HQ)_2(O^iPr)_x$-A380 towards other primary amines as well as unsymmetrical imines by reaction of alcohols and amines as demonstrated in the homogeneous system.

3.4 Conclusions

Using a multi-step grafting method, tethering a molecular analog of a *bis*(8-hydroxyquinolinato)vanadium complex, $V(O)(HQ)_2(O^iPr)_x$-A380, to an aminopropyl functionalized silica resulted in an unexpected ligand oxidation. The grafting and tethering reactions were followed using elemental analysis, IR, and MAS NMR (^{13}C, ^{29}Si and ^{51}V) spectroscopies. However, similar to the homogeneous analog, $V(O)(HQ)_2(O^iPr)_x$-A380 oxidizes benzyl alcohol selectively to benzaldehyde in air although at a much slower rate. Since similar base effects and Hammett trends are observed for the homogeneous and heterogeneous versions of the catalyst, we believe the catalysts operate via a similar mechanism. We also found that $V(O)(HQ)_2(O^iPr)_x$-A380 was effective for the aerobic oxidation of benzyl amines, which supports the susceptibility of the amine tether to oxidation by V. Unexpected oxidation of the amine tether resulted in a less active V(IV) species. This species is also more vulnerable to imine hydrolysis, which could explain catalyst leaching results. Using ligand tethers with non-oxidizable groups would prevent the formation of the V(IV) species and perhaps lead to higher rates. We also believe that V(V) species bound through two neighboring ligand tethers may have constricted rearrangement in the transition

state and slow down the reaction rate. It is extremely important to consider both the grafted silane and ligand tethers when performing multi-step syntheses of silica-supported molecular catalysts in order to prevent unintentional side reactions.

3.5 References

1. Wigington, B. N., Drummond, M. L., Cundari, T. R., Thorn, D. L., Hanson, S. K., Scott, S. L., , *Chem. Eur. J.* **2012,** *18*, 14981-14988.

2. Madonna, S., Marcowycz, A., Lamoral-Theys, D., Dessolin, J., Pirker, C., Spiegl-Kreinecker, S., Biraboneye, C-A., Berger, W., Kiss, R., and Kraus, J-L., *J. Heter. Chem.* **2010,** *47*, 719-723.

3. Hanson, S. K., Wu, R., and Silks, L. A. , *Org. Lett.* **2011,** *13*, 1908-1911.

4. Scheidt, W. R., *Inorg. Chem.* **1973,** *12*, 1758-1761.

5. Kodama, S.; Yoshida, J.; Nomoto, A.; Ueta, Y.; Yano, S.; Ueshima, M.; Ogawa, A., *Tetrahedron. Lett.* **2010,** *51*, 2450-2452.

6. Wang, L.; Chen, B.; Ren, L.; Zhang, H.; Lü, Y.; Gao, S., *Chin. J. Catal.* **2014,** *36*, 19-23.

7. Uibel, R. H., and Harris, J. M., *Anal. Chem.* **2002,** *74*, 5112-5120.

8. Uibel, R. H., and Harris, J. M., *Anal. Chem.* **2005,** *77*, 991-1000.

9. Weaver, M. R., and Harris, J. M., *Anal. Chem.* **1989,** *61*, 1001-1010.

10. Phillips, J. P., *Chem. Rev.* **1956,** *56*, 271-297.

11. Ek, S., Iiskola, E. I., Niinisto, L., Vaittinen, J., Pakkanen, T. T., Kera¨nen, J., and Auroux, A., *Langmuir* **2003,** *19*, 10601-10609.

12. Ek, S., Iiskola, E. I., and Niinisto, L., *Langmuir* **2003,** *19*, 3461-3471.

13. Juvaste, H., Iiskola, E. I., and Pakkanen, T. T., *J. Organomet. Chem.* **1999,** *587*, 38-45.

14. Daehler, A., Boskovic, S., Gee, M. L., Separovic, F., Stevens, G. W., and O'Connor, J. O., *J. Phys. Chem. B* **2005,** *109*, 16263-16271.

15. Phillips, J. P., and Merritt, L. L. , *J. Am. Chem. Soc.* **1949,** *71*, 3984-3986.

16. Shah, T. B., Raj, L. M., and Dixit, R. B., *Int. J. Poly. Mat.* **2003,** *52*, 9-20.

17. Shah, T. B., Dixit, R. B., and Dixit, B. C., *J. Therm. Anal. Cal.* **2008,** *92*, 505-512.

18. Rice, G. L., and Scott, S. L. , *Langmuir* **1997,** *13* (1545-1551).

19. Coetzee, J. F.; Padmanabhan, G. R., *J. Am. Chem. Soc.* **1965,** *87*.

20. Hall, H. K., *J. Phys. Chem.* **1956,** *60*.

21. Yang, H.; Thyrion, F. C., *Int. J. Chem. Kinet.* **1994,** *26*.

Chapter 4. Silylalkylboranes and their Silica-supported Analogs: Implications for Metal-free Catalysis

4.1 Introduction

Frustrated Lewis pairs (FLPs) represent a new strategy for the development of metal-free catalytic small molecule activation under mild conditions. An FLP is a combination of a Lewis acid and base that is sterically precluded from forming a Lewis acid-base adduct. Typical pairs consist of a bulky borane (acid) and a bulky phosphine or amine (base). Since the initial report in 2006, the chemistry of FLPs has expanded dramatically.[1] In addition to well-studied FLP-catalyzed hydrogenation,[2] interesting FLP reactivity towards a diverse set of small molecule substrates has been observed. The bifunctional and unquenched nature of the FLPs makes them capable of reacting with alkenes, alkynes, disulfides, diynes, N_2O, and CO_2, among others (see Scheme 4.1).[3]

Such variety suggests a large range of potential applications. In particular, the ability of FLP-derived systems to reversibly bind and release CO_2 is an exciting development, since it offers new routes to capture and convert this environmentally important molecule. In combination with the ability of FLPs' to cleave H_2 heterolytically, new CO_2 hydrogenation chemistry was discovered leading to CH_3OH.[4, 5]

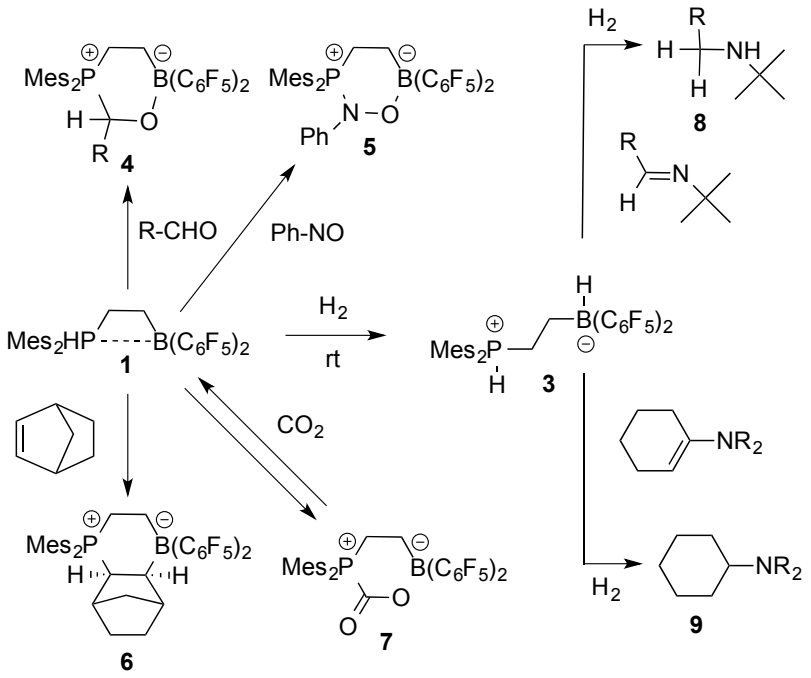

Scheme 4.1. Metal-free reactions of an intramolecular FLP (**1**). Adapted from ref. 4.[6]

All FLP chemistry reported to-date has been homogeneous (i.e., in solution), whereas catalysts may be more practical when they are heterogeneous (i.e., in the solid phase). We prepared two silylpropylboranes as molecular models for silica-supported boranes. The former were characterized using NMR to confirm their structures. This information is invaluable for investigating and assigning the structures of the silica-supported boranes. The latter were prepared using a two-step methodology in which allylsilanes were installed, then hydroborated using Piers' borane to give tethered Lewis acid sites. The materials were characterization by IR and NMR spectroscopies and their structures assessed by comparison to the molecular analogs.

4.2 Experimental Section:

4.2.1 Reagents and Materials

General Considerations. All reactions involving air- and/or moisture-sensitive compounds were carried out under an inert atmosphere in Schlenk-type glassware and/or a N_2-filled glovebox. Allyldimethylsilyl chloride (ADMSCl, 97 %, Alfa Aesar) and allyltriethoxysilane (ATES, 95 %, Gelest) were used as received. Triethylamine (NEt_3, ≥ 99.5 %) was purchased from Sigma-Aldrich and dried over CaH_2, then stored over 4 Å molecular sieves. $HB(C_6F_5)_2$ was prepared according to a literature procedure.[1] Pentane (ACS grade, ≥ 98 %, Fisher) was dried over CaH_2, degassed by three freeze-pump-thaw cycles, and vapor-transferred to an air-free Schlenk tube prior to use. Toluene (ACS grade, ≥ 99.5 %, Fisher) was purified by passage first through an alumina-packed column, then through a second column packed with CuO/Al_2O_3 (Q5 catalyst, Sigma-Aldrich).

A non-porous, fumed silica (Aerosil 380, denoted A380), with a surface area of ca. 380 m^2/g and a primary particle size of 7 nm, was supplied by Evonik. It was thermally pretreated under vacuum (10^{-4} Torr) at either 200 or 500 °C for 18-24 h. The resulting dry silicas are denoted $A380_{200}$ and $A380_{500}$, respectively. Their accessible hydroxyl (≡SiOH) contents, as measured by $VOCl_3$ chemisorption,[7] are 1.43 and 0.89 mmol/g, respectively. The absence of physisorbed water was confirmed by the complete disappearance of the bending mode δ(HOH) at ca. 1635 cm^{-1} in the IR spectrum. All dry materials were stored in an argon-filled glove box to prevent readsorption of atmospheric moisture.

4.2.2 Characterization

NMR spectra of the molecular complexes were obtained on Bruker ARX 300 (^{1}H: 300 MHz, ^{13}C: 75 MHz), Bruker Avance 400 MHz, or Varian Inova 500 (^{1}H: 500 MHz, ^{13}C: 126 MHz, ^{19}F: 470 MHz, ^{11}B: 160 MHz) spectrometers. ^{1}H NMR and ^{13}C NMR chemical shifts (δ) are given relative to $Si(CH_3)_4$, and referenced to the solvent signal (^{19}F rel. to external $CFCl_3$; ^{11}B rel. to external $BF_3{\cdot}Et_2O$). NMR assignments are supported by additional 1D and 2D NMR experiments. NMR spectra were recorded at 25 °C unless otherwise stated, and chemical shifts are reported in ppm. NMR solvents (CD_2Cl_2, C_6D_6, and $CDCl_3$) were purchased from Cambridge Isotopes, dried over CaH_2, vacuum distilled prior to use, and stored over 4 Å molecular sieves in a glovebox.

In the silica grafting work, solution-state (^{1}H, ^{11}B, ^{19}F) NMR spectra were recorded on a Bruker DMX 500 MHz spectrometer, equipped with a 5 mm BBFO 1H-F/X probe, and referenced to $Si(CH_3)_4$ at 0 ppm. Solid-state NMR spectra were recorded on a Bruker DSX 300 MHz WB spectrometer operating at 7.0 T, with frequencies of 75.4 and 59.7 MHz for ^{13}C and ^{29}Si, respectively. Samples were packed under an argon atmosphere into 4 mm zirconia rotors and sealed with Torlon o-ring caps (Bruker). ^{29}Si cross-polarization/magic angle spinning (CP/MAS) spectra were obtained using a 90 ° pulse length of 3.00 μs, a contact time of 5 ms, and high power proton decoupling during detection. Typically, 25,000 scans were acquired at a spinning rate of 10 kHz. Chemical shifts were referenced to tetrakis(trimethylsilyl)silane (Aldrich). ^{13}C CP/MAS spectra were obtained using a 90 ° pulse length of 3.7 μs, a contact time of 2 ms, and high power proton decoupling during detection. Typically, 25,000 scans were acquired at a spinning rate of 10 kHz. Chemical shifts were referenced to tetrakis(trimethylsilyl)silane.

^{11}B and ^{19}F spectra were recorded on a Bruker DSK 500 MHz WB spectrometer operating at 11.7 T, with frequencies of 160.5 and 470.6 MHz, respectively. Single-pulse ^{19}F MAS NMR spectra were acquired at both 12 and 14 kHz to identify isotropic peaks; typically, 16,000 scans were collected. Chemical shifts were referenced to polytetrafluoroethylene (PTFE, δ = -122 ppm). ^{11}B MAS spectra were obtained using a Hahn-echo pulse sequence to correct for background signal from the probe. Generally, 4,000 scans were collected at a spinning rate of 10 kHz. Chemical shifts were referenced to BF_3•Et_2O liquid (Aldrich, δ = 0 ppm).

IR spectra were recorded under Ar in transmission mode on a Bruker ALPHA spectrometer. Self-supporting pellets were made using a hand press (International Crystal Laboratories) to compact 3-5 mg silica into disks of 4 mm diameter. For background and sample spectra, 32 scans were acquired at a resolution of 4 cm^{-1}.

4.2.3 Synthesis of triethoxysilylpropyl(penta-fluorophenyl)borane ***(1)***

Allyltriethoxysilane (22.6 μL, 0.100 mmol) and $HB(C_6F_5)_2$ (34.6 mg, 0.100 mmol) were dissolved in CD_2Cl_2 (1 mL) and taken up with a pipette several times to ensure thorough mixing. The resulting solution was clear. We were unable to isolate crystals due to the oil-like nature of the silane. ^1H NMR (500 MHz, 299 K, CD_2Cl_2): δ = 4.11 (6H, q, -OCH_2CH$_3$), 1.47 (2H, q), 1.35 (2H, t), 1.19 (9H, t, -OCH$_2$CH_3), 1.09 (2H, t). $^{13}C\{^1H\}$ NMR (125 MHz, 298K, CD_2Cl_2): δ = 148.5 (dm, $^1J_{FC}$= 240 Hz, *o*-C_6F_6), 140.1 (dm, $^1J_{FC}$= 250 Hz, *p*-C_6F_6), 137.5 (dm, $^1J_{FC}$= 250 Hz, *m*-C_6F_6), 63.6, 22.4, 17.4, 16.8, 9.3 ppm. $^{11}B\{^1H\}$ NMR (64 MHz, 298 K, CD_2Cl_2): δ = 8.7 ppm (s). $^{29}Si\{DEPT\}$ NMR (99 MHz, 298 K, CD_2Cl_2): -

40.3 ppm. ^{19}F NMR (282 MHz, 299 K, CD_2Cl_2): δ = -133.1 (dd, 4F, *o*-F), -158.7 (t, 2F, *p*-F), -164.7 ppm (dq, 4F, *m*-F) [$\Delta\delta^{19}F_{m,p}$ = 6.0 ppm].

4.2.4 Synthesis of chlorodimethylsilylpropyl(penta-fluorophenyl)borane ***(2)***

Allylchlorodimethylsilane (12.1 μL, 0.0800 mmol) and $HB(C_6F_5)_2$ (27.7 mg, 0.0800 mmol) were dissolved in C_6D_6 (1 mL) and taken up with a pipette several times to ensure thorough mixing. The resulting solution was clear. ^1H NMR (500 MHz, 298 K, tol-d_8): δ = 1.97, 1.62 (m), 0.87 (t), 0.72 (m), 0.18 (s) $^{11}B\{^1H\}$ NMR (64 MHz, 198 K, tol-d_8): δ = 73.8 ppm (s). ^{19}F (282 MHz, 298 K, tol-d_8): δ = -130.5 (dd, 4F, *o*-F), -147.2 (t, 2F, *p*-F), -161.0 ppm (dq, 4F, *m*-F) [$\Delta\delta^{19}F_{m,p}$ = 13.8 ppm].

4.2.5 Silica Functionalized with Allylmonoethoxysilyl Groups (AMES-A380)

In a 150 mL Schlenk flask, $A380_{200}$ (1.0 g) was suspended in 60 mL toluene. Allyltriethoxysilane (ATES, 1.4 mL, 6.2 mmol) and *p*-toluenesulfonic acid (6.3 mg, 0.037 mmol) were added. The mixture was stirred vigorously at 65 °C for 1 day. The solid was isolated by filtration, washed with toluene (2 x 100 mL), then $CHCl_3$ (100 mL), and dried at 95 °C under vacuum (0.1 mTorr) for 18 h.

4.2.6 Silica Functionalized with Allyldimethylsilyl Groups (ADMS-A380)

In a 150 mL Schlenk flask, $A380_{500}$ (1.0 g) was suspended in 60 mL toluene. Allyldimethylsilyl chloride (ADMSCl, 0.50 mL, 3.4 mmol) and triethylamine (0.50 mL, 3.6 mmol) were added. The mixture was stirred vigorously at 65 °C for 1 day. The solid was

isolated by filtration, washed with toluene (2 x 100 mL), then $CHCl_3$ (100 mL), and dried at 95 °C under vacuum (0.1 mTorr) for 18 h.

4.2.7 Hydroboration of AMES-A380$_{200}$

In a 150 mL Schlenk flask, AMES-A380$_{200}$ (1.0 g) and $HB(C_6F_5)_2$ (510 mg, 1 equiv. based on the original accessible hydroxyl content of the silica, 1.43 mmol/g) were suspended in 60 mL toluene. The suspension was vigorously stirred at room temperature for 24 h. The solid, $B(C_6F_5)_2$-AMES-A380$_{200}$, was isolated by filtration, washed with toluene (3 x 100 mL), and dried at 100 °C under vacuum (0.1 mTorr) for 18 h. Elemental analysis: C: 5.50 %, B: 0.46 %.

4.2.8 Hydroboration of ADMS-A380$_{500}$

In a 150 mL Schlenk flask, ADMS-A380$_{200}$ (822 mg) and $HB(C_6F_5)_2$ (256 mg, 1 equiv. based on the original accessible hydroxyl content of the silica, 0.89 mmol/g) were suspended in 60 mL toluene. The suspension was stirred vigorously at room temperature for 1 h. The solid, $B(C_6F_5)_2$-ADMS-A380$_{200}$, was isolated by filtration, washed with toluene (3 x 50 mL), then dried at 100 °C under vacuum (0.1 mTorr) for 18 h. Elemental analysis: C: 5.35 %, B: 0.50 %.

In another procedure, ADMS-A380$_{500}$ (924 mg) was allowed to react with $HB(C_6F_5)_2$ (285 mg, 1 equiv. based on the original accessible hydroxyl content of the silica, 0.89 mmol/g) at 80 °C for 2 d to give $B(C_6F_5)_2$-ADMS-A380$_{500}$-80 °C. Elemental analysis: C: 5.50 %, B: 0.42 %.

4.3 Results and Discussion

4.3.1 Synthesis of a triethoxysilylpropylborane

Allyltriethoxysilane was chosen as a simple, molecular model for an allyl-functionalized silica surface. The feasibility of its hydroboration was explored first in solution. Anti-Markovnikov hydroboration with Piers' borane ($HB(C_6F_5)_2$) yielded triethoxysilylpropyl-*bis*(pentafluorophenyl)borane (**1**) as an oil. Three-coordinate alkylboranes typically have ^{11}B chemical shifts ranging from 60-80 ppm.[8] However, the ^{11}B NMR spectrum of **1** recorded at 299 K exhibits a sharp singlet at 8.7 ppm, Figure 4.1, typical of a four-coordinate borane. This chemical shift suggests a B-O interaction involving one of the ethoxy substituents on silicon. (Another small signal at 40 ppm is also present, and may be a three-coordinate species with a B-O bond, resulting from decomposition following ethoxy coordination.)

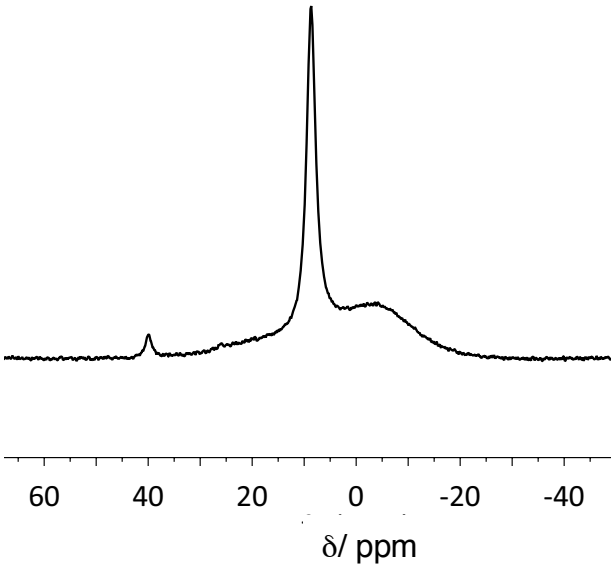

Figure 4.1. ^{11}B NMR of **1** (64 MHz, 299 K, CD_2Cl_2). The broadness under the peak is caused by probe background.

The ^{19}F NMR spectrum, Figure 4.2, shows further evidence for the B-O interaction via a small $\Delta\delta_{m,p}$ separation of just 6.0 ppm for the pentafluorophenyl resonances, similar to that for other four-coordinate pentafluorophenylboranes and much less than that for three-coordinate analogs (>15 ppm).[9, 10] Formation of the proposed intramolecular adduct is shown in Scheme 4.2.

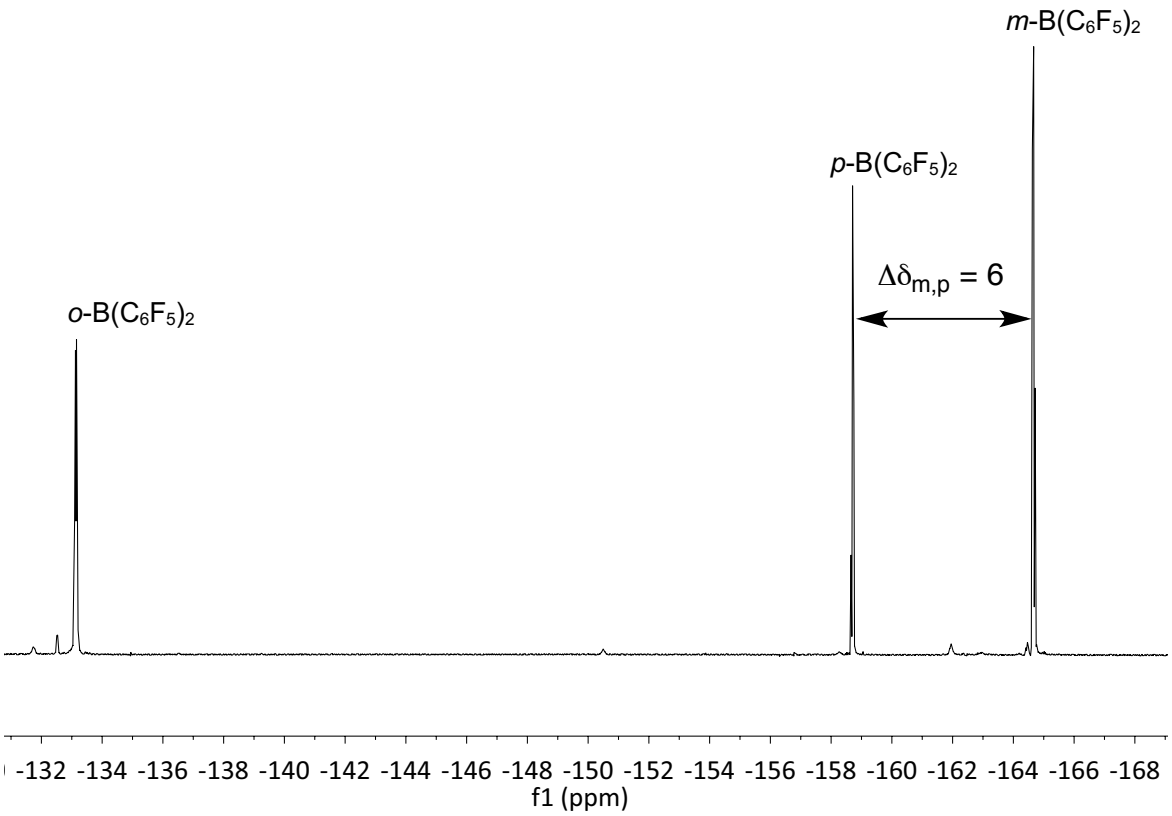

Figure 4.2. ^{19}F NMR of δ/ ppm Hz, 299 K, [CD_2Cl_2).

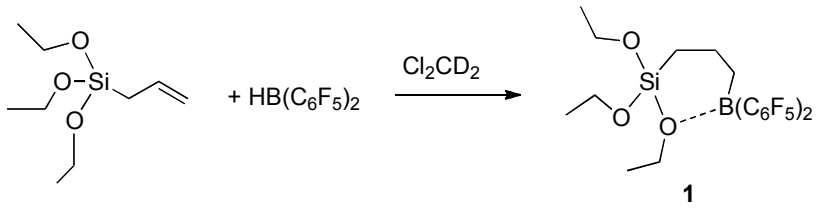

Scheme 4.2. Synthesis of **1** by hydroboration of allyltriethoxysilane with Piers' borane.

The variable temperature ^1H NMR spectra in Figure 4.3 reveal the dynamic behavior of **1**. Below 218 K, both the CH_2 and CH_3 signals of the ethoxy groups split into two sets of signals, both in a 2:1 ratio, Figure 1, consistent with freezing out of rapid exchange of the

ethoxy groups via reversible B-O bond cleavage. Low temperature ^{13}C, ^{11}B, ^{19}F, and ^{29}Si spectra were also recorded and are consistent with a B-O interaction (see Appendix I).

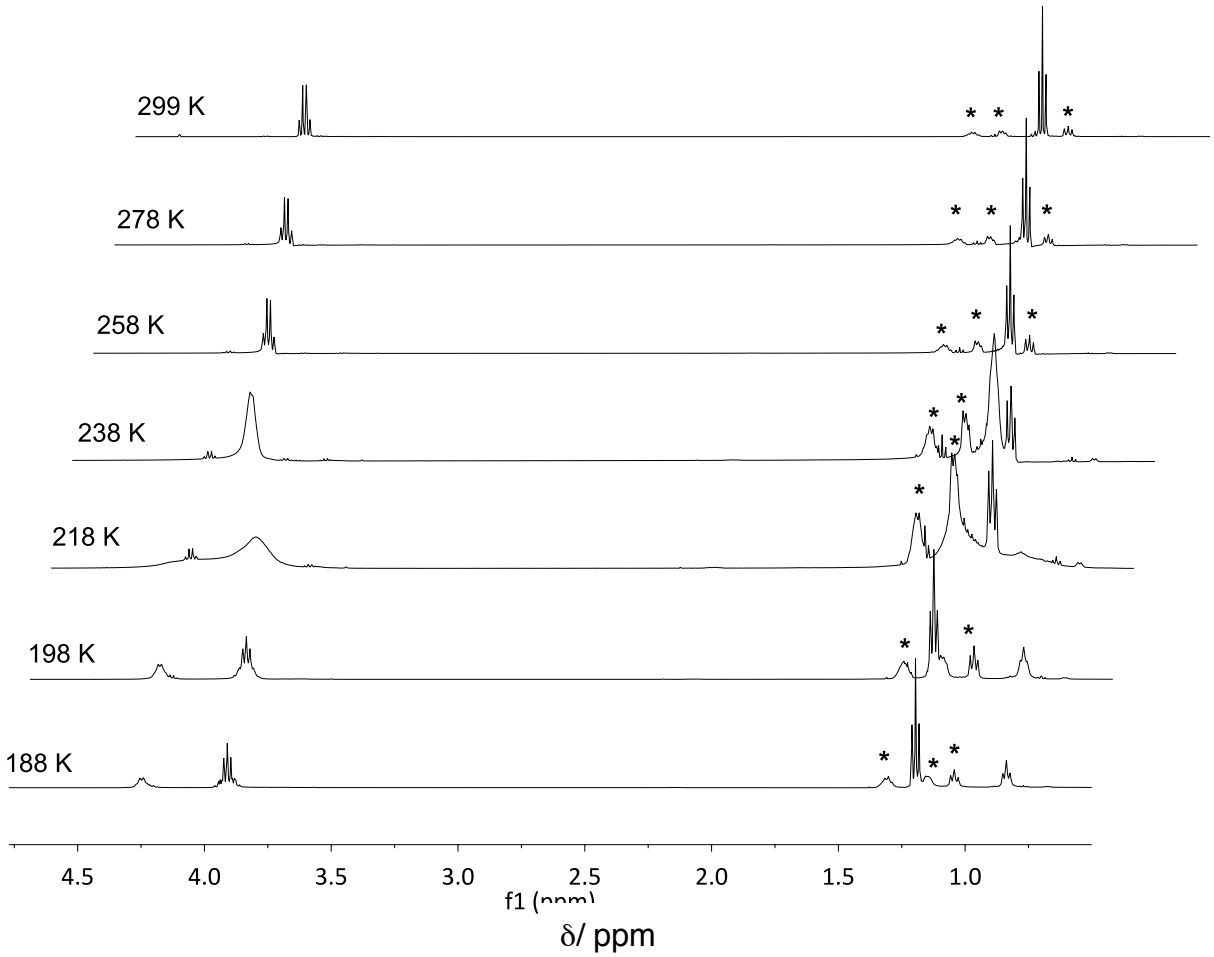

Figure 4.3. Variable temperature ^{1}H NMR study of triethoxysilylpropyl(pentafluorophenyl)-borane (**1**). Propyl signals are noted with *.

4.3.2 Synthesis and reactivity of a non-adduct-forming silylpropylborane

Since the siloxane oxygens of silica are much less electron-rich than those of alkoxysilanes, use of a silane without alkoxy substituents was explored, to avoid the

formation of an intramolecular B-O adduct observed for **1**. The absence of adduct formation and ethoxy ligand exchange products may ensure cleaner reactions and facilitate product identification by NMR. Allylchlorodimethylsilane undergoes anti-Markovnikov hydroboration with Piers' borane ($HB(C_6F_5)_2$) to yield chlorodimethylsilylbis(pentafluorophenyl)borane (**2**), Scheme 4.3.

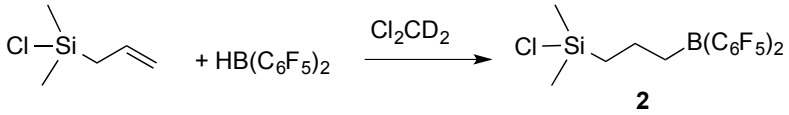

2

Scheme 4.3. Synthesis of **2** by hydroboration of allylchlorodimethylsilane with Piers' borane.

NMR characterization revealed no interactions between boron in **2** and any other part of the silane. The ^{19}F NMR spectrum in Figure 4.4 shows a much larger splitting between *meta*- and *para*-F signals ($\Delta\delta_{m,p}$= 13.8 ppm) compared to **1**. Furthermore, the ^{11}B chemical shift of 73.8 ppm indicates a three-coordinate boron center (see Appendix I).

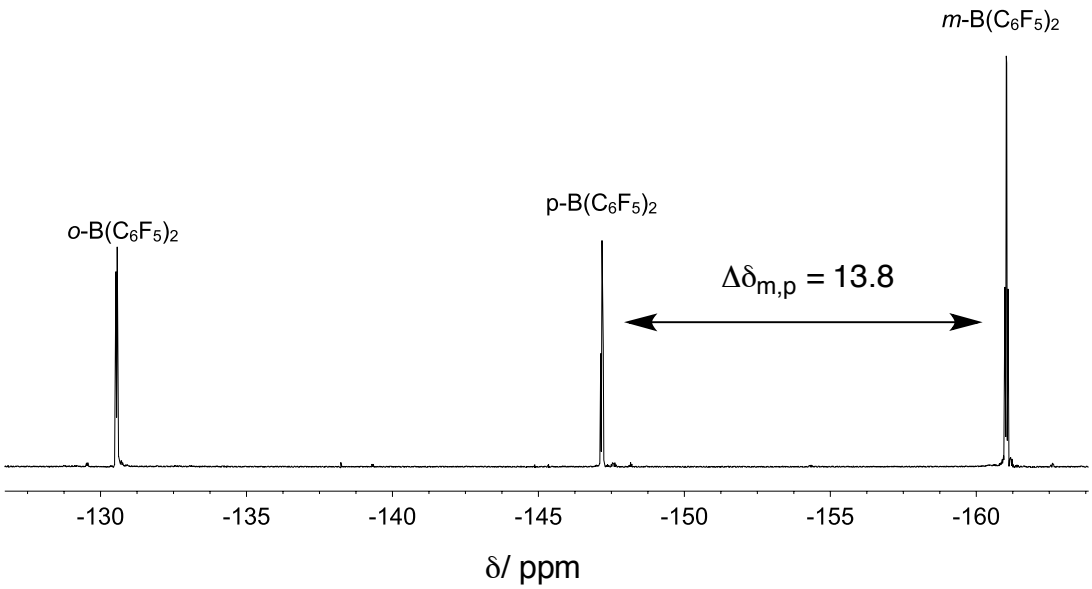

Figure 4.4. ^{19}F NMR spectra of **2**, recorded at 282 MHz and 298 K in toluene-d_8.

4.3.3 Allyl-functionalized silicas and silica-supported boranes

Our initial effort to create a site-isolated borane species involved pretreating silica at 200 °C under vacuum ($A380_{200}$), which removes adsorbed water without inducing dehydroxylation of the silica surface. We then used a two-step grafting procedure to install the silica-supported borane. First, allylmonoethoxysilyl-modified silica (AMES-$A380_{200}$) was prepared in one step by grafting allyltriethoxysilane (ATES) onto $A380_{200}$, Scheme 5.1. Anchoring the silane to the silica via reaction with multiple silanols may result in more robust anchoring of the borane. This material is referred to as AMES-$A380_{200}$. Post-synthesis silica grafting reactions involving trialkoxysilanes often occur through condensation of one or two alkoxysilyl groups.[11, 12] Therefore, this material is represented as being anchored through two siloxy bonds to silica, Scheme 4.4.

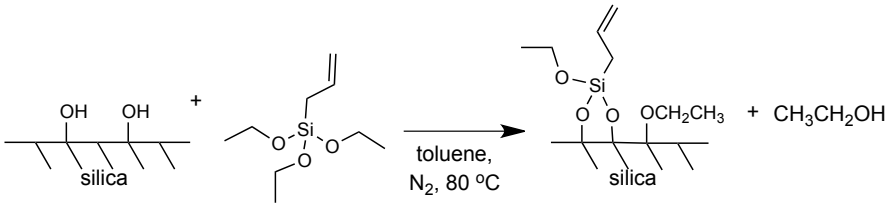

Scheme 4.4. Grafting ATES on silica $A380_{200}$ to give $B(C_6F_5)_2$-AMES-$A380_{200}$

The IR spectrum confirms the disappearance of the majority of the accessible silanols, represented by the sharp peak at 3747 cm^{-1}, Fig. 4.5. A very weak, broad peak centered at 3670 cm^{-1} remains in the υ(O–H) region after reaction, representing inaccessible (probably internal) hydroxyl groups that are perturbed by hydrogen-bonding.[3] In the υ(C–H) region, several bands appear between 3100 and 2800 cm^{-1}, assigned to the C–H stretches of the allyl methylene, as well as the methyl and methylenes of uncondensed ethoxy groups. In particular, a high frequency vinylic υ(=C-H) band is visible at 3085 cm^{-1}. The allyl group also gives rise to a characteristic υ(C=C) band at 1634 cm^{-1}, which is clearly evident in Fig. 4.5. New methyl and methylene deformations can also be seen at 1422 and 1395 cm^{-1}.

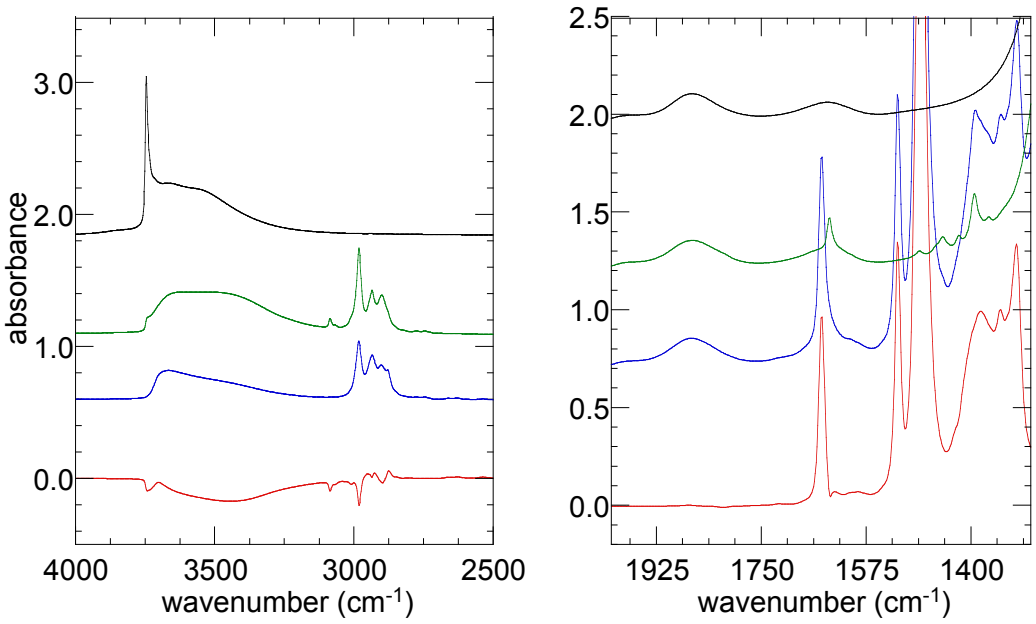

Figure 4.5. Transmission IR spectra of $A380_{200}$ (black), after allyltriethoxysilyl modification (green), and after hydroboration with $HB(C_6F_5)_2$ to give $B(C_6F_5)_2$-AMES-$A380_{200}$ (blue). The difference spectrum, before and after the hydroboration reaction, is shown in red.

Allylic hydroboration involving Piers' borane, which occurs readily in solution, was tested in the heterogeneous system. AMES-$A380_{200}$ was treated with $HB(C_6F_5)_2$ at room temperature, according to Scheme 4.5. IR spectra of AMES-$A380_{200}$ before and after hydroboration are shown in Figure 4.5. The vinylic υ(=C–H) band at 3085 disappears, and the υ(C=C) band at 1634 cm^{-1} appears to shift to 1649 cm^{-1}, as the allyl is consumed. The C_6F_5 ring breathing modes now dominate the spectrum. The characteristic band at 1472 cm^{-1}, which involves B–C stretching, C–B–C wagging, and ring-breathing, confirms the presence of the grafted borane.[13] The difference spectrum, shown in red in Fig. 4.5, provides clear evidence for the transformation of the allyl group and the incorporation of the borane. Anti-

Markovnikov addition is presumed based on the molecular system.

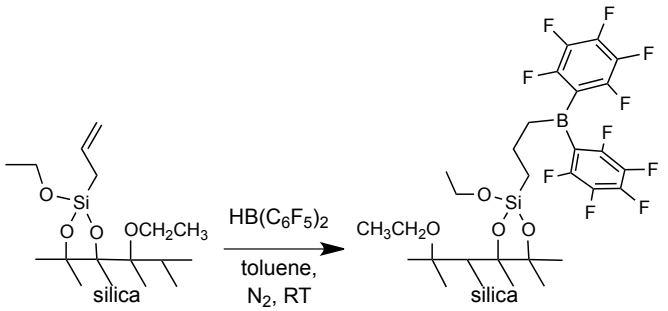

Scheme 4.5. Hydroboration of AMES-A380$_{200}$ to give B(C_6F_5)$_2$-AMES-A380$_{200}$.

Solid-state ^{19}F and ^{11}B MAS NMR chemical shifts are sensitive to the boron coordination environment. Typically, the peak separation between the *para*- and *meta*-F resonances in neutral, three-coordinate pentafluorophenylboranes is >15 ppm. In four-coordinate boranes, the separation decreases as the *para*-F resonance shifts upfield.[9, 10, 14] The ^{11}B chemical shift also appears at higher field for tetracoordinate species, relative to tricoordinate analogs.[8]

The ^{19}F MAS NMR spectrum of B(C_6F_5)$_2$-AMES-A380$_{200}$ shows two sets of signals: one sharp, and one broad, Figure 4.6a. The two intense, broad peaks are assigned by their chemical shifts, -134 (*o*-F) and -166 ppm (*m*-F). The *p*-F signal is at -152 ppm. The splitting between the *m*- and *p*-F signal is 14 ppm, suggestive of a tricoordinate borane. The chemical shifts of the broad ^{19}F NMR signals are roughly the same as those of the molecular analog $B(C_6F_5)_2(CH_2)_3Si(OCH_2CH_3)_3$, -133.1, -158.7 and -164.7 ppm, Fig. 4.2.

The spectrum does not appear to have the 2:1:2 ratio one would expect for pentafluorophenyl groups. Spinning at 14 kHz produces side bands 30 ppm from the isotopic

peak. For the *o,m*-F signals, they occur at -164 and -136 ppm, respectively. This causes the *o,m*-F signals to simply exchange spinning side-band intensity, while the *p*-F signal loses it.

The appearance of the sharp peaks suggests a mobile, physisorbed species. Its chemical shifts are in good agreement with those of pentafluorobenzene.[14] In fact, when the solid was stirred overnight in toluene, ^{19}F solution-state NMR revealed the presence of pentafluorobenzene in the supernatant.

The ^{11}B spectrum shows two major peaks, at 19 and 43 ppm, Figure 4.6b. The latter is characteristic of a tricoordinate borane bearing an oxygen-donor ligand (for which molecular analogs show chemical shifts between 20 - 50 ppm).[8] The spectrum of **1** also contains a minor boron signal located around 40 ppm, Fig. 4.1, which may be a B-O-containing species. We assign the peak at 19 ppm to four-coordinate borane-modified AMES-A380$_{200}$, as shown in Scheme 4.5 by analogy to $B(C_6F_5)_2(CH_2)_3Si(OCH_2CH_3)_3$ with a ^{11}B NMR signal at 8.7 ppm.

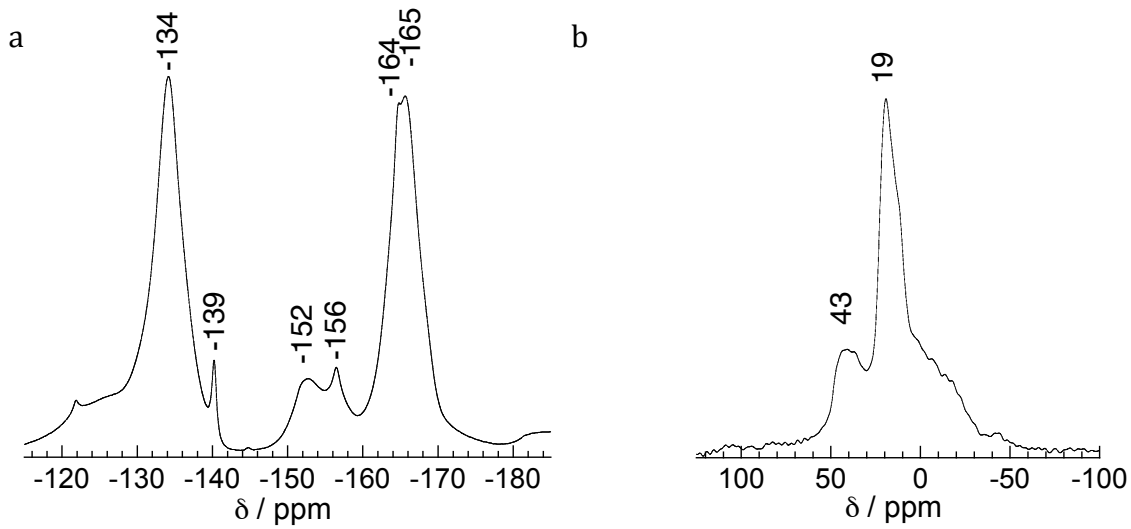

Figure 4.6. Solid-state MAS NMR of $B(C_6F_5)_2$-AMES-$A380_{200}$: (a) ^{19}F (spin rate 14 kHz); and (b) ^{11}B (spin rate 10 kHz).

The ^{19}F and ^{11}B spectra of $B(C_6F_5)_2$-AMES-$A380_{200}$ revealed a complex mixture of products. As shown with the molecular systems, boron is capable of interacting with oxygen atoms in the silane. Grafting a silane with no oxygen present, such as allyldimethylchlorosilane, we hoped to avoid any side reactions that may have occurred during the synthesis of $B(C_6F_5)_2$-AMES-$A380_{200}$. We also used silica pretreated at higher temperature (500 °C) to control the surface hydroxyl density by dehydration and partial dehydroxylation of the surface.

We used a similar two-step grafting procedure as $B(C_6F_5)_2$-AMES-$A380_{200}$ to install the silica-supported borane. Allyldimethylsilyl-modified silica (ADMS-$A380_{500}$) was prepared in one step by grafting allyldimethylsilyl chloride (ADMSCl) onto $A380_{500}$ in the presence of a stoichiometric amount of base (NEt_3), Scheme 4.6.

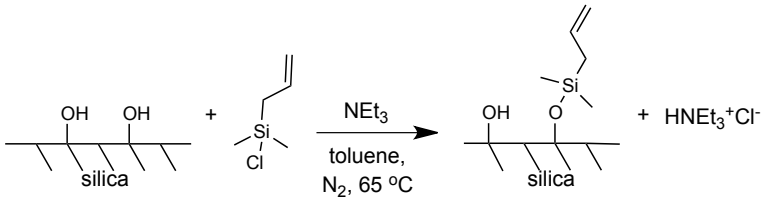

Scheme 4.6. Grafting ADMSCl onto $A380_{500}$, to give $B(C_6F_5)_2$-ADMS-$A380_{500}$.

The IR spectrum after grafting ADMSCl confirms the disappearance of the majority of the accessible silanols, represented by the peak at 3747 cm^{-1}, Fig. 4.7, leaving only a weak, broad peak centered at 3670 cm^{-1}. In the υ(C–H) region, the vinylic υ(=C-H) band appears at 3085 for the ADMS group. The characteristic υ(C=C) band of the allyl group is also visible at 1634 cm^{-1}, in addition to the methyl and methylene deformations between 1500 and 1300 cm^{-1}.

ADMS-$A380_{500}$ was hydroborated using Piers' borane. The anticipated product is $B(C_6F_5)_2$-ADMS-$A380_{500}$, as shown in Scheme 4.7.

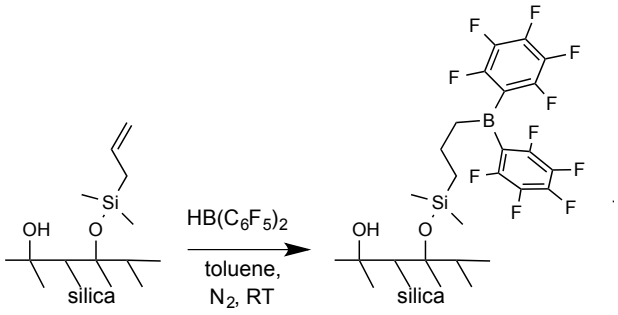

Scheme 4.7. Hydroboration of ADMS-$A380_{500}$ to give $B(C_6F_5)_2$-ADMS-$A380_{500}$.

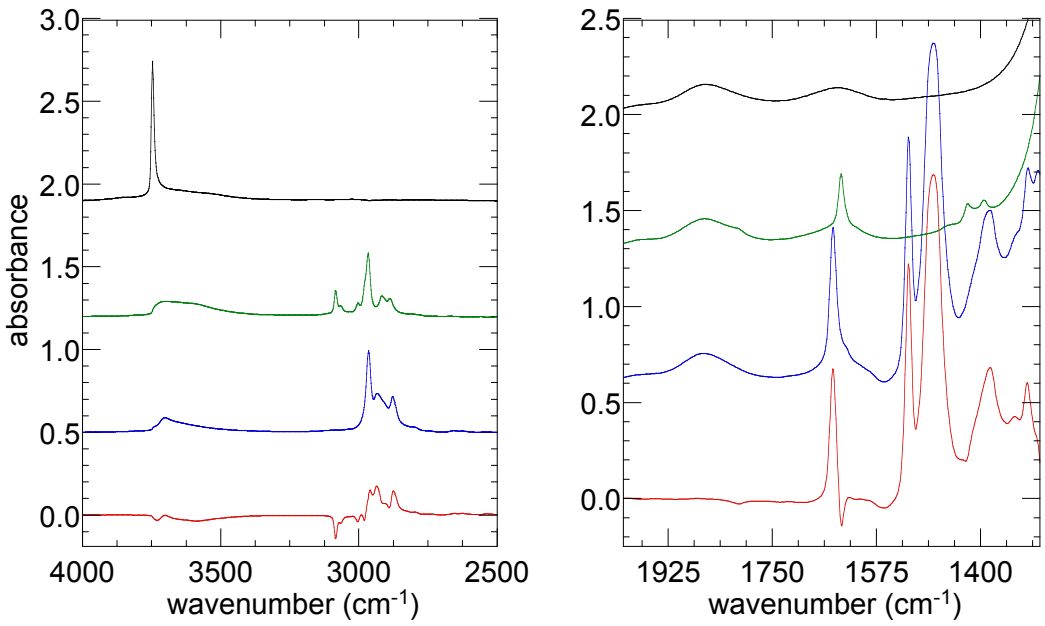

Figure 4.7. Transmission IR spectra of $A380_{500}$ (black), after allyldimethylsilyl modification (green) and after hydroboration with $HB(C_6F_5)_2$ to give $B(C_6F_5)_2$-ADMS-$A380_{500}$ (blue). The difference spectrum, before and after the hydroboration reaction, is shown in red.

The IR spectrum of the borane-modified silica is shown in Fig. 4.7. The vinylic υ(=C–H) band at 3085 is no longer present, and the υ(C=C) band at 1634 cm^{-1} appears to shift to 1649 cm^{-1}, as with the previous materials. The C_6F_5 ring breathing modes dominate the spectrum, and the band at 1472 cm^{-1}, involving B–C stretching, C–B–C wagging, and ring-breathing, confirms the presence of the borane.[4]

$B(C_6F_5)_2$-ADMS-$A380_{500}$ was also characterized using NMR. Despite our effort to form a single species the ^{19}F MAS NMR spectrum, Fig. 4.8a, contains a similar set of two pentafluorophenyl signals as $B(C_6F_5)_2$-AMES-$A380_{200}$. The most intense peaks, assigned to *o*-F and *m*-F, are broad and have prominent shoulders due to spinning side-bands (30 ppm from the isotopic peak). The sharp signals at -139 and -155 ppm are the *o*-F and *p*-F signals,

respectively, of physisorbed pentafluorobenzene. No sharp *m*-F signal is visible, although it may be obscured by the broad *m*-F signal. Upon washing the material with toluene, the sharp peaks disappear while the broad peaks at -133, -155, and -166 ppm remain, Fig. 4.8b. The relative position of this peak makes it difficult to determine whether the boron is three- or four-coordinate. The $\Delta\delta$(*m*-F, *p*-F) separation is 11 ppm, which is between the separation found for four-coordinate **1** (with a B-O interaction) and three-coordinate **2**.

The ^{11}B MAS NMR spectrum, Figure 4.8c, is very broad, reflecting a mixture of boron species. The most prominent peaks appear at 13 and 19 ppm, which differ significantly from that of the molecular analog, **2**, (73.8 ppm). There is also a sharp peak at 0.8 ppm, which may be a physisorbed four-coordinate borate. Similar to $B(C_6F_5)_2$-AMES-$A380_{200}$, $B(C_6F_5)_2$-ADMS-$A380_{500}$ may reflect some type of B-O interaction with silica oxygen atoms.

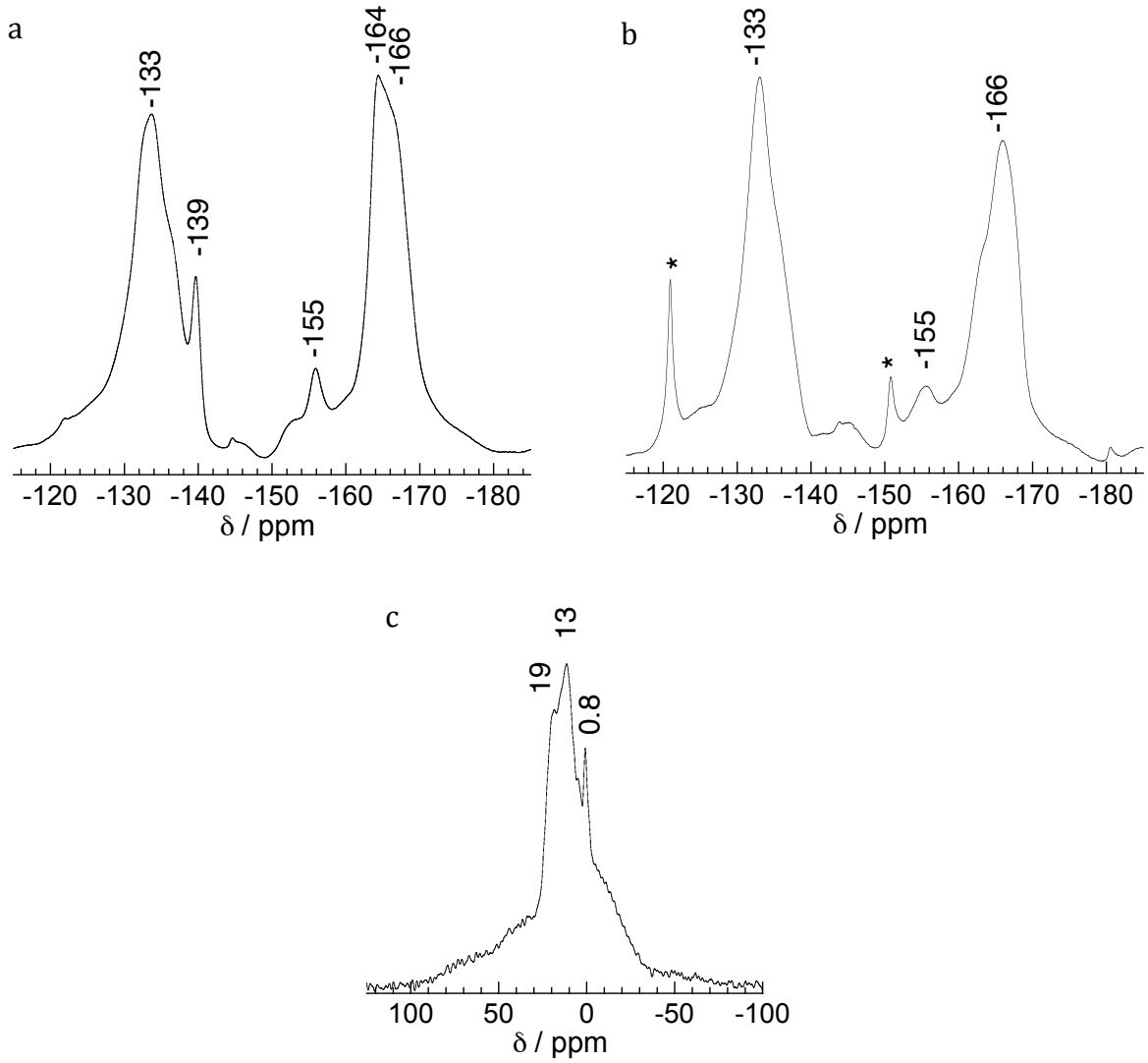

Figure 4.8. Solid-state MAS NMR of $B(C_6F_5)_2$-ADMS-$A380_{500}$, prepared at room temperature with stirring for 1 h: (a) ^{19}F (spin rate 14 kHz); (b) ^{19}F after washing in toluene; and (c) ^{11}B (spin rate 10 kHz) (* indicates spinning side-bands of Teflon o-ring).

The filtrate after hydroboration was analyzed by ^{19}F in attempt to understand the source of pentafluorobenzene. Starting material was seen in addition to peaks that are

consistent with the presence of $HOB(C_6F_5)_2$ and $[(C_6F_5)_2\ B]_2O$, see Table 4.1.[14] We did not detect any soluble pentafluorobenzene. The solid state ^{19}F NMR suggests this species is rather mobile and presumably physisorbed to the support and requires redissolving the support to remove.

Despite changing both the silane precursor and the silica, we obtained a complex mixture of products by ^{19}F and ^{11}B NMR. We thought by working at slightly elevated temperature we could drive the selectivity toward the desired product, Scheme 4.7. A third material was prepared using a procedure similar to that described above for $B(C_6F_5)_2$-ADMS-$A380_{500}$, except hydroboration was performed at 80 °C. This material is labeled $B(C_6F_5)_2$-ADMS-$A380_{500}$(80 °C).

Similar to $B(C_6F_5)_2$-ADMS-$A380_{500}$, the IR spectra of $B(C_6F_5)_2$-ADMS-$A380_{500}$(80 °C) confirms the presence of the borane, Fig. 4.9. Subtle differences between the two materials are visible in the υ(O–H) region and in the 1500 - 1300 cm^{-1} region after hydroboration; however, the materials seem to be essentially the same as $B(C_6F_5)_2$-ADMS-$A380_{500}$, with the same characteristic peak at 1472 cm^{-1} upon incorporation of the borane. Based on the IR spectra, we believe that the grafting reaction and subsequent hydroboration occur according to the Schemes shown above.

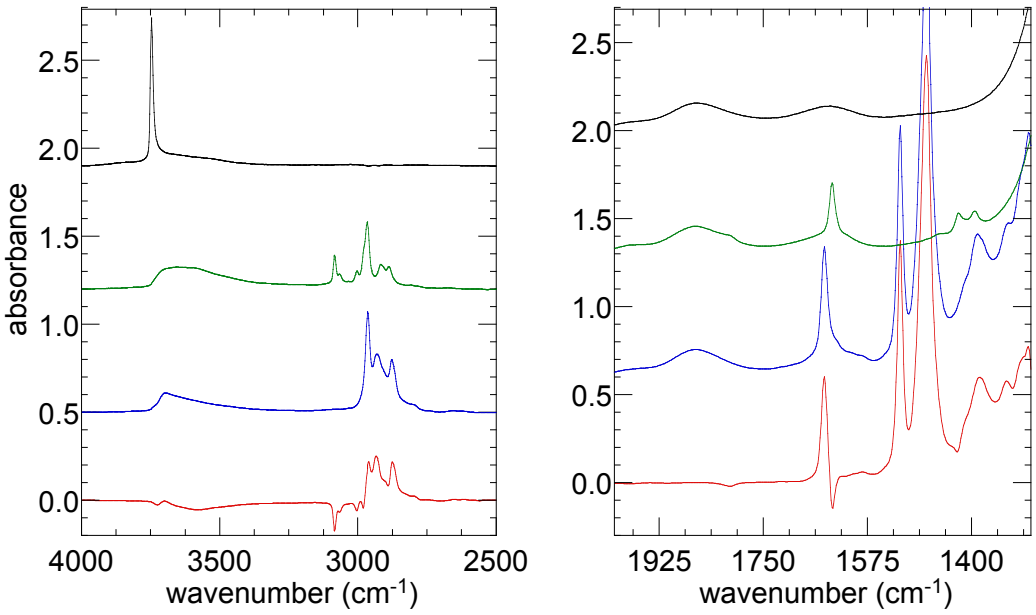

Figure 4.9. Transmission IR spectra of $A380_{500}$ (black), after allyldimethylsilyl modification (green), and after hydroboration with $HB(C_6F_5)_2$ to give $B(C_6F_5)_2$-ADMS-$A380_{500}$(80 °C) (blue). The difference spectrum, before and after the hydroboration reaction, is shown in red.

Similar to the previous materials, the ^{19}F MAS NMR spectrum of $B(C_6F_5)_2$-ADMS-$A380_{500}$(80 °C) shows two sets of three signals, Fig. 4.10a, however, the sharp set of resonances at -139 (*o*-F), -155 (*p*-F), and -163 (*m*-F) ppm, for pentafluorobenzene are much more intense. Presumably, formation of this product is accelerated at the higher temperature. Upon washing, these peaks can be removed leaving two broad resonances at -133 and -166 ppm (*o*-F and *m*-F, respectively), Fig. 4.10b. The *p*-F signal is located at -155 ppm. Based on the ^{19}F spectrum, this material appears to be structurally equivalent to $B(C_6F_5)_2$-ADMS-$A380_{500}$.

Figure 4.10c shows the solid-state ^{11}B MAS NMR spectrum, which consists of an intense peak at 12 ppm and a shoulder at 19 ppm. As observed in $B(C_6F_5)_2$-ADMS-$A380_{500}$, the relative position of the ^{11}B peak suggests boron may be four-coordinate.

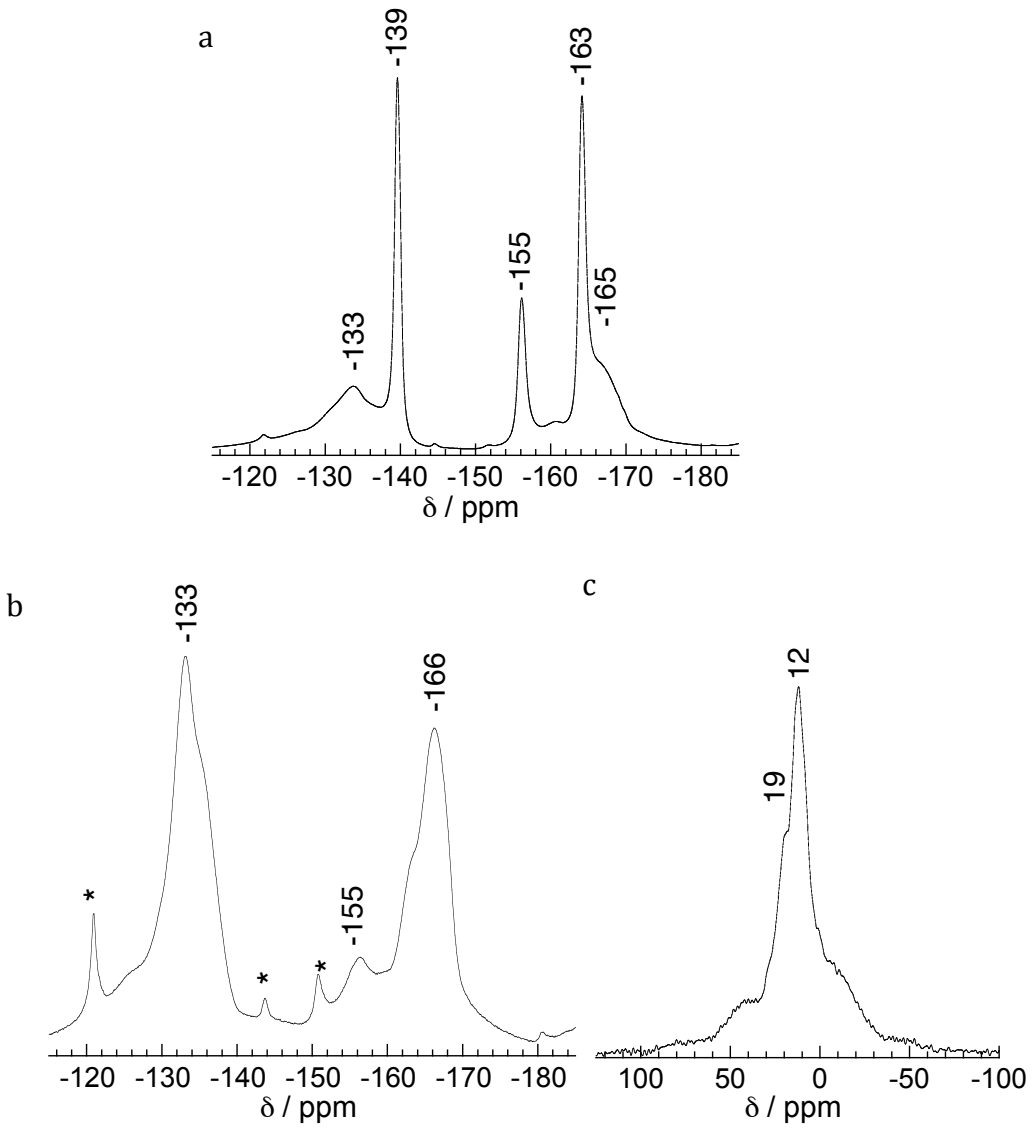

Figure 4.10. Solid-state MAS NMR of $B(C_6F_5)_2$-ADMS-$A380_{500}$(80 °C): (a) ^{19}F (spin rate 14 kHz); (b) ^{19}F (spin rate 14 kHz) after washing in toluene and (c) ^{11}B spectra (spin rate 10 kHz) (* indicates spinning side-bands of Teflon o-ring).

.

The ^{19}F chemical shifts for all three materials are summarized in Table 4.1. Overall, the major boron species in each material seem to be quite similar, regardless of the support and synthesis conditions. The ^{19}F spectra of $B(C_6F_5)_2$-ADMS-$A380_{500}$ and $B(C_6F_5)_2$-ADMS-$A380_{500}$(80 °C) do not resemble that of $B(C_6F_5)_2(CH_2)_3Si(CH_3)_2Cl$ (**2**), rather seem to be more like $B(C_6F_5)_2(CH_2)_3Si(OCH_2CH_3)_3$ (**1**).

Table 4.1. Solid-state ^{19}F NMR chemical shifts (δ, ppm) for borane-modified silicas and molecular analogs[a]

Material	*o*-F	*p*-F	*m*-F
$B(C_6F_5)_2$-AMES-$A380_{200}$	-134	-152	-166
$B(C_6F_5)_2$-ADMS-$A380_{500}$	-133	-155	-166
$B(C_6F_5)_2$-ADMS-$A380_{500}$(80 °C)	-133	-155	-166
$B(C_6F_5)_2(CH_2)_3Si(CH_3)_2Cl$ (**2**)	-130.6	-140.2	-161.0
$B(C_6F_5)_2(CH_2)_3Si(OCH_2CH_3)_3$ (**1**)	-133.1	-158.7	-164.7
$HB(C_6F_5)_2$[b]	-132.7	-148.6	-160.0
$(C_6F_5)_2BOH$[c]	-133.1	-148.3	-161.4
$[(C_6F_5)_2B]_2O$[c]	-132.6	-144.3	-160.2
$(C_6F_5)H$[c]	-139.2	-154.3	-162.5

[a] All spectra were recorded in toluene-d_8, except where noted.

[b] Recorded in CD_2Cl_2.

[c] Chemical shifts from ref. 14.

We were unable to conclusively state the structure of the silica-supported propyl bis(pentafluorophenyl)borane with ^{19}F and ^{11}B NMR. ^{13}C and ^{29}Si MAS NMR were also used to probe the grafting and hydroboration reactions of $B(C_6F_5)_2$-ADMS-$A380_{500}$(80 °C). Anchored allyldimethylsilyl groups in ADMS-$A380_{500}$ are evident in the ^{13}C CP/MAS NMR, via vinylic signals at 113 and 132 ppm, the methylene at 25 ppm and the methyl groups at -3 ppm, Fig 4.11a. The ^{29}Si CP/MAS NMR shows a signal for a monofunctional siloxy unit (M) at 12 ppm, Fig. 4.11b. The peaks at -100 and -107 ppm correspond to Q^3 (residual silanols) and Q^4 (siloxane) sites, respectively.

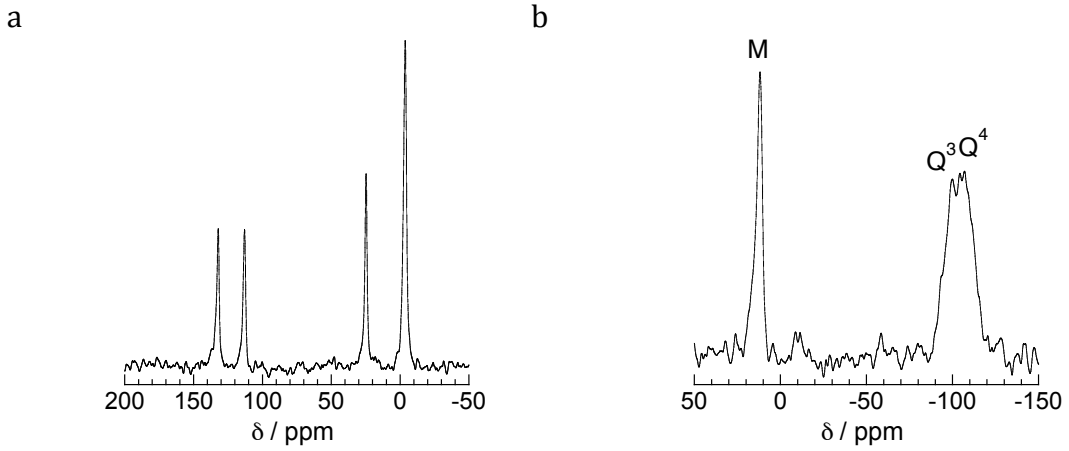

Figure 4.11. Solid-state NMR for ADMS-$A380_{500}$: (a) ^{13}C CP/MAS; and b) ^{29}Si CP/MAS spectra (spin rate 10 kHz).

After hydroboration, the two signals characteristic of the vinylic carbons disappear completely, Fig 4.12a. New signals appear between 10-30 ppm for the saturated propyl tether. In the ^{29}Si CP/MAS NMR, the monofunctional silicon (M) signal shifts slightly, from 12 to 15 ppm, Fig. 4.12b, while the Q^3 and Q^4 signals remain essentially unchanged. The ^{13}C and ^{29}Si CP/MAS NMR spectra confirm that the hydroboration reactions were successful.

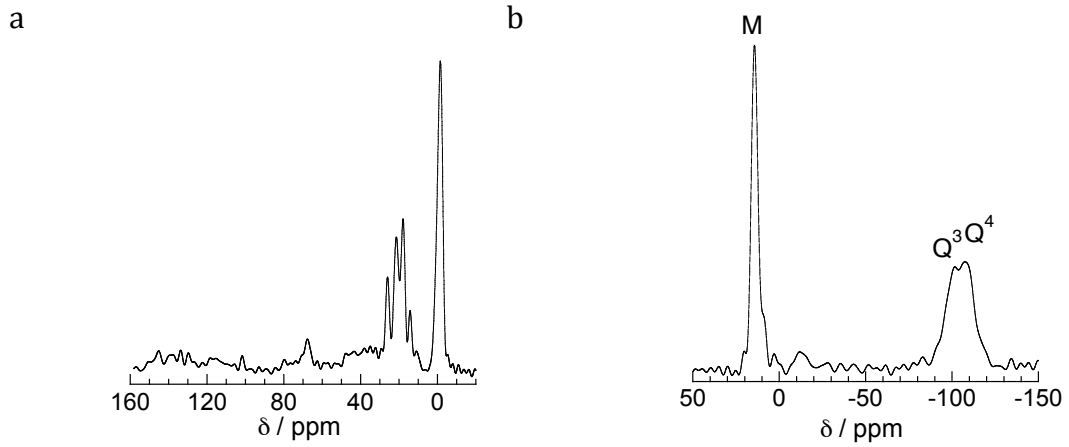

Figure 4.12. Solid-state NMR for $B(C_6F_5)_2$-ADMS-$A380_{500}$(80 °C): (a) ^{13}C CP/MAS; and (b) ^{29}Si CP/MAS spectra (spin rate 10 kHz).

Elemental analysis of the materials shows an average B content of 0.4 % and the C content of approximately 5 wt %. These values correspond to a B to C ratio of roughly 1:11, which is consistent with the loss of a $–C_6F_5$ ring. Although no evidence for water was present in the synthesis, we saw $HOB(C_6F_5)_2$ and $[(C_6F_5)_2\ B]_2O$ in the filtrate following the hydroboration reactions. Soluble pentafluorophenylbenzene was not observed in solution however, the solid-state MAS ^{19}F MAS shows it is clearly present on the silica surface. These materials are extremely sensitive to hydrolysis and undergo changes during storage probably due to adventitious water. The presence of water could lead to the formation of a B-OH species with concomitant formation of pentafluorobenzene.

4.4 Conclusions

Two silylpropyl bis(pentafluorophenyl)boranes were synthesized as molecular models for the Lewis acid component of supported frustrated Lewis pairs. We found **1** exhibits a B-O interaction with an ethoxysilyl group. Complex **2**, containing no oxygen atoms, lacks these interactions. Three types of supported propyl bis(pentafluorophenyl)boranes, were prepared using a two-step methodology. First, allyl propylsilanes were installed, followed by hydroboration using Piers' borane to give tethered Lewis acid sites. Attempts to synthesize three-coordinate silica-suppported propyl bis(pentafluorophenyl)boranes were thwarted by an unexpected side-reaction leading to a mixture of products including pentafluorobenzene. Preserving the structure of the catalyst is not only difficult during synthesis but also in prolonged storage of the material. In these lengthy syntheses, it is not often practical to make new material every time a reaction is tested. Proper storage of these sensitive materials in sealed ampules or at low temperature can prevent changes, likely due to adventitious water.

4.5 References

1. Welch, G. C.; Juan, R. R. S.; Masuda, J. D.; Stephan, D. W., *Science* **2006,** *314*, 1124-11126.

2. Ashley, A. E.; Thompson, A. L.; O'Hare, D., *Angew. Chem. Int. Ed.* **2009,** *48*, 9839-9843.

3. Stephan, D. W.; Erker, G., *Angew. Chem. Int. Ed.* **2010,** *49*, 46-76.

4. Mömming, C. M.; Otten, E.; Kehr, G.; Fröhlich, R.; Grimme, S.; Stephan, D. W.; Erker, G., *Angew. Chem. Int. Ed.* **2009,** *48*, 6643-6646.

5. Neu, R. C.; Ménard, G.; Stephan, D. W., *Dalton Trans.* **2012,** *41*, 9016-9018.

6. Erker, G., *Dalton Trans.* **2011,** *40*, 7475-7483.

7. Rice, G. L.; Scott, S. L., *Langmuir* **1997,** *13*, 1545-1551.

8. Nöth, H.; Wrackmeyer, B., *NMR Spectroscopy of Boron Compounds*. Springer-Verlag: Berlin Heidelberg, 1978; Vol. 14.

9. Horton, A. D.; de With, J., *Organometallics* **1997,** *16*, 5424.

10. Parks, D. J.; Blackwell, J. M.; Piers, W. E., *J. Org. Chem.* **2000,** *65*, 3090-3098.

11. Crisci, A. J.; Tucker, M. H.; Dumesic, J. A.; Scott, S. L., *Topics in Catal.* **2010,** *53*, 1185-1192.

12. Marrone, M.; Montanari, T.; Busca, G.; Conzatti, L.; Costa, G.; Castellano, M.; Turturro, A., *J. Phys. Chem. B* **2004,** *108*, 3563-3572.

13. Wanglee, Y.-J.; Hu, J. G.; White, R. H.; Lee, M. Y.; Stewart, S. M.; Perrotin, P.; Scott, S. L., *J. Am. Chem. Soc.* **2012,** *134*, 355-366.

14. Tian, J.; Wang, S.; Feng, Y.; Li, J.; Collins, S., *J. Mol. Catal. A* **1999,** *144*, 137-150.

Appendix I.

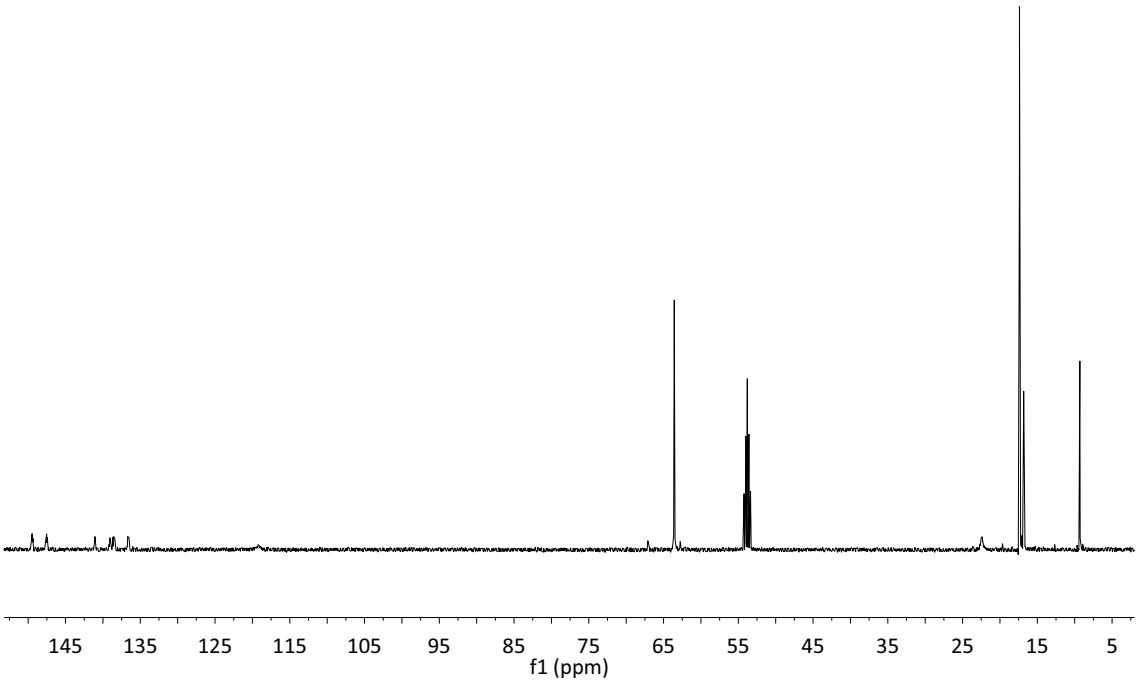

Figure A1.1. $^{13}C\{^{1}H\}$ NMR of **1** (125 MHz, 299 K, CD_2Cl_2).

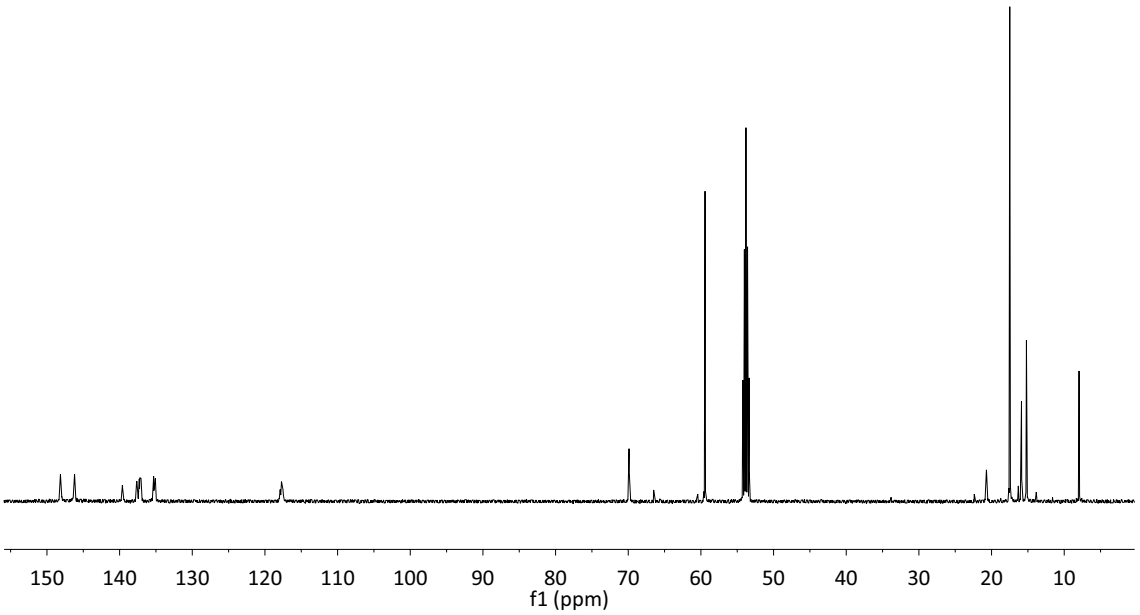

Figure A1.2. $^{13}C\{^{1}H\}$ NMR of **1** (125 MHz, 188 K, CD_2Cl_2).

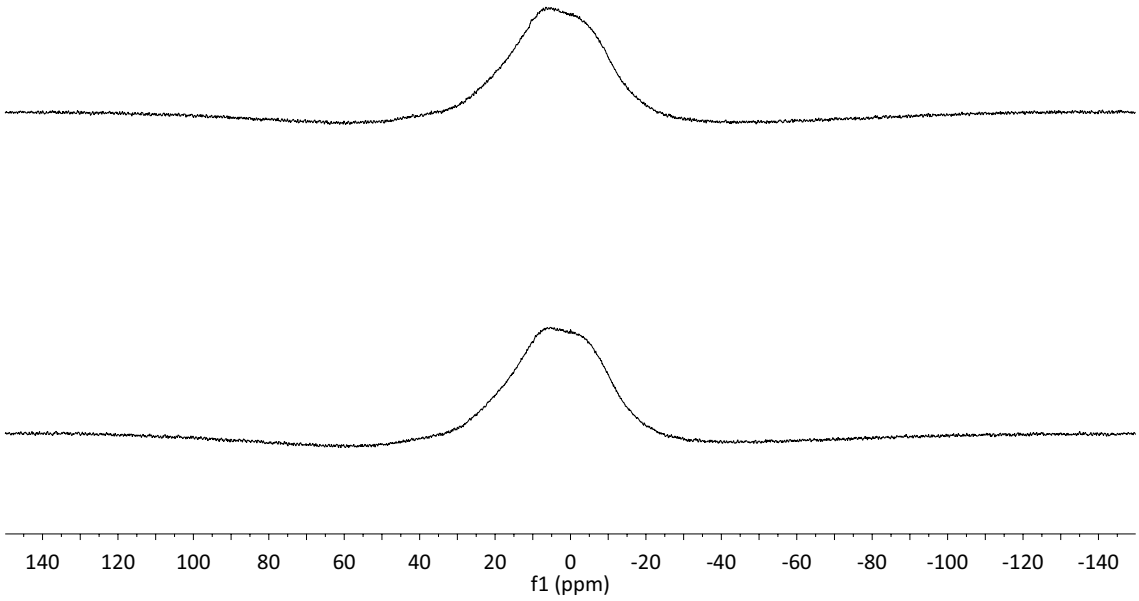

Figure A1.3. $^{11}B\{^{1}H\}$ (top) and ^{11}B NMR (bottom) of **1** (64 MHz, 188 K, CD_2Cl_2).

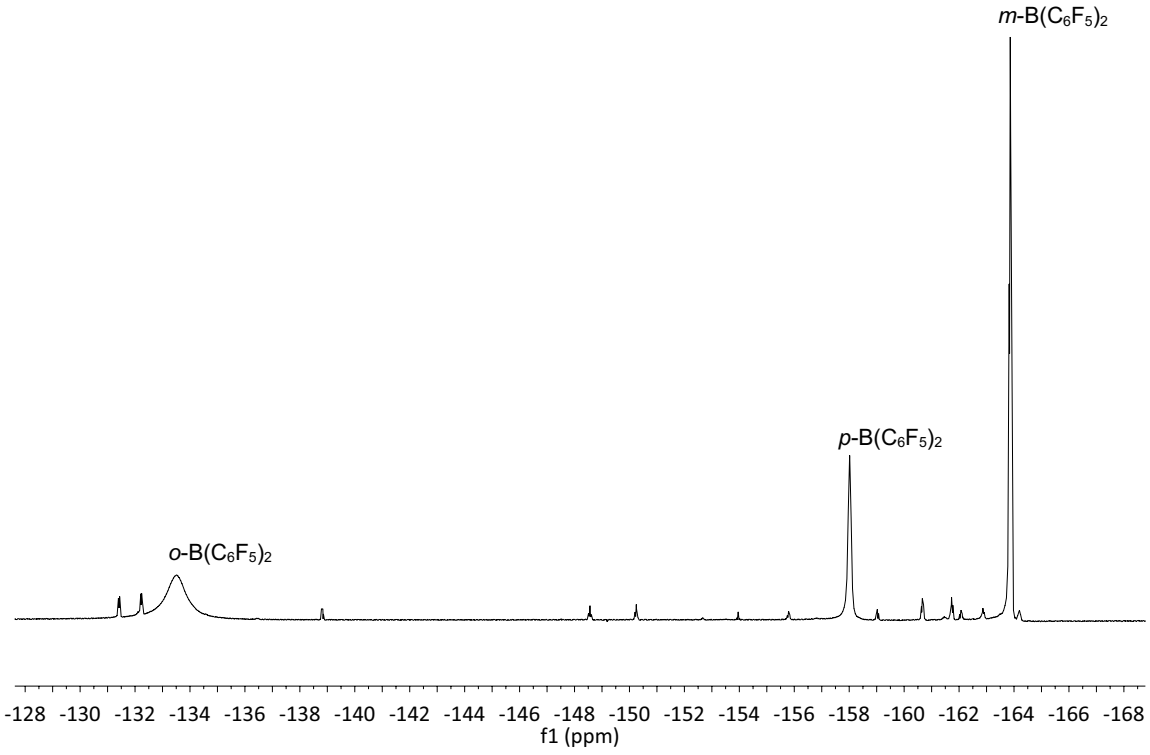

Figure A1.4. ^{19}F NMR of **1** (282 MHz, 188 K, CD_2Cl_2).

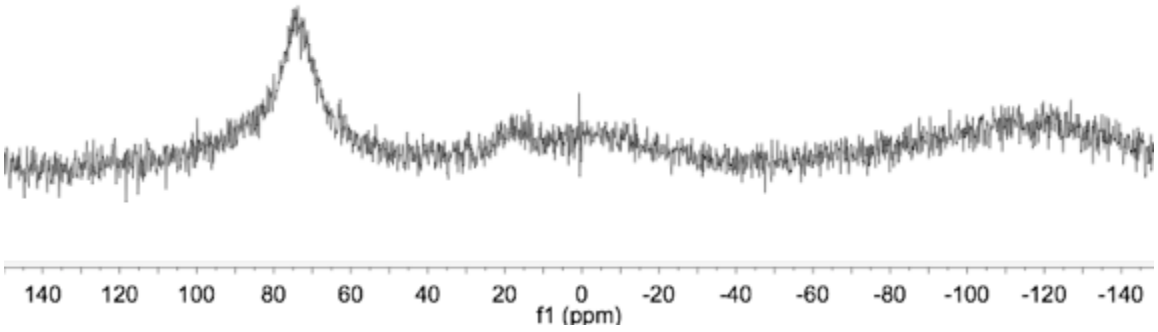

Figure A1.5. ^{11}B NMR of **2** (25.6 MHz, 299 K, C_6D_6).

Chapter 5: Redox reactions of Cp*Ir Complexes Supported on Periodic Mesoporous Organosilicas

5.1. Introduction

Carboxylic acids are important organic compounds, utilized in a wide variety of consumer products. They serve as synthetic precursors to esters, amides, and polymers. Production of carboxylic acids from aldehydes can be achieved using a variety of oxidants, such as permanganate, hydrogen peroxide, and oxygen.[1] Aldehyde disproportionation, in which the aldehyde itself serves as the oxidant, is also well-established. In the Cannizzaro reaction, an aldehyde bearing no α-hydrogens undergoes disproportionation under basic conditions to afford a carboxylate salt and a primary alcohol (Scheme 5.1).[1]

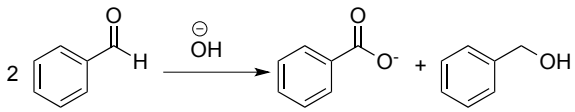

Scheme 5.1. The Cannizzaro reaction is the base-induced disproportionation of an aldehyde to the corresponding carboxylate and aldehyde.

An alternative for generating carboxylic acids from aldehydes is the "aldehyde–water shift" (AWS) reaction. It is analogous to the well-studied water–gas shift reaction (Scheme 5.2), in which water serves as the terminal oxidant. Using this strategy, aldehydes may be oxidized in an atom-economical route under mild conditions, while also liberating H_2 as a valuable by-product.

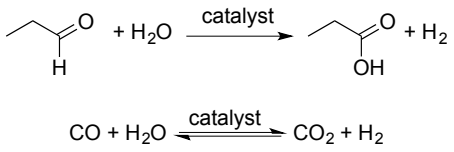

Scheme 5.2. Comparison of "aldehyde-water shift" with the well-known, analogous water-gas shift reaction.

The AWS reaction was named in 2004 by Stanley and coworkers,[2] who observed it as a side-reaction during Rh-catalyzed hydroformylation. However, Murahashi et al. had already identified the reaction in 1987, as part of a larger study of Ru-catalyzed conversion of alcohols and aldehydes to esters and lactones.[3] The AWS reaction may also play a role in the dehydrogenation of primary alcohols. Grützmacher[4] and Milstein[5] reported a more general reaction in which a wide range of primary alcohols are oxidized by H_2O to the corresponding carboxylates in the presence of a base.

Recently, Brewster et al. reported a series of di- and monocationic Ru, Rh, and Ir complexes that were tested for catalytic activity in the AWS reaction, Fig. 5.1, using propionaldehyde as the substrate and water as both oxidant and solvent (4 mM catalyst, 500 mM substrate, H_2O, 105 °C, 18 h).[6] For many of the catalysts tested, propionic acid was present as approximately 50% of the converted product, indicating that disproportionation is more favorable than AWS. Catalyst precursors consisting of Ir and Rh with bipyridyl and phenylpyridyl ligands are the most active, displaying near quantitative conversion of propionaldehyde. However, Ir(ppy) and Ru(bpy) demonstrated greater selectivity towards AWS.

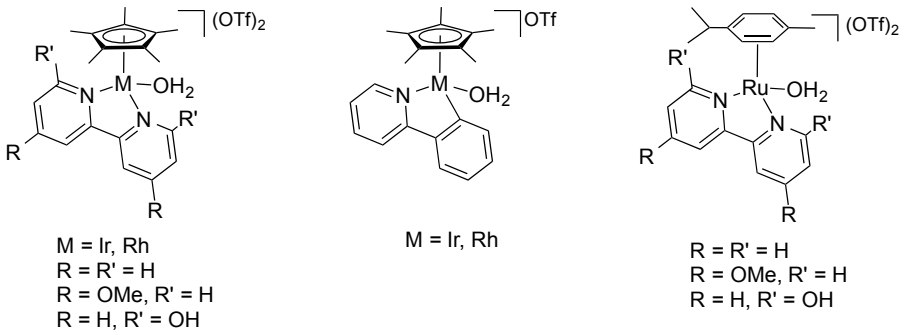

Figure 5.1. Catalysts screened for the AWS reaction. Complexes are named by the metal and the pyridyl ligand, i.e., $[Cp^*Ir(bpy)OH_2][OTf]_2$ = Ir(bpy).[6]

While the AWS reaction was proposed to occur at a single metal center, oxidations catalyzed by molecular iridium compounds can be complicated by the high activity of iridium oxides, which can be formed in situ from the organometallic precursor.[7-10] Catalyst decomposition may have occurred without detection of finely dispersed metal oxide to the naked eye. Supporting the catalyst could allow the possibility to operate at the reaction at higher temperatures if the decomposition pathways are mononuclear, which is likely based on the homogeneous study, and would allow for reuse. Here we describe new silica-supported half-sandwich metal complexes modeled after the molecular AWS catalysts. Specifically, we developed immobilized phenylpyridyl and bipyridyl ligands for Ir. A periodic mesoporous organosilica (PMO) was chosen as the catalyst support because of its excellent chemical and thermal stability, high porosity, and large surface area. PMOs have shown to have improved hydrothermal stability related to the more hydrophobic environment induced inside the pore channels, due to the presence of ethylene groups in the walls.[11-13] The

silica-supported complexes were characterized in detail to elucidate their structures using NMR and IR spectroscopies, N_2 physisorption, and elemental analysis. The reactivity of the materials were also tested

5.2 Experimental Section

5.2.1 Reagents and Materials

Tetramethyl orthosilicate (TMOS, 98%), 1,2-*bis*(triethoxysilyl)ethane (BTEB, 96%) and *bis*(trimethoxysilyl)ethane (BTME, 96%) were purchased from Aldrich and used as received. 2-[2-[2-(trimethoxysilyl)ethyl]phenyl]pyridine (ppy-silane) and 2-(2-pyridyl)-(3-[2-(trimethoxysilyl)ethyl]pyridine (bpy-silane) were prepared according to a literature procedure (see Appendix II). Pluronic P123 was purchased from BASF. NaCl (Certified ACS Crystalline) was obtained from Fisher Scientific. Ethanol (200 proof, Gold Shield) was used as received. $[Cp^*IrOH_3][OTf]_2$ was prepared according to a literature procedure.[14] The supported versions of these catalysts were dried under vacuum (0.1 mTorr) at 423 K for 15 h. All dry materials were stored in an argon-filled glove box to prevent readsorption of atmospheric moisture.

5.2.2. Characterization

Solid-state NMR spectra were recorded on a Bruker DSX500 WB spectrometer operating at 12.0 T, with frequencies of 125 and 99 MHz for ^{13}C and ^{29}Si, respectively. Samples were packed under argon into 4-mm zirconia rotors (Bruker). ^{29}Si magic angle spinning (MAS) and cross-polarization/magic angle spinning (CP/MAS) spectra were

obtained using a 90° pulse length of 2.5 ms, a contact time of 5 ms, and high-power proton decoupling during detection. Typically, 25 000 scans were acquired at a spinning rate of 10 kHz. Chemical shifts were referenced using tetrakis(trimethylsilyl)silane (Aldrich). ^{13}C CP/MAS spectra were obtained using a 90° pulse length of 2.4 ms, a contact time of 2 ms, and high-power proton decoupling during detection. Typically, 25 000 scans were acquired at a spinning rate of 10 kHz. Chemical shifts were referenced using tetrakis(trimethylsilyl)silane (Aldrich).

IR spectra were recorded under Ar in diffuse reflectance (DRIFT) mode on a Bruker ALPHA spectrometer. For background and sample spectra, 32 spectra were recorded at a resolution of 4 cm^{-1}. Self-supporting pellets of silica were made by pressing 3-5 mg sample into disks of 4 mm diameter using a hand press. N_2 adsorption/desorption measurements were performed on a Micromeritics Tristar 3000 Porosimeter. TEM images were collected on an FEI Tecnai G2 Sphera Microscope. An Oxford electron dispersive X-ray spectroscopy (EDS) system is attached for chemical analysis, and a Gatan UltraScan 1000P CCD camera for image recording. Metal contents were determined using an inductively-coupled plasma atomic emission spectrometer (Thermo iCAP 6300). The standard solutions (Rh Standard for ICP TraceCERT, 1000 mg/L Rh in HCl, Aldrich, and Ir Standard, 1000 mg/mL in water with dilute HCl, Ultra Scientific) were diluted to the desired concentration with dilute HNO_3, for use in elemental analysis. The silica samples were digested with HF/HNO_3 and the liquid was evaporated. The residue was dissolved in dilute HNO_3, as in preparation of the standards.

5.2.3 Synthesis of Phenylpyridyl-Functionalized PMO (ppy-PMO)

Following a modified literature procedure,[15] Pluronic P123 (1.91 g) was dissolved with stirring in 1.60 M aqueous HCl (70 mL), then heated to 318 K in a tightly sealed HDPE bottle (200 mL) in an oil bath. TMOS (1.38 mL, 9.62 mmol) and BTEB (2.42 mL, 9.36 mmol) were added, followed 15 min later by NaCl (0.426 g). After a further 15 min, 2-[2-[2-(trimethoxysilyl)ethyl]phenyl]pyridine (ppy-silane) was added (660 mg) (ppy-silane should represents ca. 11 % of the Si in the PMO framework). After 24 h, the reaction mixture was removed from the oil bath and transferred to a 125 mL Parr pressure reactor equipped with a Teflon liner. The reactor was placed in an oven at 378 K for 24 h. The resulting suspension was filtered, and washed with ca. 200 mL water. The surfactant was removed by ethanol extraction: the solid was suspended in 500 mL acidified ethanol (containing 2 M HCl) and refluxed for 24 h, then filtered and washed with ca. 200 mL ethanol. The ethanol extraction was performed three times. The resulting solid was suspended in a buffer solution of pH 7 (100 mL 0.1 M KH_2PO_4, 58.2 mL 0.1 M NaOH) for 5 h with vigorous stirring. The suspension was then filtered and washed with 350 mL water. The silica was collected and suspended in 150 mL water and stirred overnight. The suspension was filtered again, washed with water and the solid was dried in the oven overnight at 373 K followed by an additional drying step under vacuum at 388 K. Elemental analysis: 24.1 % C, 4.2 % H, 1.4 % N. Expected: 1.8 % N.

5.2.4 Synthesis of Bipyridyl-Functionalized PMO (bpy-PMO)

Bpy-PMO was prepared in a manner similar to that described above for ppy-PMO, but instead of ppy-silane, 2-(2-pyridyl)-(3-[2-(trimethoxysilyl)ethyl]pyridine (bpy-silane) and

BTME were added in the co-condensation reaction (bpy-silane should represents ca. 11 % of the Si in the PMO framework). Elemental analysis: 21.8 % C, 3.4 % H, 1.9 % N. Expected: 3.2 % N.

5.2.5 Metallation of ppy-PMO

Metallation was carried out using a modified literature procedure.[16] In a 35 mL reactor with a Teflon screw cap, ppy-PMO, NaOAc and $[Cp^*Ir(OH_2)_3][OTf]_2$ (1:1.8 ppy to metal ratio) were suspended in CH_2Cl_2 (20 mL). The suspension was vigorously stirred overnight at room temperature. The solid was isolated by filtration, washed with CH_2Cl_2 (3 x 100 mL) and dried at 110 °C under vacuum (0.1 mTorr) for 18 h. To remove NaOAc, the silica was suspended in CH_2Cl_2 (20 mL) and stirred for 24 h at room temperature. Despite multiple attempts, ^{13}C NMR signals at 182 and 24 ppm attributed to residual acetate remained in the NMR spectrum. The solid was isolated by filtration, washed with CH_2Cl_2 (3 x 100 mL) and dried at 110 °C under vacuum (0.1 mTorr) for 18 h. Elemental analysis: 4.8 wt% Ir; expected 10.1 wt% Ir.

5.2.6 Metalation of bpy-PMO

The metalation reaction on bpy-PMO was carried out with $[Cp^*Ir(OH_2)_3][OTf]_2$ using a literature procedure.[17] The workup was similar to that used for ppy-PMO. Elemental analysis: 1.5 % Ir; expected 2.6 wt% Ir.

5.2.7 Catalytic Oxidation of Propionaldehyde

In a typical reaction, approx. 20 mg catalyst (0.5 mM) was added to a 15 mL Teflon screw-cap reactor with a side-arm adapter. In a separate vial, the aldehyde substrate (30 mM, 60 equiv.) and internal standard (phenol) were dissolved in H_2O (10 mL). A small aliquot was removed for ^1H NMR analysis in D_2O, and the remaining solution was added to the catalyst solution under flowing N_2. The reactor was sealed and heated in an oil bath to 378 K while stirring vigorously. After 18 h, the reactor was removed from the heat and stirring was stopped. The suspension was centrifuged and the supernatant sampled for ^1H NMR analysis in D_2O. Substrate conversion was determined by integration, using the internal standard.

5.2.8 Catalytic Hydrogenation of Levulinic Acid

In a typical reaction, levulinic acid (1 mmol) and approx. 100 mg catalyst (0.025 mmol) were combined in THF (2 mL). The reactor was sealed, charged with 50 bar H_2 and heated in an oil bath to 393 K while stirring vigorously. After 40 h, the reactor was removed from the heat, stirring was stopped and the reactor was vented. The suspension was filtered and the supernatant sampled for ^1H NMR analysis in CD_2Cl_2.

5.3 Results and Discussion

5.3.1 Synthesis and Characterization of Phenylpyridyl-Functionalized Silica (ppy-PMO)

Previous syntheses of phenylpyridyl- or bipyridyl-functionalized silicas generally involved multistep grafting procedures. One strategy is to co-condense a readily available silane, such as chloropropyltriethoxysilane, then tether a modified bipyridyl ligand/complex.

A second approach involves direct grafting of a pre-made bipyridylsilane onto a silica support.[18-22] Additional methods of incorporating bpy complexes onto substrates include physical adsorption,[23] ion exchange,[24] and encapsulation,[25] in addition to other techniques.[26-30]

Synthesis of ordered mesoporous silicas with ppy or bpy ligands incorporated within the framework is limited by the availability of appropriate silanes for co-condensation, or lengthy synthesis procedures to obtain these silanes. Recently, Inagaki et al. prepared PMOs containing ppy or bpy ligands within the framework by condensation of a newly synthesized organodisilane precursor [(*i*-PrO)$_3$Si–R–Si(O*i*-Pr)$_3$] (R = $C_{10}H_6N_2$ or $C_{11}H_7N$), without addition of any other silanes.[31, 32] However, incorporating the ligand directly into the silica framework in this way may severely limit the mobility of the metal complex, impacting its reactivity. Here, we report a PMO material prepared by co-condensing a ppy- or bpy-silane into a silica framework. This method provides a robust linkage, while maintaining more solution-like behavior by incorporating a flexible tether.

The ppy-PMO was synthesized by template co-condensation of 2-[2-[2-(trimethoxysilyl)ethyl]phenyl]pyridine (ppy-silane) with 1,2-bis(triethoxysilyl)ethane (BTEB) and tetraethyl orthosilicate (TEOS), Scheme 5.3. Approx. 11 % of the Si in the synthesis mixture should be derived from ppy-silane, according to this synthesis procedure. However, elemental analysis shows that only 4.8 mol % of the initial silane is incorporated in the silica framework, likely due to steric interferences during silica condensation from incorporating the bulky organosilane.

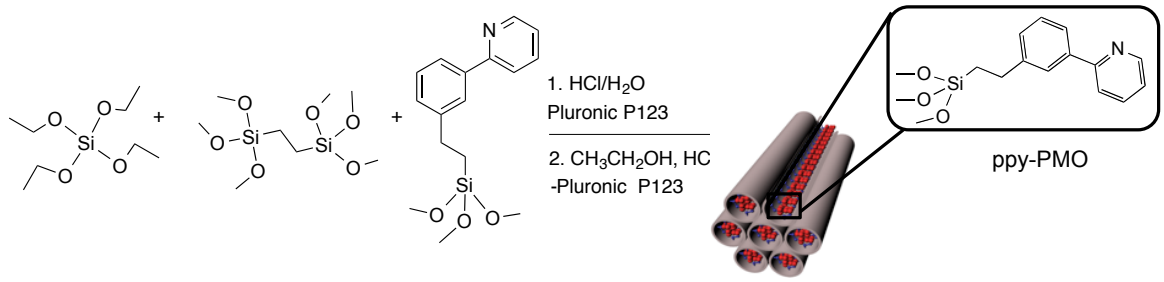

Scheme 5.3. Synthesis of ppy-PMO via co-condensation of TEOS, BTME and ppy-silane.

The characterization of ppy-PMO is consistent with literature reports for similar materials. In the ^{13}C CP/MAS spectrum, signals for the aromatic rings between 124-160 ppm are consistent with the pattern observed for the free ligand (Fig. 5.2a). Signals characteristic of framework ethane, due to the condensation of BTME, appear at 5 ppm. The hydrolysis/condensation reaction produces ethanol as a by-product, which evidenced by ethoxy signals at 16 and 58 ppm. The ^{29}Si CP/MAS NMR spectrum shows peaks at -58 and -64 ppm, confirming BTME and presumably the ppy-silane are robustly anchored through either two or three siloxane bonds (T^2 and T^3 sites). The framework silicon atoms appear as Q^3 and Q^4 sites (-100 and -108 ppm, respectively), indicating near-complete condensation (Fig. 5.2b). These results indicate that Si-C bonds and the ppy moiety remain intact during synthesis and extraction.

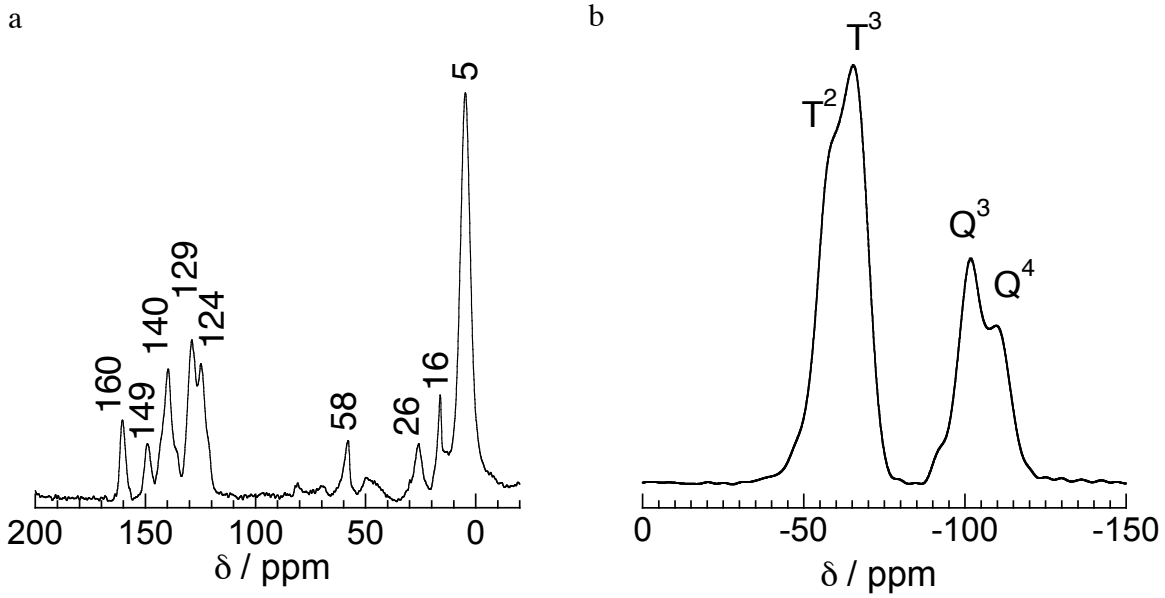

Figure 5.2. Solid-state NMR spectra for ppy-PMO: (a) ^{13}C CP/MAS; and (b) ^{29}Si CP/MAS. Spinning rate 10 kHz.

Nitrogen adsorption–desorption produced a type IV isotherm with H1-type hysteresis loops at high relative pressures, characteristic of capillary condensation within uniform pores (Fig. 5.3).[33] The B.E.T. surface area is 633 m^2/g, with B.J.H. pore diameter and volume of 5 nm and 0.64 cm^3/g, respectively. Co-condensation of the bulky ppy-silane into the porous silica framework maintains the integrity of the PMO material, as seen by the linear channels and hexagonally-arranged pores that are clearly visible by TEM (Fig. 5.4).

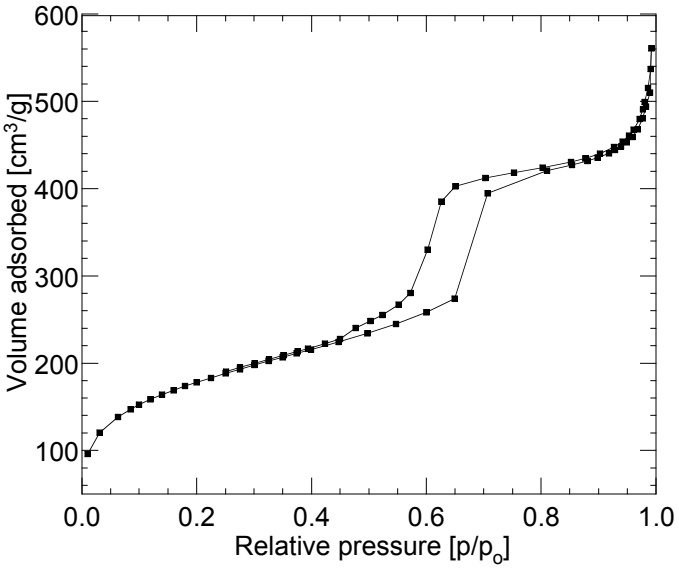

Figure 5.3. N_2 adsorption/desorption isotherms for ppy-PMO.

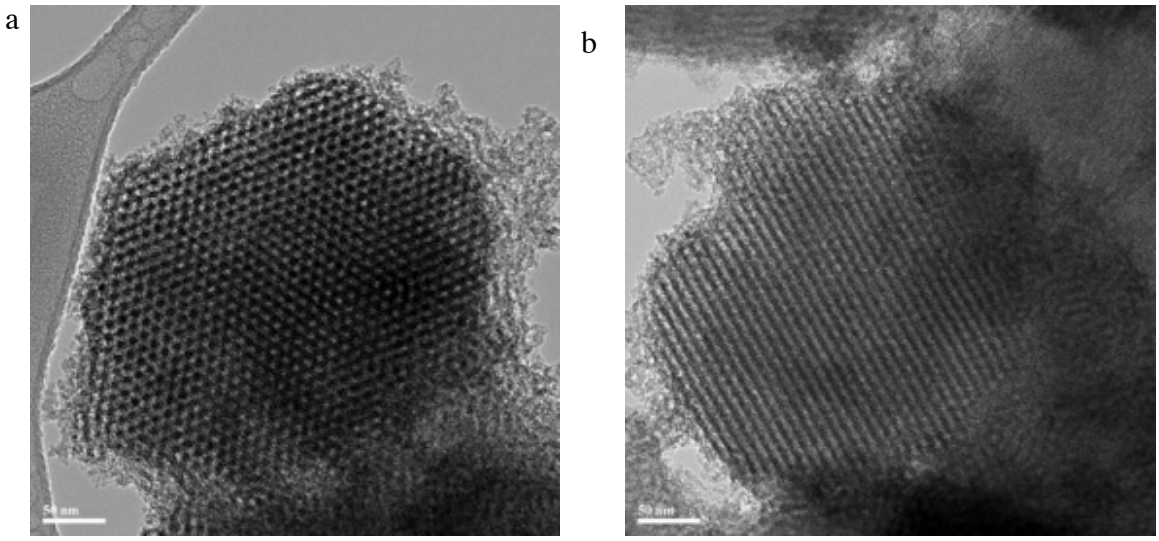

Figure 5.4. TEM images of ppy-PMO imaged at two different perspectives: (a) top view of hexagonal pores, and (b) side view of regularly-ordered porous channels.

5.3.2 Synthesis and Characterization of Bipyridyl-Functionalized Silica (bpy-PMO)

The bpy-PMO was synthesized and characterized using similar methods, by co-condensation with 2-(2-pyridyl)-(3-[2-(trimethoxysilyl)ethyl]pyridine (bpy-silane). Approx. 11 mol % of the Si in the synthesis mixture should be derived from bpy-silane, according to this synthesis procedure, however elemental analysis showed that only 6.5 mol % incorporation was achieved. The difference is again ascribed to … The signal for the ethane-bridged disilane, at 5 ppm, is the most prominent peak in the ^{13}C CP/MAS spectrum, appearing with signals at 16 and 60 ppm for residual ethoxy groups (Fig. 5.5). The aromatic peaks of the bipyridyl-functionalized silane appear between 120 and 160 ppm, consistent with the molecular analog. During workup, some of the P123 surfactant was not fully extracted, as shown by the small peaks at 60-80 ppm. Similar to ppy-PMO, the ^{29}Si CP/MAS NMR spectrum confirms that the BTME (and presumably the bpy-silane) are covalently anchored through either two or three siloxane bonds (T^2 and T^3 sites). TEM images of the material show well-defined pores as well as hexagonally ordered channels (Fig. 5.6). As with ppy-PMO, the bpy-silane appears to be intact following synthesis and workup of the material.

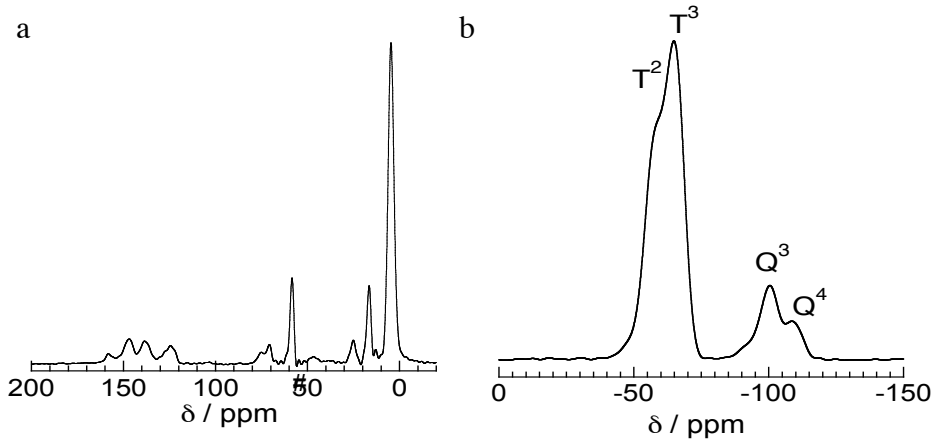

Figure 5.5. Solid-state NMR spectra for bpy-PMO: (a) ^{13}C CP/MAS; and (b) ^{29}Si CP/MAS. Spinning rate 10 kHz (# indicates residual surfactant).

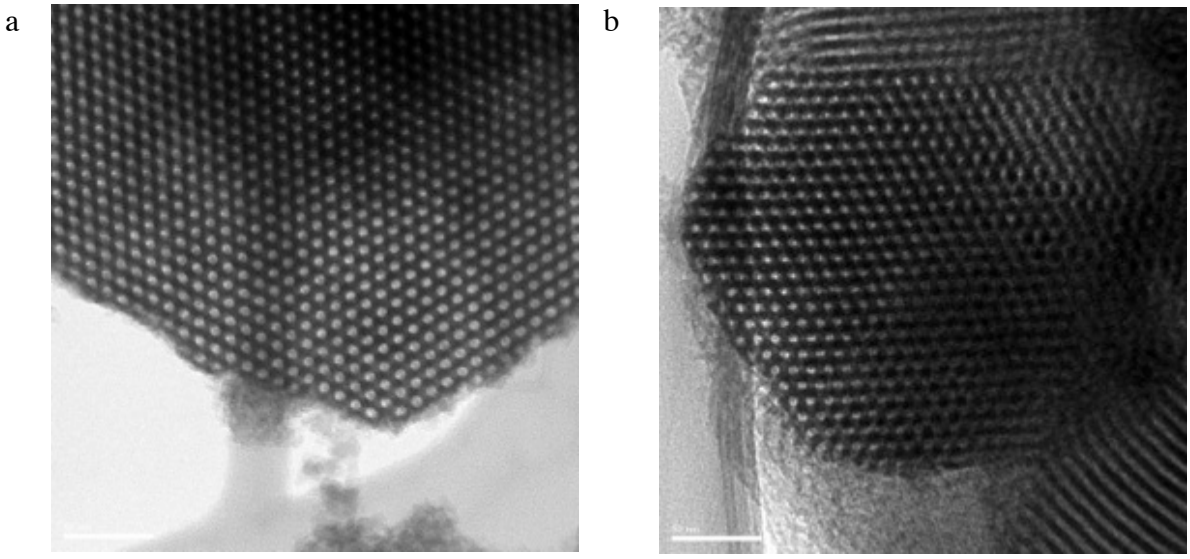

Figure 5.6. TEM images of bpy-PMO imaged at two different perspectives: (a) top view of hexagonally-ordered pores, and (b) side view showing regularly ordered porous channels (lower right corner).

*5.3.3 Synthesis and Characterization of Cp*M-ppy-PMO*

The reaction of $[Cp^*Ir(OH_2)_3^+](OTf^-)_2$ with ppy-PMO is expected to give the *C,N*-chelated complex, via initial coordination of the pyridine ring followed by ortho-metalation at the phenyl group (Scheme 5.4). Analogous reactions have been reported in solution.[16] The ppy-PMO, initially tan, evolves to a yellow color upon reaction with the Ir complex. The resulting solid has a metal content of 4.8 wt% Ir, compared to the expected value of 10.1 wt%. Although the synthesis procedure used a 2:1 ppy to metal ratio, the Ir:N ratio is approx. 1:3.8 (0.25 mmol Ir, 0.97 mmol ppy).

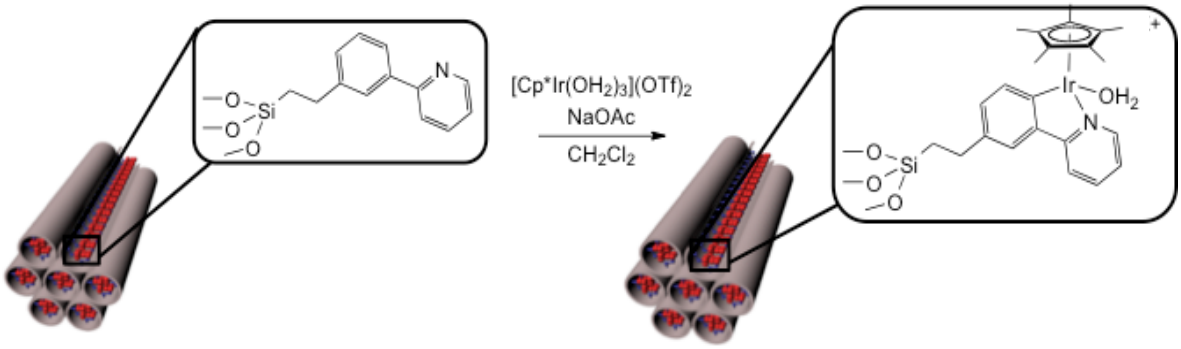

Scheme 5.4. Expected metalation of ppy-PMO with $[Cp^*Ir(OH_2)_3(OTf)_2]$ to give silica-supported Cp*Ir-ppy-PMO.

The ^{13}C CP/MAS NMR spectra of the tethered complex agrees well with that of the homogeneous analog. Peaks in the aromatic region (110-170 ppm) corresponding to the ppy group remain, as does the methylene peak of the BTME precursor at 5 ppm. A new signal at 9 ppm corresponds to the methyl groups of the Cp* ligands, while the quaternary carbon signal appears at 89 ppm. A third resonance at 168 ppm corresponds to the 2′ position of the

phenyl ring (*ipso* carbon directly bound to Ir), as observed in the molecular complex Cp*Ir(ppy),[16] Fig. 5.7. Sharp signals for NaOAc are also present, suggesting it cannot be removed by washing and is strongly adsorbed to silica and/or coordinated to Ir.

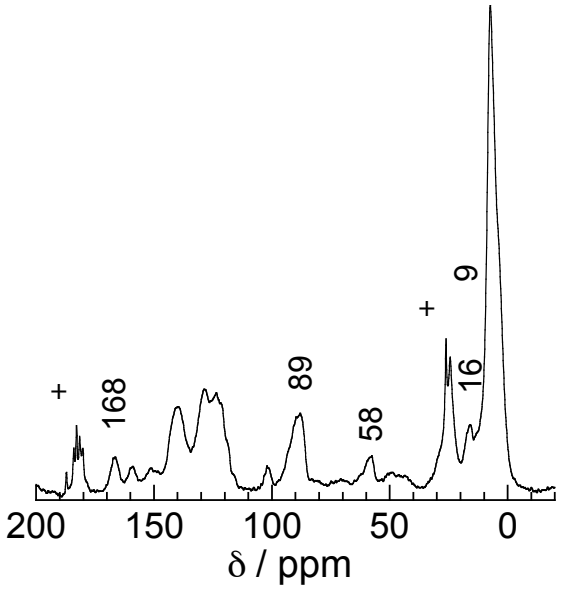

Figure 5.7. ^{13}C CP/MAS solid-state NMR spectrum for Cp*Ir-ppy-PMO (+ indicates residual -OAc).

Figure 5.8 displays DRIFT spectra of the ppy-PMO before and after reaction with $Cp^*Ir(OH_2)_3(OTf)_2$. The IR spectrum of ppy-PMO contains bands assignable to C=C and C=N aromatic ring modes of the ppy group and CH_2 bends of the propyl chain and BTME (1350–1650 cm^{-1}). A broad peak centered at 3670 cm^{-1} remains in the υ(O–H) region, representing silanol groups perturbed by hydrogen-bonding. A small band at 3730 cm^{-1} is attributed to isolated surface hydroxyls that remain due to incomplete silane condensation.

Little change occurs in this region upon reaction with $Cp^*Ir(OH_2)_3(OTf)_2$. The broad band at 3670 cm^{-1} remains, and an additional peak at 3470 cm^{-1} appears possibly from some interaction between acetate and hydroxyl groups. In the υ(C–H) region, several bands are visible between 3100 and 2800 cm^{-1}, corresponding to the C-H stretching modes of the propyl chain of the ppy-silane and the alkyl chain of the surfactant (due to incomplete extraction) as a minor component. After metalation, some features in this region are lost and new weak bands appear between 2600 and 2000 cm^{-1}, which may be overtones and/or combination bands associated to the Ir complex.

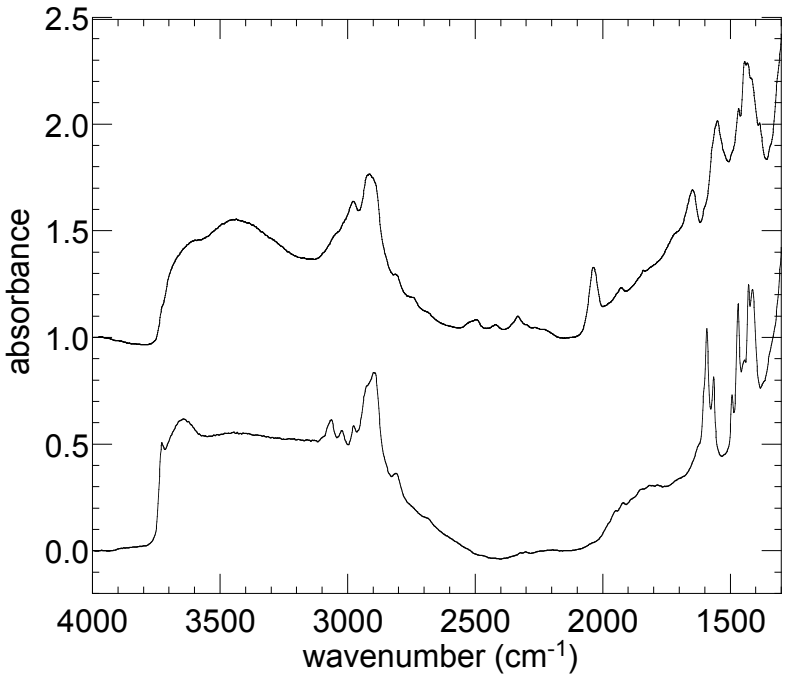

Figure 5.8. DRIFT spectra of ppy-PMO (bottom), Cp*Ir-ppy-PMO (top)

*5.3.4 Synthesis and Characterization of Cp*Ir-bpy-PMO*

According to literature precedent[17], reaction of $Cp^*Ir(OH_2)_3(OTf)_2$ with bpy-PMO should give the *N,N*-chelated complex, via coordination of both bipyridine rings.

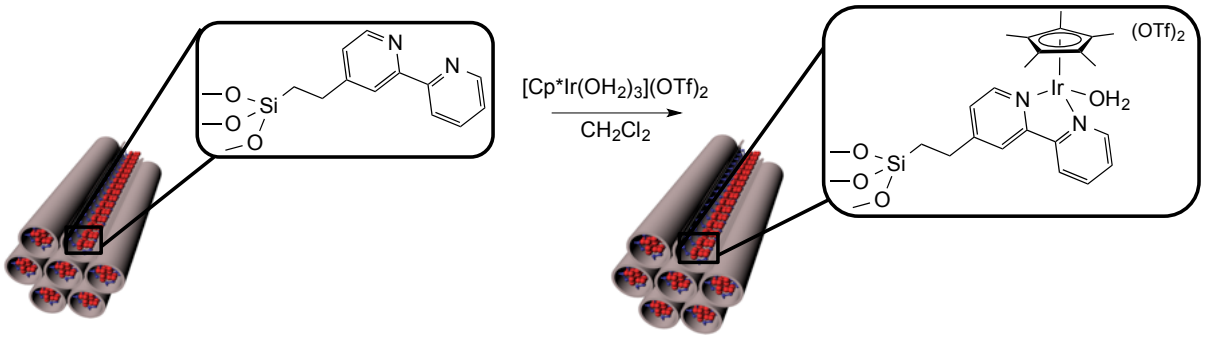

Scheme 5.5. Expected metalation of bpy-PMO with $[Cp^*Ir(OH_2)_3(OTf)_2]$ to give silica-supported Cp*Ir-bpy-PMO.

The ^{13}C CP/MAS NMR signals of Cp*Ir-bpy-PMO remain largely unchanged relative to bpy-PMO, however, an new peak 89 ppm for the Cp* ligand appears in the spectrum. A second peak for the methyl groups on the ring should appear at 9 ppm, although it is not clearly visible due to the intense broad ethylene signal (Fig. 5.9). Unlike for the ppy-PMO, no diagnostic ^{13}C signal appears upon coordination of Ir, however, the material undergoes an obvious color change from beige to yellow. The Ir content is 1.5 wt %, compared to the expected value of 2.6 wt%. A 2:1 ratio of bpy:Ir was used in the synthesis, however elemental analysis of the material reveals that the actual value is closer to 8:1.

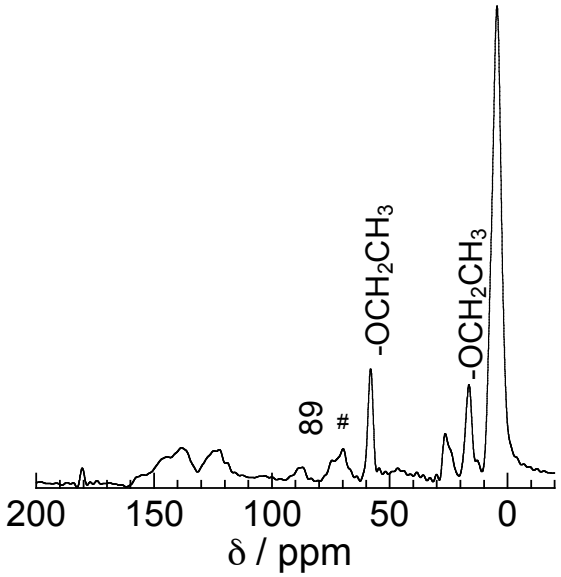

Figure 5.9. ^{13}C CP/MAS NMR spectrum of Cp*Ir-bpy-PMO (# indicates residual surfactant).

Both bpy-PMO and Cp*Ir-bpy-PMO materials exhibit type IV isotherms in nitrogen adsorption–desorption, with H1-type hysteresis loops at high relative pressures (Fig. 5.10). Consequently, these materials can be described as having pores of uniform size and shape. Cp*Ir bpy-PMO has considerably lower surface area, pore volume, and pore diameter, relative to the non-metalated material. The B.E.T. surface area declined from 611 m^2/g for bpy-PMO to 340 m^2/g for Cp*Ir bpy-PMO, while the corresponding B.J.H. pore volume decreased from 0.75 to 0.48 cm^3/g, due to possible blockage of the pores.

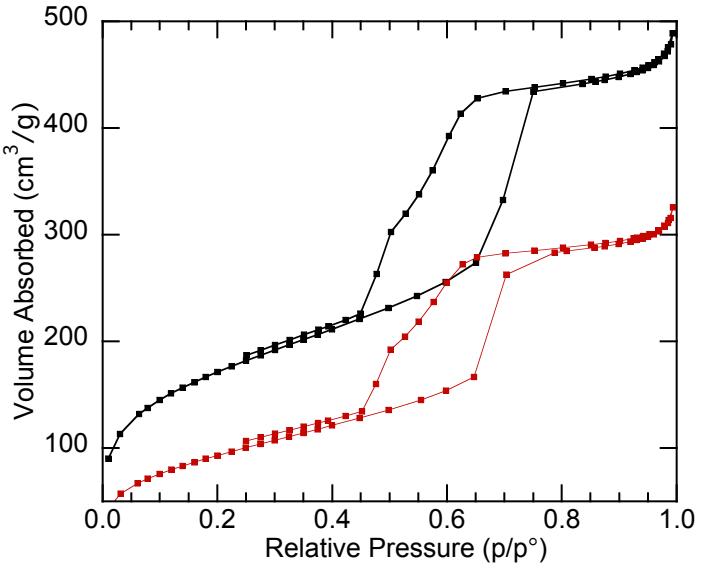

Figure 5.10. N_2 adsorption/desorption isotherms for bpy-PMO (black) and Cp*Ir-bpy-PMO (red).

The TEM images verify that hexagonally-ordered pores and linear channels are maintained upon metalation with iridium (Fig. 5.11). To our surprise, in some images small metal nanoparticles were also visible, and were identified as Ag by EDX (see Appendix II). In the synthesis of $[Cp^*Ir(OH_2)_3(OTf)_2]$, excess AgOTf was added to scavenge chloride ions from $[Cp^*IrCl_2]_2$, and removal of the Ag^+ was apparently incomplete. Fortunately, control reactions in a prior homogeneous study[6] involving performing the AWS reaction in the presence of AgOTf (the original silver source) and Ag_2O (the decomposition product of any excess AgOTf present during the synthesis, which is light-driven) had no effect on the TON

a

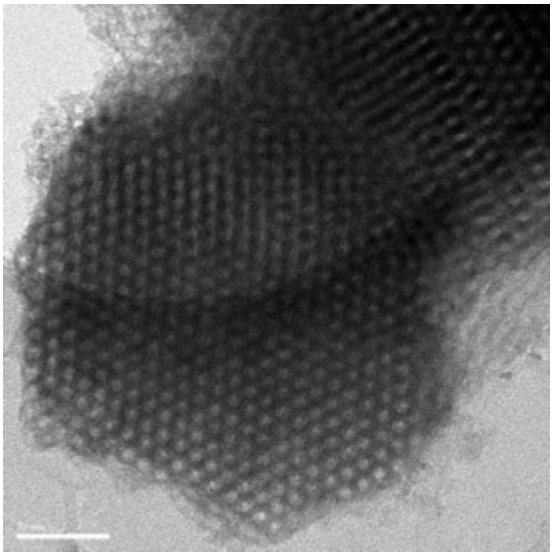

b

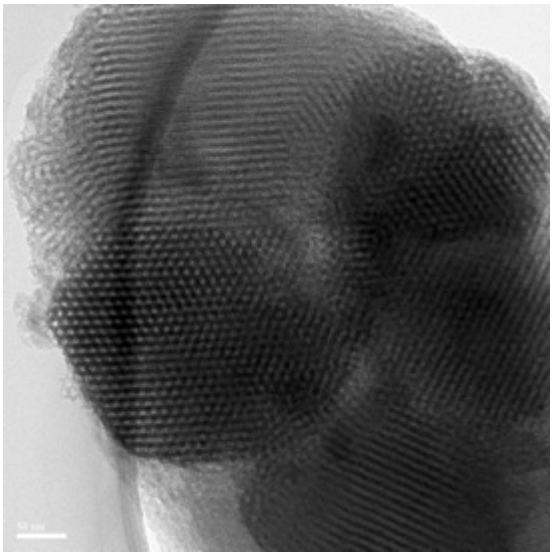

Figure 5.11. TEM images of Cp*Ir-bpy-PMO imaged at two different perspectives: (a) top view of hexagonally-ordered pores, and (b) side-view of regularly-ordered porous channels.

Fig. 5.12 displays DRIFT spectra of the bpy-PMO material before and after reaction with $Cp^*Ir(OH_2)_3(OTf)_2$. Much like the ppy-PMO, the spectrum of bpy-PMO contains several bands between 3100 and 2800 cm^{-1} corresponding to the C-H stretching modes of the propyl chain of the bpy-silane and some contribution from the alkyl chain of the surfactant. In addition, bands assignable to C=C and C=N aromatic ring modes of the bpy group and CH_2 bends of the propyl chain are present between 1350–1650 cm^{-1}.

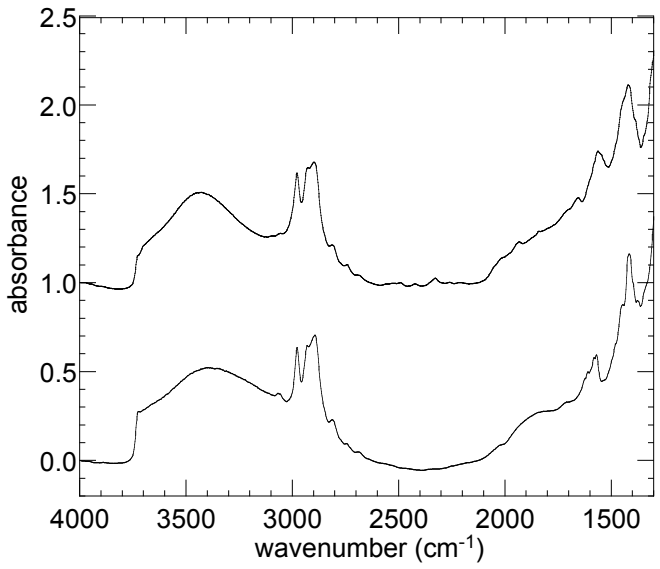

Figure 5.12. DRIFT spectra of bpy-PMO (bottom), and Cp*Ir-bpy-PMO (top).

Characterization of the metalated ppy-PMO and bpy-PMO materials (largely through NMR spectroscopy) is in good agreement with the properties of the molecular analogs. Thus the immobilized ppy and bpy ligands appear to preserve their coordination ability to form the metal complexes, although there is much unmetalated ligand. The general synthetic strategy appears successful and produces well-defined materials suitable for comparison of homogeneous and heterogeneous AWS catalysts.

5.3.5 Catalytic activity in AWS

The reactivity of Cp*Ir-ppy-PMO in propionaldehyde oxidation by water was explored under conditions similar to those used for the homogeneous reaction (using substrate to catalyst ratios of 125:1 and 68:1, for the homogeneous and heterogeneous systems, respectively). After 18 h at 105 °C (0.474 mM catalyst, 32.5 mM aldehyde, 10 mL

H_2O), we observed both propionic acid and *n*-propanol in a 3:1 ratio by solution-state ^1H NMR, in addition to unreacted starting material. Small amounts of *n*-propanol presumably forms by propionaldehyde disproportionation. Aldehyde conversion was low (*ca*. 3%), consistent with results for the analogous homogeneous catalyst. Although disproportionation is likely, the ratio between propionic acid and n-propanol is not 1:1 but rather 3:1. This implies that AWS catalysis is favored over disproportionation, as for the molecular catalyst.

The reactivity of Cp*Ir-bpy-PMO was also explored under conditions similar to those used for the homogeneous reaction (using substrate to catalyst ratios of 250:1 and 220:1, for the homogeneous and heterogeneous systems, respectively). In contrast to the analogous homogeneous catalyst, aldehyde conversion was low (*ca*. 30% compared to 99 % for the homogeneous). Disproportionation also seemed to be the major pathway, the ratio between propionic acid and n-propanol was nearly 1:1, indicating no AWS was occurring. This observation is also consistent with the homogeneous catalyst.

5.3.6 Catalytic activity for hydrogenation of levulinic acid (LA)

Although half-sandwich Cp*Ir complexes possess low activity for AWS (oxidation), these catalysts show excellent performance in the catalytic hydrogenation of ketones, acids and esters.[6, 34, 35] Plant biomass contains a high amount of oxygen-containing functional groups. Pretreatment of biomass through pyrolysis or biochemical transformations breaks down the recalcitrant material into organic alcohols, phenolics, acids, ketones, and esters, among other derivatives. Catalytic transformation of these building blocks could provide more sustainable feedstocks for the chemical industry. In particular, the conversion of levulinic acid (LA) into γ−valerolactone (GVL) has been extensively studied with both

homogeneous[34, 36-38] and heterogeneous[39-45] catalysts. Fu et al. reported that half-sandwich iridium complexes could be used to convert LA into GVL in excellent yields at mild temperatures and pressures (10 bar H_2, 120 °C).[34] Despite their high activity, homogeneous catalysts are often difficult to separate from the reaction mixture. Inspired by previous literature, we tested our silica-supported metal catalysts for an alternative transformation. Cp*Ir-ppy-PMO gave 100 % conversion of LA to GVL under 50 bar H_2, 120 °C in THF after 40 h.

5.4 Conclusion

In summary, we successfully prepared novel periodic mesoporous organosilicas with phenylpyridyl and bipyridyl groups covalently anchored in the silica framework. Co-condensation of the bulky organosilanes had no effect on the porous nature of the material. Characterization showed that the ppy and bpy ligands anchored to the framework preserve their coordination abilities. Reaction with Cp*M complexes resulted in robust tethering to give Cp*Ir-ppy and Cp*Ir-bpy-PMO materials. After confirming their identity through spectroscopy, these catalysts were tested for their activity in AWS under conditions similar to those used for their homogeneous analogs. Cp*Ir-ppy-PMO shows modest activity for AWS of propionaldehyde yet with low conversion (*ca.* 3 %), much like the homogeneous catalyst. However, when tested for a different catalytic transformation, hydrogenation of LA to GVL, we found 100% conversion after 40 h. These results demonstrate the potential of Cp*Ir-ppy-PMO as a catalyst for molecular-based heterogeneous catalytic reactions.

5.5 References

1. Smith, M. B., *March's Advanced Organic Chemistry: Reactions, Mechanisms, and Structure*. John Wiley and Sons, Inc.: Hoboken, NJ, 2007.

2. Stanley, G. G.; Aubry, D. A.; Bridges, N.; Barker, B.; Courtney, B., *Prepr. Pap. - Am. Chem. Soc., Div. Fuel Chem.* **2004,** *49*, 712-713.

3. Murahashi, S.-I.; Naota, T.; Ito, K.; Maeda, Y.; Taki, H., *J. Org. Chem.* **1987,** *52*, 4319-4327.

4. Zweifel, T.; Naubron, J.-V.; Grützmacher, H., *Angew. Chem. Int. Ed.* **2009,** *48*, 559-563.

5. Balaraman, E.; Khaskin, E.; Leitus, G.; Milstein, D., *Nat. Chem.* **2013,** *5*, 122-125.

6. Brewster, T. P.; Ou, W. C.; Tran, J. C.; Goldberg, K. I.; Hanson, S. K.; Cundari, T. R.; Heinekey, D. M., *ACS Catal.* **2014,** *4*, 3034-3038.

7. Harriman, A.; Pickering, I. J.; Thomas, J. M.; Christensen, P. A., *J. Chem. Soc., Faraday Trans.* **1988,** *84*, 2795.

8. Hintermair, U.; Hashmi, S. M.; Elimelech, M.; Crabtree, R. H., *J. Am. Chem. Soc.* **2012,** *134*, 9785-9795.

9. Mills, A.; Russell, T., *J. Chem. Soc., Faraday Trans.* **1991,** *87*, 1245.

10. Trasatti, S., *J. Electroanal. Chem. Interfacial Electrochem.* **1980,** *111*, 125.

11. Burleigh, M. C.; Markowitz, M. A.; Jayasundera, S.; Spector, M. S.; Thomas, C. W.; Gaber, B. P., *J. Phys. Chem. B* **2003,** *107*, 12628-12634.

12. Guo, W.; Li, X.; Zhao, X. S., *Microporous Mesoporous Mater.* **2006,** *93*.

13. Shylesh, S.; Jha, R. K.; Singh, A. P., *Microporous Mesoporous Mater.* **2006,** *94*.

14. Eisen, M. S.; Haskel, A.; Chen, H.; Olmstead, M. M.; Smith, D. P.; Maestre, M. F.; Fish, R. H., *Organometallics* **1995,** *14*, 2806-2812.

15. Liu, J.; Yang, Q.; Kapoor, M. P.; Setoyama, N.; Inagaki, S.; Yang, J.; Zhang, L., *J. Phys. Chem. B* **2005,** *109*, 12250.

16. Li, L.; Brennessel, W. W.; Jones, W. D., *Organometallics* **2009,** *28*, 3492.

17. Ogo, S.; Makihara, N.; Kaneko, Y.; Watanabe, Y., *Organometallics* **2001,** *20*, 4903-4910.

18. Wu, F.; Feng, Y.; Jones, C. W., *ACS Catal.* **2014,** *4*, 1365-1375.

19. Nguyen, J. V.; Jones, C. W., *Macromolecules* **2004,** *37*, 1190-1203.

20. Nunes, C. D.; Valente, A. A.; Pillinger, M.; Fernandes, A. C.; Romao, C. C.; Rocha, J.; Goncalves, I. S., *J. Mater. Chem.* **2002,** *12*, 1735-1742.

21. Nunes, C. D.; Pillinger, M.; Valente, A. A.; Goncalves, I. S.; Rocha, J.; Ferreira, P.; Kuhn, F. E., *Eur. J. Inorg. Chem.* **2002**, 1100-1107.

22. Maillet, C.; Janvier, P.; Pipelier, M.; Bertrand, M. J.; Praveen, T.; Bujoli, B., *Eur. J. Org. Chem.* **2002**, 1685-1689.

23. Mongey, K. F.; Vos, J. G.; MacCraith, B. D.; McDonagh, C. M.; Coates, C.; McGarvey, J. J., *J. Mater. Chem.* **1997,** (7), 1473-1479.

24. Ogawa, M.; Nakamura, T.; Mori, J. I.; Kuroda, K., *Microporous Mesoporous Mater.* **2000,** *48*, 159-164.

25. Collinson, M. M.; Novak, B.; Skylar, M.; Taussig, J. S., *Anal. Chem.* **2000,** *72*, 2914-2918.

26. Li, H. R.; Lin, J.; Zhang, H. J.; Li, H. C.; Fu, L. S.; Meng, Q. G., *Chem. Commun.* **2001**, 1212-1213.

27. Sato, Y.; Kagotani, M.; Souma, Y., *J. Mol. Catal. A: Chem.* **2000,** *151*, 79-85.

28. Odobel, F.; Bujoli, B.; Massiot, D., *Chem. Mater.* **2001,** *13*, 163-173.

29. Odobel, F.; Massiot, D.; Harrison, B. S.; Schanze, K. S., *Langmuir* **2003,** *19*, 30-39.

30. Gosh, P. K.; Spiro, T. G., *J. Am. Chem. Soc.* **1980,** *102*, 5543-5549.

31. Waki, M.; Mizoshita, N.; Tani, T.; Inagaki, S., *Angew. Chem. Int. Ed.* **2011,** *50*, 11667-11671.

32. Waki, M.; Maegawa, Y.; Hara, K.; Goto, Y.; Shirai, S.; Yamada, Y.; Mizoshita, N.; Tani, T.; Chun, W.-J.; Muratsugu, S.; Tada, M.; Fukuoka, A.; Inagaki, S., *Angew. Chem. Int. Ed.* **2014,** *136*, 4003-4011.

33. Gregg, S. J.; Sing, K. S. W., *Adsorption, Surface Area and Porosity* Academic Press: London, 1982; Vol. 2nd ed.

34. Deng, J.; Wang, Y.; Pan, T. X., Q.; Guo, Q.-X.; Fu, Y., *ChemSusChem* **2013,** (6), 1163-1167.

35. Liu, Z.; Deeth, R. J.; Butler, J. S.; Habtemariam, A.; Newton, M. E.; Sadler, P. J., *Angew. Chem. Int. Ed.* **2013,** *52*, 4194-4197.

36. Chalid, M.; Broekhius, A. A.; Heeres, H. J., *J. Mol. Catal. A: Chem.* **2011,** *241*, 14.

37. Geilen, F. M. A.; Engendahl, B.; Harwardt, A.; Marquardt, W.; J., K.; Leitner, W., *Angew. Chem. Int. Ed.* **2010,** *49*, 5510.

38. Li, W.; Xie, J. H.; Lin, H.; Zhou, Q. L., *Green Chem.* **2012,** *14*, 2388.

39. Al-Shaal, M. G.; Wright, W. R. H.; Palkovits, R., *Green Chem.* **2012,** *14*, 1260.

40. Delhomme, C.; Schaper, L. A.; Zhang-Preße, M.; Raudaschl-Sieber, G.; Weuster-Botz, D.; Kühn, F. E., *J. Organomet. Chem.* **2013,** *724*, 297.

41. Raspolli Galletti, A. M.; Antonetti, C.; Ribechini, E.; Colombini, M. P.; Nassi o Di Nasso, N.; Bonari, E., *Appl. Energy* **2013,** *102*, 157.

42. Wright, W. R. H.; Palkovits, R., *ChemSusChem* **2012,** *5*, 1657.

43. Yan, K.; Lafleur, T.; Wu, G.; Liao, J.; Ceng, C.; Xie, X., *Appl. Catal. A* **2013,** *468*, 52.

44. Schutte, H. A.; Thomas, R. W., *J. Am. Chem. Soc.* **1930,** *52*, 3010-3012.

45. Christian, R. V., Jr.; Brown, H. D.; Hixon, R. M., *J. Am. Chem. Soc.* **1947,** *69*, 1961-1963.

Appendix II

A2.1 Synthesis of 2-[2-[2-(trimethoxysilyl)ethyl]phenyl]pyridine (ppy-silane).

In a JY-NMR tube (^{iPr}NCOP^{tBu})Ir(H)Cl (0.040 g, 0.069 mmol), 2-phenylpyridne (0.015 mL, 0.104 mmol) and Sodium tert-butoxide (0.020 g) were left to react at room temperature in 0.5 mL of toluene-d_8 until total conversion to *trans*-(^{iPr}NCOP^{tBu})Ir(H)(2-phpy) is observed in ^{1}H NMR. The solution is transferred to a 20 mL vial with the aid of n-pentane (2 mL) and pumped dry. The residue was dispersed in n-pentane (10 mL) and the solution decanted to another vial and pumped dry. This residue was transferred to a JY NMR tube with the aid of 2-phenylpyridine (0.247 mL, 1.71 mmol) first and then with trimethoxyvinylsilane (0.661 mL). The reaction mixture was heated at 120 ºC in an oil bath. Total conversion is observed within 6 hours. It is filtered through a short plug of Celite at room temperature. The filtrate is pumped dry to yield a bright red colored oil. Yield: 0.17 g (32 %). ^{1}H NMR (C_6D_6, 25 ºC): d 8.55 to 8.53 (m, 1H), 7.33 (dd, J = 7.5 Hz, J^2 = 1.5 Hz, 1H), 7.25 to 7.22 (m, 1H), 7.18 (dd, J = 7.5 Hz, J^2 = 1.5 Hz, 1H), 7.12 to 7.07 (m, 3H), 6.69 to 6.65 (m, 1H), 3.37 (s, 9H, CH_3O), 3.13 to 3.09 (m, 2H, CCH_2), 1.12 to 1.08 (m, 2H, CH_2Si). ^{13}C NMR (C_6D_6,25 ºC): d 161.3, 149.6, 143.9, 140.9, 136.3, 130.7, 130.2, 129.1, 126.4, 124.4, 121.8, 50.6, 27.3, 12.8.

A2.2 Synthesis of 2-(2-pyridyl)-(3-[2-(trimethoxysilyl)ethyl]pyridine (bpy-silane).

Prepared following the same procedure. Yield: 0.13 g (25 %) ^{1}H NMR (C_6D_6,25 ºC): d 8.74 (m, 1H), 8.53 (m, 1H), 8.40 (m, 1H), 7.24 to 7.19 (m, 2H), 6.75 to 6.67 (m, 2H), 3.36

(s, 9H, CH_3O), 2.87 to 2.83 (m, 2H, CCH_2), 1.09 to 1.06 (m, 2H, CH_2Si). ^{13}C NMR (C_6D_6,25 ^oC): d 158.4, 157.1, 149.7, 146.8, 137.2, 137.0, 124.0, 123.2, 121.5, 50.6, 26.4, 11.8.

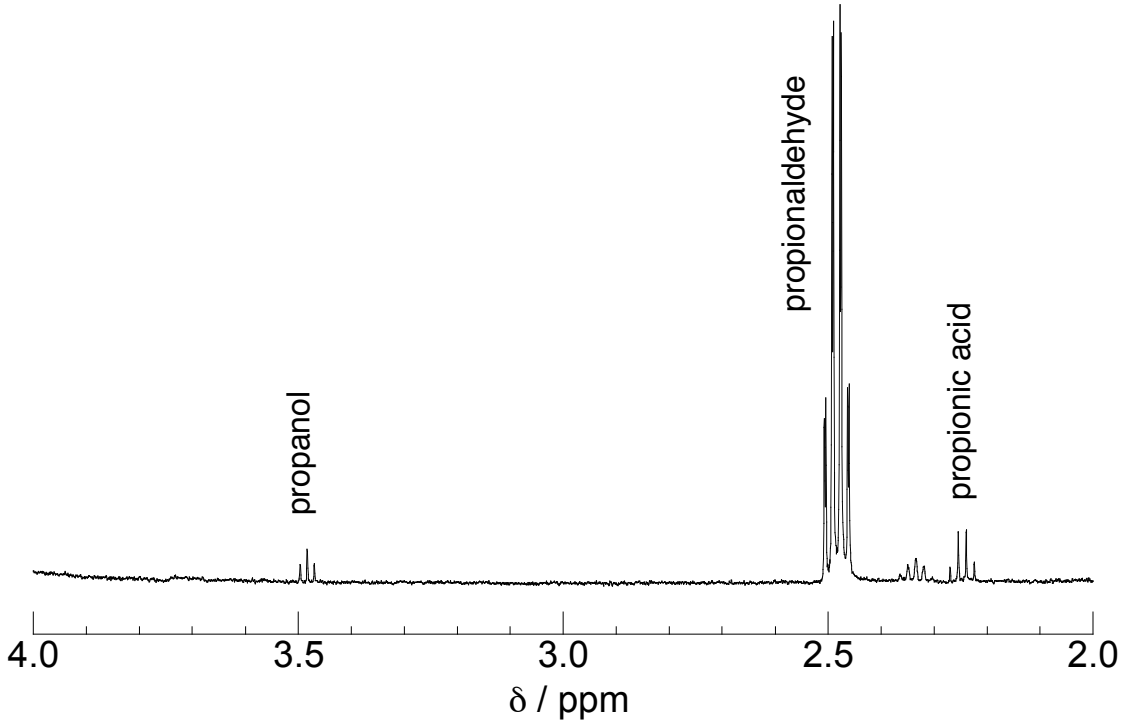

Figure A2.1. Representative ^1H spectrum in D_2O from aldehyde-water shift reaction of propionaldehyde and Cp*Ir-ppy-PMO.

a

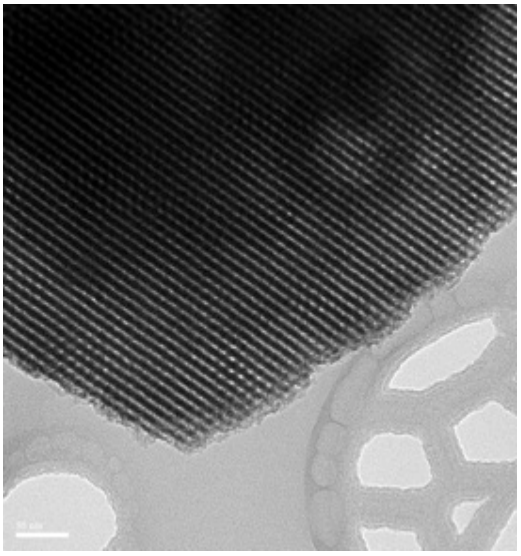

b

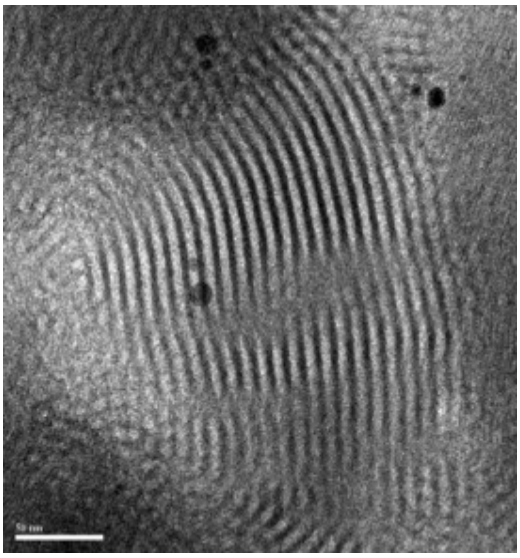

Figure A2.2. TEM images of Cp*Ir-bpy-PMO imaged at two different perspectives: (a) top view of pore channels, and (b) side-view of regularly-ordered porous channels (black dots are Ag nanoparticles from $Cp^*Ir(OH_2)_3(OTf)_2$ synthesis).

Chapter 7: Conclusions

We demonstrated that it is possible to tailor and isolate well-defined surface species using a molecular approach. Two different methodologies were used to synthesize immobilized catalysts: ligand grafting followed by metal tethering on a silica support and co-condensation. Intrinsic features of the supported complexes were characterized, and comparisons were made to the corresponding molecular catalysts.

Typically, multi-step reactions are used to immobilize metal complexes on a support, but only the final material is characterized to a modest extent. During our ligand grafting reactions, we confirmed the importance in characterizing the material at each step of the reaction. In synthesizing a silica-supported vanadium catalyst, we discovered unexpected reactivity of the ligand tether, through solid-solid NMR and EPR, upon introduction of the metal precursor leading to a mixture of vanadium species, which turned out to be less active than the homogeneous system. Such side reactions can be easily overlooked or entirely missed if appropriate analysis of the material is not performed.

Simplified models of silica supports tend to describe surface silanols as uniformly spatially distributed on the silica surface. In many cases, ligands tethers are alkyl chains that give the supported catalyst some mobility/flexibility similar to that exhibited in solution. In the preparation of the vanadium catalyst, elemental analysis showed that two grafted ligands were close enough in spatial proximity to coordinate to a single metal center. This highlights the need to use a variety of complementary techniques to accurately assign the structure of immobilized catalysts.

In grafting propyl bis(pentafluorophenyl)boranes on silica, we learned that preserving

the structure of the catalyst is not only difficult during synthesis but also in prolonged storage of the material. In these lengthy syntheses, it is not often practical to make new material every time a reaction is tested. Proper storage of these sensitive materials in sealed ampules or at low temperature can prevent changes, likely due to adventitious water.

Catalysts with higher hydrothermal stability than grafted/tethered complexes can be prepared by co-condensing organosilanes in the silica framework of periodic mesoporous organosilicas. The hydrophobic nature of these materials can create microenvironments within the pores that could preserve the catalyst and prevent leaching by ligand detachment in aqueous conditions. Additionally, having more phenylpyridyl or bipyridyl groups than the metal could capture any released metal fragments.

Expanding capabilities to design 'nanoarchitectures' at the molecular level will enable chemists to build ideal catalysts for sustainable transformations of high added-value molecules. We expect advances in catalyst design, synthesis, and characterization will lead to a better understanding of catalyst structure and function and, thus, to advances in existing catalytic processes and the development of new technologies.